

Charge Carrier Dynamics in Organo Lead Halide Perovskites

THÈSE N° 7702 (2017)

PRÉSENTÉE LE 5 MAI 2017

À LA FACULTÉ DES SCIENCES DE BASE
LABORATOIRE D'OPTOÉLECTRONIQUE QUANTIQUE
PROGRAMME DOCTORAL EN PHYSIQUE

ÉCOLE POLYTECHNIQUE FÉDÉRALE DE LAUSANNE

POUR L'OBTENTION DU GRADE DE DOCTEUR ÈS SCIENCES

PAR

Mahmoud Saeed Qaid Mohammad HEZAM

acceptée sur proposition du jury:

Prof. N. Grandjean, président du jury
Prof. B. M. J. Deveaud, directeur de thèse
Prof. M. Saba, rapporteur
Prof. O. Bakr, rapporteur
Prof. A. Hagfeldt, rapporteur



ÉCOLE POLYTECHNIQUE
FÉDÉRALE DE LAUSANNE

Suisse
2017

إلى أمي ..

إلى أبي ..

إلى زوجتي ..

إلى (عمرو) و (محمد) ..

Acknowledgements

Many people were key and important for this thesis to be realized, to whom I express my highest gratefulness and gratitude.

I start with thanking my advisor and my marvelous teacher, Prof. Benoit Deveaud. It has been a life pride for me to work under the supervision of Prof. Benoit. The freedom he offered to choose the research topics, the paramount scientific guidance every time we meet, and the friendly humble character in all the time, will keep a great source of inspiration for me. I can't also forget his help in resolving, in the most elegant way I could imagine, different administrative issues at the EPFL and at the side of King Saud University (KSU) as well. Thanks, Benoit, for everything.

Second, I want to thank Prof. Abdullah Aldwayyan, KSU for his continuous support during the whole period of this thesis. Under his management, I really enjoyed working with an active group in Riyadh with anti-frustrated visions and countless research ideas.

I want also to thank Prof. Nazeeruddin, EPFL, who kept providing state-of-the-art perovskite samples, since the early days of perovskite revolution. All samples and solar cell devices presented in this thesis have been fabricated by the group of Prof. Nazeeruddin, which has been an essential success parameter, considering the large instability issues of perovskites in all research topics discussed in this thesis. The personal support and steering advices from Prof. Nazeeruddin are also unforgettable.

Next, I want to make a very specialized thanks to Dr. Gwenole Jacopin, the post-doctoral fellow in the LOEQ group. He has been bright and determined in all the moments, with an immediate and highly responsive character. I thank him for all the scientific discussions we have had and for his experimental help during my thesis work as well. I have to mention here that some experimental results presented in this thesis were purely carried out by him (namely, data of Figure 3.10, Figure 3.11, Figure 3.19, Figure 3.20, data of Figure 4.7, Figure 5.3, and Figure 5.7). I wish Dr. Gwenole all the best in his scientific future.

I want to thank many other people whom I encountered during my thesis. I thank Dr. Jean-Daniel Ganiere, formerly Research Associate in the LOEQ group, for his experimental support especially at the beginning of this thesis. I thank Mehran Shahmohammadi, former PhD student in LOEQ, for his experimental help especially during the first two years of my thesis. I also thank Wei Liu, current PhD student in LOEQ, for the fruitful discussions and for the enjoyable walkings in the city. I also thank all the people who are/have been working in the group of Prof. Nazeeruddin, namely Dr. Peng Qin, who supplied us with "an infinite number

of samples”, Dr. Ibrahim Dar, who showed readiness to fabricate samples even at mid-night, Dr. Neha Arora, who has been special in making outstanding FAPbBr₃ films and devices, Dr. Giulia Grancini, for the fruitful scientific discussions. I also thank my friends in Riyadh, Saif Qaid, Hamid Ghaithan, Abdulaziz Alqasem, Dr. Naziruddin Khan who created an immensely active research environment. Here, I go back in order, and I thank Dr. Mohammad Alduraibi, for all the supportive efforts and time especially in the research work on ZnO nanowires.

I want to declare special thanks for the secretary of the LOEQ group, Claire-Lyse Rouiller, for the superior administrative support. I also thank Anh Eymann, secretary of the Physics PhD program, for her continuous help and guidance.

I here make the important stop to thank my family for their support during my thesis. I start with my mother, who kept doing special prayers and good deeds every time I travel. Her emotions have been more efficient in guiding my life than anything else. I thank my father for everything he made for me, and for his continuous encouragement. I thank all my sisters and brothers, who supported me a lot. At the end, I thank my little family, my wife and my two kids Amr and Mohammad. I highly appreciate the extraordinary support I received from my wife, for whom I owe a lot. I also appreciate the patience and help I received from my kids. I have to admit that they, both, helped me in choosing the colorings of some figures.

Mahmoud Hezam

Abstract

In the last five years, organo lead halide perovskites have emerged as a new and efficient player in the field of photovoltaics, jumping in a short time to an advanced front position. This class of materials has also shown proficient light emission capabilities, and perovskite-based light emission devices have been demonstrated as well. Therefore, the optical characterization of these materials has been widely used to explain and evaluate their light absorption/emission characteristics. Despite their remarkable success, they also have shown severe intrinsic sensitivity to their surrounding conditions, e.g. UV light, oxygen, and moisture.

This thesis is composed of three studies on the optical characterization of perovskites. The thesis starts with an introductory chapter on organo lead halide perovskites, which includes a literature review on the possible origins of perovskite phase instability. Next, the first study of this work presents a detailed investigation on the photovoltaic and spontaneous emission properties of FAPbBr₃ perovskite films (FA = Formamidinium). The study first introduces the absorption/emission detailed balance equilibrium in a working perovskite solar cell, based on which the device characteristics are calculated under different ideal/non-ideal conditions. Time-resolved photoluminescence (TRPL) is shown to be a good measure for evaluating the maximum possible open-circuit voltage (V_{oc}) of the device. Perovskite solar cells were fabricated, using two differently prepared FAPbBr₃ perovskite films, and the results were correlated with TRPL measurements. A record V_{oc} of 1.42 V that is higher than the value of the built-in potential (as reported in the literature) developed by the device contacts was achieved, and consequential insights about charge separation dynamics are discussed. Amplified spontaneous emission (ASE) was successfully demonstrated for the same perovskite films. Bandgap renormalization (BGR) was observed as a red-shift in the ASE peak, and the gain behavior is shown to allow the estimation of BGR values directly from the ASE peak position. A value of $5-7 \times 10^{-9}$ eV.cm was obtained for the BGR constant.

The second study in this work addresses the UV-induced damage on MAPbI₃ perovskite (MA = Methylammonium). The study reports that UV degradation can occur in the perovskite bulk, and is not only associated with the presence of oxygen or TiO₂ surface, as reported by some recently published works. UV degradation is found to switch off when the sample is cooled below 200 K, which indicates the presence of a thermally activated process. Based on that, the direct bond dissociation in the thermally liberated MA cations is proposed to be a first UV-induced degradation step, which can be accompanied/followed by other degradation processes.

The third study demonstrates cathodoluminescence (CL) mapping of $\text{MAPbI}_{3-x}\text{Br}_x$ microcubes. An abnormal CL intensity contrast between the center and edge of single microcubes is observed, where the CL emission is highly reduced in the centers at room temperature, and almost vanishes at 4 K, while the edges have prominent CL emission. The observed behavior is correlated, with the help of STEM-EDX maps, with a noticeable deficiency of MA ions in the centers. The CL maps are also correlated with Monte Carlo simulations under different e-beam acceleration voltages, and the enhanced edge CL emission is explained as a result of diffusion assisted carrier recombination.

Keywords: organo lead halide perovskite, perovskite solar cells, photoluminescence, time-resolved photoluminescence, cathodoluminescence, UV-induced damage, amplified spontaneous emission

Résumé

Au cours des cinq dernières années, les pérovskites à base d'halogénure de plomb sont apparus comme un nouvel acteur extrêmement prometteur dans le domaine des dispositifs photovoltaïques. Ces pérovskites ont occupé, en un minimum de temps, une position très avantageuse. Cette classe de matériaux s'est également montrée fort efficace dans l'émission de lumière, puisque des émetteurs de lumières à base de pérovskites ont été démontrés. En conséquence, la caractérisation optique de ces matériaux a été une démarche quasiment universelle pour expliquer et évaluer leurs caractéristiques d'absorption/émission de lumière. Malgré leurs succès remarquables, les pérovskites se sont montrés extrêmement sensibles aux conditions environnantes, comme par exemple, la lumière UV, la présence d'oxygène ou l'humidité.

Cette thèse est composée sur la base de trois études de caractérisation optique des pérovskites. Au départ, la thèse commence par un chapitre introductif sur les pérovskites à base d'halogénure de plomb, comprenant une revue de la littérature quant aux origines possibles de l'instabilité des pérovskites vis-à-vis les conditions environnantes.

La première partie de ce travail présente une étude détaillée des propriétés photovoltaïques et d'émission spontanée des couches de pérovskites FAPbBr₃ (FA = Formamidinium). L'étude présente d'abord un bilan détaillé à l'équilibre de l'absorption/émission dans une cellule solaire à base de pérovskites en fonctionnement. Les calculs sont basés sur les caractéristiques du dispositif dans des conditions idéales et non-idéales. Nous montrons ensuite que la photoluminescence résolue dans le temps (TRPL) est une technique parfaitement adaptée pour évaluer le maximum prévisible de la tension en circuit-ouvert (V_{OC}) du dispositif. Des cellules solaires à base de pérovskite ont été fabriqués, deux modes de préparation différents pour la couche de pérovskite FAPbBr₃ et les caractéristiques des cellules ont été corrélées avec les mesures de TRPL. Une valeur record de V_{OC} de 1.42 V, plus élevée en fait que la valeur du potentiel interne (constatée dans la littérature) généré par le dispositif a été obtenue, et de nouvelles idées sur la dynamique de la séparation des charges sont discutées. L'observation de l'émission spontanée amplifiée (ASE) a été obtenue avec succès pour les mêmes couches de pérovskite. La renormalisation du gap (BGR) a été déduite du déplacement vers le rouge du pic de l'ASE, et le comportement de gain est une solution simple qui permet l'estimation des valeurs de la BGR directement à partir de la position du pic de l'ASE. Une valeur de $5 \text{ à } 7 \times 10^{-9} \text{ eV.cm}$ a été obtenue pour la constante de BGR.

La deuxième étude menée au cours de ce travail porte sur les dégradations des pérovskites MAPbI₃ (MA = méthylammonium) provoquées par la lumière UV. L'étude montre que la dégradation UV peut se produire

dans le pérovskite massif et n'est pas seulement associée à la présence d'oxygène ou de TiO_2 en surface, comme rapporté par certains travaux publiés récemment. En effet, la dégradation UV est bloquée lorsque l'échantillon est refroidi en dessous de 200 K, ce qui indique la présence d'un processus activé thermiquement. Sur cette base, la dissociation de la liaison directe des cations MA est proposée comme une première étape de la dégradation induite par la lumière UV. Celle-ci peut être accompagnée ou suivie par d'autres processus de dégradation.

La troisième étude décrit les résultats de la cartographie de cathodoluminescence (CL) des microcubes de $\text{MAPbI}_{3-x}\text{Br}_x$. Un contraste anormal de l'intensité de CL entre le centre et le bord d'un microcube unique a été observée, où l'émission CL est fortement réduite au centre du cube à température ambiante, et presque nulle à 4 K, tandis que les bords présentent des émissions importantes de CL. Le comportement observé pourrait être corrélé, avec un déficit d'ions MA dans les centres mesuré par STEM-EDX. Les images de CL sont également en corrélées avec les résultats de simulations Monte Carlo sous différentes tensions d'accélération du faisceau d'électrons. Au final, l'augmentation relative de l'émission de CL du bord s'explique par la recombinaison des porteurs assistée par diffusion.

Mots-clés: pérovskites à base d'halogénure de plomb, cellules solaires à base de pérovskites, photoluminescence, photoluminescence résolue en temps, cathodoluminescence, dégradation induite par UV, émission spontanée amplifiée

Table of Contents

Acknowledgements	iii
Abstract (English)	v
Résumé (Français)	vii
Chapter 1: Organo Lead Halide Perovskites	1
1.1 A Glance of History	1
1.2 The Perovskite Structure	2
1.3 Organo Metal Halide Perovskites	4
1.4 Potential of Perovskites in Photovoltaic Applications	5
1.5 Methylammonium Lead Halide Perovskite (MAPbI ₃)	7
1.6 Mixed Halide MAPbI _{3-x} Br _x Perovskite	13
1.7 Effects of Organic Cation Replacements: Formamidinium vs. Methylammonium	15
1.8 Formamidinium Lead Bromide (FAPbBr ₃)	16
1.9 Potential of FAPbBr ₃ in Light Emission Applications	17
1.10 Description of Subsequent Chapters	18
References	20
Chapter 2: Experimental Setups	31
2.1 Picosecond Time-resolved Photoluminescence Setup	31
2.1.1 Excitation Line	31
2.1.2 Detection Line	34
2.1.3 Vacuum and Cooling Systems	36
2.2 High Power Picosecond Pulsed Time Integrated PL Setup	36
2.2.1 Excitation Line	36
2.2.2 Optical Path and PL Detection	38
2.3 Cathodoluminescence Setup	38
2.3.1 Interaction of Electron Beam with Matter	39
2.3.2 Description of the Cathodoluminescence setup	40
References	41

Chapter 3: Photovoltaic and Amplified Spontaneous Emission Studies on FAPbBr ₃	
Thin Films	43
3.1 Theoretical Background	44
3.1.1 Open-Circuit Measurements	46
Light Intensity-Dependent Open Circuit Voltage (V_{oc})	46
Time-resolved Photoluminescence	52
3.1.2 Short Circuit Measurements	53
J-V Measurements	53
IPCE and Electroluminescence Measurements	55
3.1.3 Beyond Illumination Level of Solar Radiation: Light Amplification	56
3.2 Description of Samples	59
3.3 Results and Discussion	59
3.3.1 Time-resolved PL and Photovoltaic Studies	59
3.3.2 Amplified Spontaneous Emission Studies	64
PL Quenching by Spiro-OMeTAD	67
Investigation of Threshold Carrier Densities under Different Excitation	
Wavelengths	68
References	74
Chapter 4: Time-resolved Photoluminescence Studies on MAPbI ₃ /Metal Oxide	
Interfaces	79
4.1 Introduction	80
4.2 Description of Samples	81
4.3 Studies on UV-induced damage at MAPbI ₃ /metal oxide interface	82
4.3.1 Room Temperature Measurements	82
UV Degradation at the TiO ₂ /MAPbI ₃ interface	85
UV Degradation at the Al ₂ O ₃ /MAPbI ₃ interface	87
UV Degradation in bulk MAPbI ₃	88
4.3.2 Low Temperature Measurements	90
4.3.3 Rationalizing the results	93
4.4 A Word about Electron Injection at the MAPbI ₃ /TiO ₂ interface	94
References	96
Chapter 5: Asymmetric Cathodoluminescence Emission in CH ₃ NH ₃ PbI _{3-x} Br _x	
Perovskite Single Crystals	101
5.1 Introduction	102
5.2 Description of Samples and Experimental Conditions	103
5.3 Results and Discussion	105
References	113

Chapter 6: Conclusions	117
6.1 Summary of Results	117
6.2 Future Perspectives	118
Curriculum Vita	121

...all perovskites (which have a habit of doing the unexpected)...

Mike Glazer, 1975 [5]

Chapter 1

Organo Lead Halide Perovskites

In this chapter, a short introductory account on organo lead halide perovskites is provided. The ideal perovskite crystalline structure is described, along with the different atomistic and structural factors that impact the perovskite phase stability and crystalline order. Taking $\text{CH}_3\text{NH}_3\text{PbI}_3$ as a model perovskite material, being the most successful and mostly explored organo lead halide perovskite photovoltaic material, a comprehensive literature review is provided, showing how the crystalline disorder is a major motive behind the superior light harvesting/charge extraction efficiencies and the remarkably poor device stability at the same time. This chapter also serves as an introduction to three organo lead halide materials that are studied in this manuscript, namely, $\text{CH}_3\text{NH}_3\text{PbI}_3$, $\text{CH}_3\text{NH}_3\text{Pb}_{3-x}\text{I}_x$ (with $x \sim 0$) and $\text{CH}(\text{NH}_2)_2\text{PbBr}_3$.

1.1 A Glance of History

The word “perovskite” was originally used to name the CaTiO_3 mineral, which was discovered by Gustave Rose in the Ural Mountains in 1839. Rose used the word “perovskite” to name the new mineral after the Russian mineralogist Lev Perovski (1792-1856) [1]. New minerals, having the same ABX_3 compound structure, have been discovered since then, and the word “perovskite structure” has been used to indicate such materials. It was only in 1926 that Victor Goldschmidt succeeded, based on basic crystal chemistry concepts and available data on physical properties (e.g. melting points, hardness...etc) of many ternary perovskite-like compounds, to describe the atomic chemical positioning of cations and anions in the perovskite structure [2]. The first XRD data was published for BaTiO_3 perovskite by Helen Megaw in 1945 [3]. In 1969-1976, Mike Glazer, who first worked as a post-doc in the group of Helen Megaw, discovered the 23 types of tilt in the octahedra of perovskites, and developed a simple and firm notation to describe them [4], [5], which has been widely adopted thereafter.

The perovskite structure can be visualized as composed of corner-sharing octahedra of BX_6 , where one A cation is placed in the cage formed by eight adjacent BX_6 octahedra. The A cation in the ABX_3 perovskite structure has shown important steric effects that have been responsible for the observation of many interesting physical properties of perovskite compounds in different applications over the last few

decades. Specifically, organic A cations of different molecular sizes and properties can be introduced in the perovskite lattice to produce layered perovskites. In layered perovskites, as will be discussed below in this chapter, the organic cation (A in the ABX_3 perovskite structure) is chosen with a large size such that it spatially separates adjacent BX_6 octahedra in one direction. This spatial separation along one crystalline axis results in a layered structure, where sheets of inorganic BX_6 octahedra are sandwiched between organic layers [6]–[9]. Layered perovskites were early discovered and investigated for different applications [10]–[18]. For example, a lot of research work in the 1960s-1970s was carried out to study the two-dimensional magnetic interactions between BX_6 layers, where B is a magnetic ion, e.g. Cu^{2+} , Mn^{2+} , Fe^{2+} ..etc [10]–[12]. In the 1990s, several organic-based layered perovskites were investigated for their electrical and optical properties[13], [15]–[18].

The distinctly successful story of perovskites in photovoltaics started first by the work of Tsutomu Miyasaka and his team early in 2006. Between 2006-2009, Miyasaka's group used quantum dots of organic-cation based perovskites to replace molecular dyes as light harvesting entities in dye-sensitized solar cells [19]–[23]. During this period, the rate of success was noticeably slow before a power conversion efficiency (PCE) of 6.5% was finally achieved in 2011 by Im et al [24]. In 2012, PCEs of ~ 9-11% were obtained by Miyasaka and other groups [25], [26] ushering in the birth of "*perovskite solar cells*". During the time of carrying out this thesis, thousands of patents and publications have appeared on perovskite solar cells.

1.2 The Perovskite Structure

The ideal perovskite structure has a cubic unit cell as shown in Figure 1.1. It has the general formula ABX_3 , where the A cation is placed at the body center ($\frac{1}{2}, \frac{1}{2}, \frac{1}{2}$), the B cation at the corners of the cube (0,0,0), and the X anion at the centers of cube edges ($\frac{1}{2}, 0, 0$), $(0, \frac{1}{2}, 0)$, $(0, 0, \frac{1}{2})$. This structure has O_h symmetry. Assuming a cubic unit cell cube with side a , the B-X bond length = $a/2$. The octahedral coordination of the B atom by six X atoms can also be seen in Figure 1.1.

It is also common, and very useful, to consider the perovskite structure as composed of corner sharing BX_6 octahedra, as mentioned above. Each X atom is then shared by two octahedra, and the corner sharing octahedra spatially extend to form one-dimensional sheets. If the size of the A cation is small enough, neighboring sheets will also be linked through their X corners, such that the A cation will be located in the cage shared by eight octahedra. Figure 1.2 shows another unit cell perovskite structure, where the BX_6 octahedron is surrounded by A atoms at the cube's corners (0, 0, 0). In this view, the B atom is located at the cube center ($\frac{1}{2}, \frac{1}{2}, \frac{1}{2}$), and X atoms are located on the cube face centers ($\frac{1}{2}, \frac{1}{2}, 0$), $(\frac{1}{2}, 0, \frac{1}{2})$, $(0, \frac{1}{2}, \frac{1}{2})$. This way of visualizing the perovskite unit cell is very useful to study possible lattice stability and deformations, as will be discussed below.

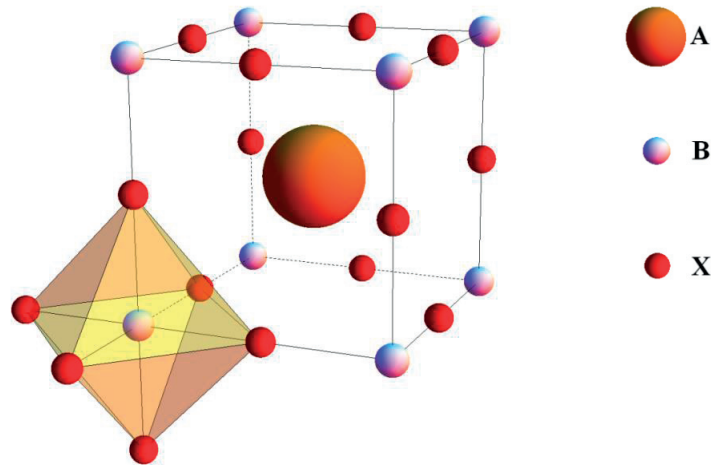


Figure 1.1 The ideal ABX_3 cubic crystalline structure. The A cation will be confined inside the interstice formed by eight BX_6 octahedra

Assuming a closed packed structure (assumption not implemented in Figure 1.2), the geometry of atomic positions in the lattice can be used to deduce relations between the atomic radii of constituting atoms (R_A , R_B , R_X). The B-X bond length of $a/2$ mentioned above and A-X bond length of $\frac{\sqrt{2}}{2}a$ result in the following relation:

$$t = \frac{R_A + R_X}{\sqrt{2} (R_B + R_X)} \quad (1.1)$$

where the parameter t is the Goldschmidt tolerance factor, and it equals unity for an ideal cubic perovskite structure. In other words, from Eq. 1.1, t measures the mismatch of charge equilibrium between the A-X bond length (nominator of Eq. 1.1) and the B-X bond length (denominator of Eq. 1.1) as a deviation from unity [27]. Ions with different sizes and affinities result in perovskite structures with different tolerance factors. Most importantly, a smaller A cation can result in octahedral tilt in a way that reduces t [28]. Other, less important, structural deviations also exist, such as B cation displacement and distortion of octahedra [5]. Also, as the ion size is reduced by lowering the temperature, which generally results in reducing t , a phase transition usually occurs between the high temperature cubic phase to less symmetric lower temperature tetragonal and orthorhombic phases [29]–[32].

The tolerance factor has been accepted for a long time to predict the possible formation and stability of ternary perovskite structures. However, although a necessary condition, the tolerance factor is not by itself sufficient for phase stability predication, and many other additional indicators have been proposed. One simple and effective method is to use the octahedral factor, μ , which measures the ratio between the B and X atoms in the BX_6 octahedra [33]:

$$\mu = \frac{R_B}{R_X} \quad (1.2)$$

There is a minimum value of μ , below which the BX_6 octahedral unit cannot form. For halide perovskites (i.e. $X = \text{halide}$), a minimum octahedral factor μ of 0.442 and a tolerance factor range of $0.81 < t < 1.11$ result in stable perovskite phases, with the high symmetry cubic phase most likely in the narrower range of $\sim 0.89 < t < 1.0$ [29], [33].

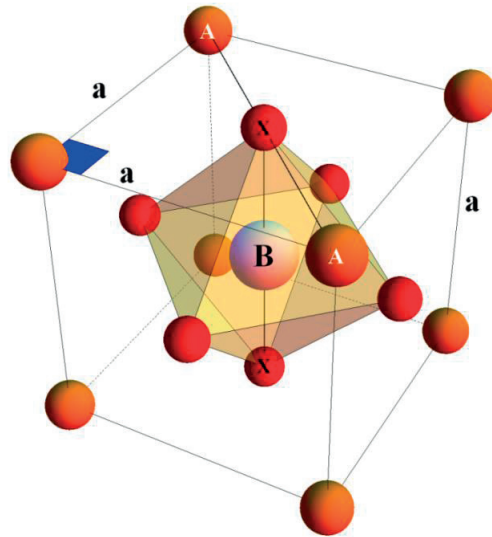


Figure 1.2 The BX_6 octahedron in a cubic perovskite structure. Assuming a closed packed structure (not implemented in the figure), the geometry of atomic positions in the lattice can be used to derive Eq. 1.1.

1.3 Organo Metal Halide Perovskites

Organo metal halide perovskites refer to a family of perovskites where the A cation is an organic molecule, B is a metal atom, and X is a halide atom (e.g. I, Br, Cl) in the ABX_3 structure. Therefore, they consist of inorganic sheets of metal halide corner-sharing octahedra (BX_6), which are separated by interstitials of organic molecules. The cubic perovskite structure can be kept with small organic molecules (Figure 1.3a); however, larger molecules can also be incorporated resulting in a layered structure of 2D inorganic/organic sheets as mentioned in Sec. 1.2, and as can be seen in Figure 1.3b. Based on the arrangement of energy levels for both the organic and inorganic layers, several self-assembling Quantum Well (QW) structures can be formed. For example, in the schematic diagrams of Figure 1.3b, the energy gap of the organic layer, determined by the energy difference between the highest occupied molecular orbital (HOMO) and the lowest unoccupied molecular orbital (LUMO), is assumed to be larger than the bandgap of the inorganic semiconductor layer, resulting in type I QW structure [6]. Other 2D perovskite QW structures have also been acknowledged [6].

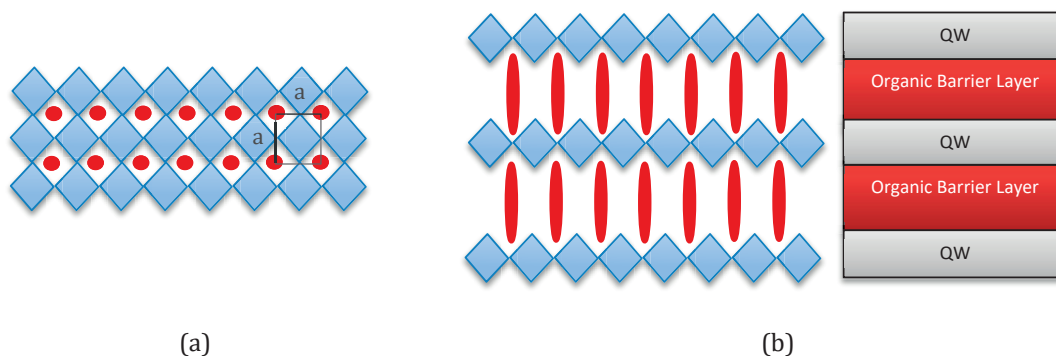


Figure 1.3 Schematic diagrams for 3D and 2D organo metal halide perovskites. Small organic A cations (red entities) allow the inorganic BX_6 octahedra to form a 3D network (a), while increasing the size of A results in organic/inorganic 2D structures (b).

The quantum confinement as well as the dielectric confinement of excitons in the QW structure of 2D organo metal halide perovskites significantly increase their exciton binding energies, up to a few hundreds of meV [34]–[36], which makes them less promising for photovoltaic applications. In photovoltaics, separation of excitons, or free e-h pairs, is the fundamental process that allows generation of the electrical current. 3D organo metal halide perovskites, i.e. the ones with small organic cations (Figure 1.3a), have much smaller, and sometimes negligible, exciton binding energies. In this thesis, 3D organo metal halide perovskites are studied, namely: methylammonium lead iodide $(CH_3NH_3)PbI_3 = MAPbI_3$, mixed $MAPbI_{3-x}Br_x$ (namely, $MAPbI_{3-x}Br_x$) and formamidinium lead bromide $CH(NH_2)_2PbBr_3 = FAPbBr_3$. For the rest of this thesis manuscript, unless otherwise stated, the word “perovskite” will be reserved for 3D organo metal halide perovskites.

1.4 Potential of Perovskites in Photovoltaic Applications

In a solar cell device, a light absorbing material absorbs solar photons to generate e-h pairs. A separation mechanism takes place after that to drive electrons and holes into two different pathways thus generating the electrical current. In most solar cell technologies, a semiconductor material plays the role of the solar light absorber (e.g. Si, GaAs, CdTe, CIGS, CZTS, quantum dots, and perovskite solar cells). The suitability of light absorber for light harvesting can be evaluated primarily by its bandgap; a smaller bandgap allows a wider absorption range of the solar spectrum at the cost of larger thermalization losses of hot carriers excited above the bandgap, and vice versa for a higher bandgap. This argument establishes one of the basic assumptions of the Shockley-Queisser limit (SQL), which calculates the maximum theoretical efficiency obtainable from a solar cell having a single light absorbing layer [37]. Figure 1.4 shows the theoretical SQ limit versus bandgap, along with highest experimentally obtained efficiencies for the main semiconductor-based solar cell technologies. A bandgap of ~ 1.5 eV coincides with the maximum

theoretically possible efficiency. The interest in perovskites primarily comes from the fact that bandgaps of some perovskites lie in that region (e.g. $\text{CH}_3\text{NH}_3\text{PbI}_3$, $E_g \sim 1.55\text{-}1.6$ eV).

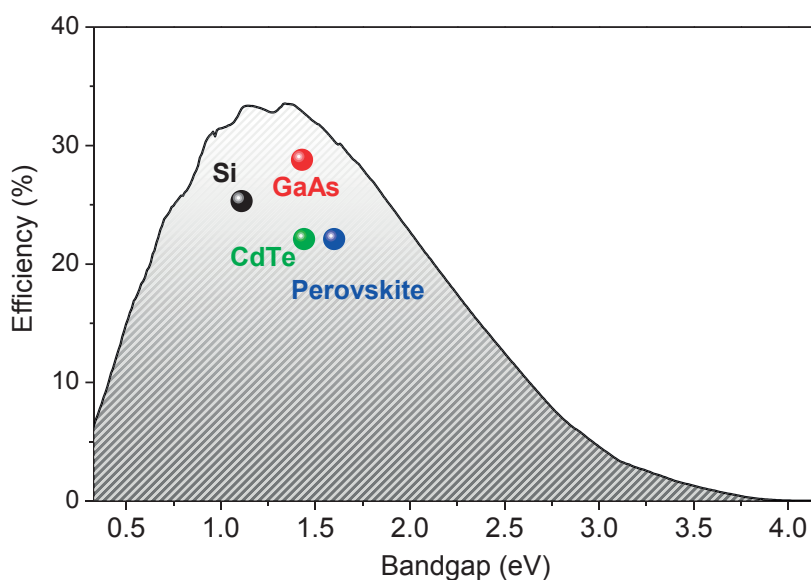


Figure 1.4 Calculated SQ limit as a function of bandgap. The curve was calculated assuming a step function for the semiconductor absorption switching from 0 to full absorption at E_g . The curve was generated using the solar spectrum data (AM1.5G) with ~ 1000 W/m^2 intensity available from the National Renewable Energy Laboratory (NREL) [38]. The bandgaps of Si, GaAs and CdTe (at 300 K) were taken from Ref. [39], while the bandgap of perovskite was taken to be 1.6 eV. The colored points in the graph shows the maximum experimentally recorded efficiencies for the above semiconductors [40], which can be compared with their theoretical SQ limits. See Chapter 3 for calculation details.

The band structure of semiconductors is another important factor to be considered. For example, in an indirect bandgap semiconductor, e.g. Si, solar light absorption is a second order process that involves a simultaneous absorption (emission) of a phonon, thus reducing the absorption coefficient and requiring a much thicker light absorbing layer. In direct bandgap semiconductor-based solar cells, a sub-micrometer absorber layer can be sufficient for complete solar light harvesting. Generated charges are also transported through the absorber layer in most solar cell structures, necessitating an improved material purity and increased processing costs.

Perovskites are direct bandgap semiconductors that can be prepared with high purity using low-cost chemical methods. This distinguishing advantage, besides foreseeing a promising future for perovskite solar cells, allowed massive material research from different research communities to be realized over the past few years. Only during the time frame of this thesis, numerous research results with thousands of publications and patents have appeared. From the material property side, tremendous research has emerged on a variety of perovskite materials, where a wide spectrum of material characterization

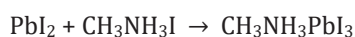
techniques has been implemented. In this thesis, photoluminescence (PL), cathodoluminescence (CL) and time-resolved photoluminescence (TRPL) techniques were mainly used to investigate the optical quality of MAPbI₃ and FAPbI₃ and MAPbI_{3-x}Br_x samples prepared under different conditions. A brief summary of the main physical properties of MAPbI₃, mixed MAPbI₃ and FAPbI₃ perovskites will be given below.

1.5 Methylammonium Lead Halide Perovskite (MAPbI₃)

MAPbI₃ is a direct bandgap semiconductor, with a bandgap of ~1.6 eV at room temperature [41]. Figure 1.5 shows the band structure of the room temperature tetragonal phase of MAPbI₃.

The methylammonium cation (CH₃NH₃⁺) has a molecular radius of R_{MA} = 0.18 nm according to Refs. [42], [43], and 0.217 nm according to Ref. [44]. Therefore, for MAPbI₃ perovskite, with R_{Pb} = 0.119 nm and R_I = 0.220 nm [45], the tolerance factor *t* and octahedral factor *μ* can be calculated to be 0.83-0.91 and 0.54 respectively. Due to the relatively small *t*, MAPbI₃ has a tetragonal crystalline phase at room temperature, which changes to pseudo-cubic at ~330K; below ~165K, a tetragonal-to-orthorhombic phase transition occurs [32], [46]–[48]. A summary of lattice parameters for the three crystalline phases is shown in Table 1.1.

MAPbI₃ can be experimentally synthesized using two precursor materials: lead iodide (PbI₂) and methylammonium iodide (CH₃NH₃I = MAI), according to the simple reaction:



The reaction enthalpy of the above reaction, i.e. the formation energy of CH₃NH₃PbI₃ perovskite from PbI₂ and CH₃NH₃I precursors, is calculated to be -0.1 eV [49]. This very small value has many direct and important impacts on the material characteristics. First, a facile formation of the perovskite phase can easily occur once PbI₂ and MAI precursors coexist in a reaction environment. Indeed, this has been one of the main advantages of perovskite solar cells, as low perovskite formation temperatures (down to room temperature) can still produce high efficiency solar cell devices [50]. Temperature is not the only stimulus that can activate the perovskite reaction above; a small pressure can also stimulate this reaction as can be revealed by the simple experiment shown in Figure 1.6. On the other side, however, this small formation energy is one of the main reasons behind perovskite phase instability towards surrounding conditions. First, separation of the perovskite phase into PbI₂ (solid) and MAI (vapor) is expected to be an exothermic process of a similar formation energy [51]. In addition, the low formation energy permits the perovskite and its MAI and PbI₂ precursors to coexist, a problem that has been well recognized for MAPbI₃ by the escape of MAI vapor and existence of residual PbI₂ even after long annealing times [50], [52], [53]. This intrinsic chemical instability is still one of the major drawbacks against long-term stability of MAPbI₃ perovskite based solar cells. Additionally, MAPbI₃ decomposition into PbI₂ is also reported to be highly driven by many environmental conditions such as moisture (see Refs. [54]–[58]), UV radiation (See Refs. [56], [59] and Chapter 4), oxygen in the ambient air [60] and temperature [55].

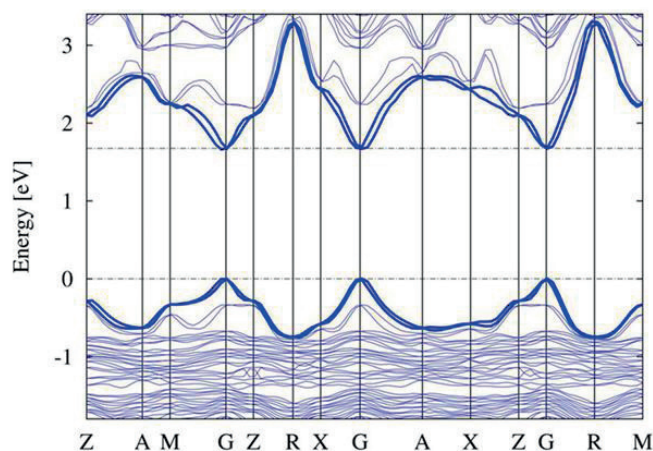


Figure 1.5 (from Ref. [41]) Calculated band structure of MAPbI₃ in the room-temperature tetragonal phase. Valence Band (VB) and Conduction Band (CB) are highlighted as thick solid lines.

Table 1.1 Lattice parameters of the three temperature-dependent crystalline phases of MAPbI₃, taken from Ref. [32].

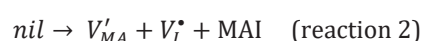
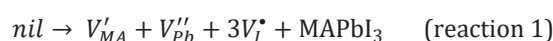
Crystalline System	Phase	Space group	Lattice Parameters (Å)
Cubic	α	$Pm\bar{3}m$	$a = 6.278(4)$ [measured at 353 K]
Tetragonal	β	$I4/mcm$	$a = 8.851(9)$ $c = 12.444(13)$ [measured at 298 K]
Orthorhombic	γ	$Pnma$	$a = 8.8362(11)$ $b = 12.5804(15)$ $c = 8.5551(10)$ [measured at 100 K]

Another potential source for MAPbI₃ instability is the methylammonium organic cation (MA). For a perfect cubic PbI₆-based perovskite structure with tolerance factor $\mu = 1$, the maximum radius available for the organic cation can be calculated, using Eq. 1.1, to be 0.26 nm. The small size of the MA cation (0.18 nm) allows MA cation movements in the interstice between the PbI₆ octahedra, which adds other degrees of freedom to the lattice system. In fact, several MA ion movements have been experimentally verified, e.g. C-N alignment and re-orientations along different directions in the octahedral interstice [47], [63]–[65] (whose activation energy is estimated to be 13 meV and 40 meV by Ref. [66] and Ref. [67] respectively), lower energy rotation around the C-N bond axis [47], and translational displacement inside the octahedral cage [47]. These experimentally verified movements add a substantial disorder to the crystalline system at room temperature.



Figure 1.6 An experiment showing the low formation energy of MAPbI₃ from PbI₂ and MAI precursors. The solid state reaction between PbI₂ (yellow powder) and MAI (white powder) immediately takes place by gentle grinding of the two precursors at room temperature using a mortar and pestle for ~ 1-2 minutes resulting in MAPbI₃ perovskite (black grey powder in the right image). As mentioned in the text, the formation energy for MAPbI₃ from PbI₂ and MAI is ~ 0.1 eV (compare it, for example, with > few eV for BaTiO₃ perovskite synthesized from TiO₂ and BaCO₃ precursors, which needs a much higher reaction temperature (above 800 °C) for the solid state reaction to take place [61], [62]).

Ionic conduction is another major source of phase instability in MAPbI₃. Anion-vacancy-assisted ion transport has been a well-known phenomenon with large diffusion coefficients for many inorganic oxide and halide perovskites [68]–[70]. It turned out that MAPbI₃ is not an exception, and iodine vacancy diffusion in MAPbI₃ has been theoretically predicted [71], and later verified experimentally by different groups [72], [73]. Schottky-type vacancies of anions and cations can readily form in MAPbI₃ with low formation energies [74], according to the following two reactions (in Kroger-Vink notation [75]):



where the symbols V'_{MA} , V''_{Pb} , V_I^* stand respectively for singly negatively charged MA vacancy, doubly negatively charged Pb vacancy and singly positively charged iodine vacancy.

The Schottky defect in reaction 1 has a small formation energy of 0.14 eV only, suggesting an equilibrium defect concentration of $2 \times 10^{19} \text{ cm}^{-3}$ at room temperature. The partial Schottky disorder described by reaction 2 has even a smaller formation energy of 0.08 eV and thus an equilibrium defect concentration of $2 \times 10^{20} \text{ cm}^{-3}$. This simply means that 4% of iodine and MA positions will be vacant in a stoichiometric perovskite lattice system, which establishes a rich environment for ionic conduction [74]. Interestingly, the energy levels of these vacancy defects have unusual properties. First, they make shallow energy levels at the band edges. Second, those energy levels are located inside the conduction and valence bands, and are not located in the mid-gap region. For example, the V'_{MA} defect makes an acceptor level at ~ 70 meV below the VB level, while the V_I^* defect makes a donor level at ~ 20 meV above the CB level [76]. Excited carriers can then relax from those shallow intra-band trap levels to the band edges. In other words,

despite their low formation energies compared to intra-band defects, which allows them to exist with high densities, these defects will not contribute to capturing the excited carriers and so to non-radiative recombination rates [49], [76]. It has to be mentioned here that mid-gap trap states are also possible to be created, but with formation energies higher than that of the Schottky system in reactions 1 & 2 above. In the same way, shallow mid-gap traps have less formation energies than deep ones, which further mitigates the overall trap scattering effects on carriers in MAPbI₃ perovskite [49], [76].

The likelihood to have a high density of “mobile” iodide vacancies with no carrier trapping consequences is a unique combination that could finally explain, at one stroke, many previously observed unusual photo-induced phenomena in though high quality MAPbI₃-based devices [77]–[81]. Briefly, when the perovskite solar cell device is illuminated, the photovoltage developed across the device terminals can activate the iodine vacancy migration, which has an activation energy (E_a) as low as 0.58 eV only [71]. This ionic conductivity results in slow photo-induced processes across the perovskite interfaces leading to many effects such as photo-induced giant dielectric constant [77], extremely slow photoconductivity response [78], unprecedented evolution of PL intensity over time [79], and most importantly the well-known problem of current-voltage hysteresis in perovskite solar cells [80], [81].

Many of the above phenomena were first explained by the high polarity of the MA ions that can, under light illumination, collectively align with the illumination field resulting in structural changes to the easily deformable perovskite structure [77]–[79]. The MA cation has a highly polar central C-N bond, with a dipole moment of 2.65 Debye [66] (to be compared with 1.85 Debye for H₂O and 1.91 Debye for HF). There are other implications of such a large dipole moment. From the prospective of the perovskite lattice system, the MA cation has a C_{3v} symmetry, which prevents the MAPbI₃ perovskite structure to possess an inversion symmetry center, and thus an ideal cubic structure. Even at high temperatures well above 330K, only a “pseudo-cubic” phase is achieved [32], [66]. This indeed promotes the possibility of having a polar crystalline structure and ferroelectricity behavior. Although polar MAPbI₃ crystalline structures were reported in some research works (P4mm was reported for the cubic phase [82], I4cm for the tetragonal phase [82] and Pna2₁ for the orthorhombic phase [63]), many other works reported nonpolar crystalline systems [32], [63], [83] as mentioned above. The lack of second harmonic generation efficiency in the work of Yamada et al [84] and Govinda et al [83] also supports this conclusion, adding further controversy to the polarity of the perovskite structure.

The next mobile defect in MAPbI₃ structure is MA vacancy, whose migration activation energy E_a is calculated to be 0.84 eV [71]. Migration of MA⁺ ions in MAPbI₃ was experimentally verified by Yuan et al [72]. However, in addition to its higher activation energy, the MA disorder at room temperature and the relatively complex process of MA diffusion between adjacent octahedral cages leave iodine vacancy diffusion as the dominant process [85].

The rate of ionic diffusion for a certain defect species (with a given concentration) can be obtained through the relation [86]:

$$k = \frac{k_B T}{\hbar} e^{-\frac{E_a}{RT}}$$

where k_B is Boltzman's constant, T is temperature, \hbar is the reduced Planck's constant, and R is the ideal gas constant. From the above relation, the diffusion rates are estimated at room temperature to be $\sim 6 \times 10^3 \text{ s}^{-1}$ and 0.25 s^{-1} for I^- and MA^+ vacancies respectively. The rate of ionic diffusion also depends on the available concentration of ionic defects (i.e. stoichiometry of original precursors and sample preparation conditions) and on the morphology (i.e. grain boundaries) of the perovskite sample, which can explain the large variation of reported hysteresis time constants [85]. The activation energy for Pb^{2+} vacancy is estimated to be 2.31 eV resulting in vacancy diffusion rate of $\sim 4 \times 10^{-26}$, which suggests an immobile Pb sublattice in the perovskite structure [71].

Now, the above-mentioned different sources of phase instability in MAPbI_3 perovskite did not prevent MAPbI_3 to remarkably keep the "champion's" position as a photovoltaic material among all other perovskites. The bandgap of MAPbI_3 , corresponding to a maximum SQ limit of $\sim 31\%$ located at the crest of the SQL efficiency curve (Figure 1.4), is an important pre-requisite for such success. The passivation of traps in this material, with such a low-energy and rich chemistry of defects, is another success parameter. Besides the shallow intra-band levels of defects with low formation energies mentioned above, other passivation mechanism(s) are also proposed in the literature [74], [87]–[89].

Another source behind the strong photovoltaic efficiency in MAPbI_3 comes from exciton dissociation and exciton binding energy. Despite the negative impacts of disorder caused by MA ion rotations and movements, these ultrafast molecular movements (e.g. 0.3-0.5 THz for molecular rotations [85]) are expected to cause ultrafast changes to the dielectric function, which can affect the long-term stability and properties of excitons [85], [90]. Also, the dominant dielectric screening produced by these freely moving polar ions reduces the exciton binding energy in the high temperature tetragonal and cubic phases of MAPbI_3 [91]–[93]. Therefore, the reduced exciton binding energy (down to 6 meV at room temperature [91]) and their easy dissociation provide a first step towards e-h separation necessary for the photovoltaic action to take place.

An important and striking property of MAPbI_3 is the unusual long diffusion length of both electrons and holes (exceeding $1 \mu\text{m}$ [94], [95] for polycrystalline films, and $175 \mu\text{m}$ for high quality single crystals [96]), which is significantly longer than the thickness required for almost complete absorption of the solar spectrum (absorption depth of MAPbI_3 is $\sim 100\text{-}200 \text{ nm}$ in the visible range [94], [95]). This long diffusion length for electrons and holes implies reduced e-h recombination events compared to traditional direct semiconductor materials. The small effective mass of electrons and holes (calculated by Ref. [97] for example to be $m_e^* \sim 0.23 m_e$, $m_h^* \sim 0.29 m_e$) and their decent mobilities [98]–[100] can only partially explain this property. The ultralow deep-level trap density that can be achieved in this solution-processed material (down to the order of 10^9 or 10^{10} cm^{-3} [96]), a consequence of the high formation energies required for deep-level mid-bandgap traps [49], [76], [101] discussed above, is another important property that can reduce the non-radiative monomolecular recombination of excited e-h pairs.

However, in addition to the weak trap-assisted recombination, the e-h bimolecular recombination is also shown to be greatly reduced in MAPbI₃ [66], [98], [102]–[109]. Many reasons have been proposed in the literature to explain the weak bimolecular recombination in MAPbI₃. First, the spatial separation of electrons and holes in the unit cell has been proposed by Wehrenfennig et al [98] as one of the reasons. Density functional calculations showed that the conduction band minimum consists mainly of 6p orbitals of lead (Pb), while the valence band maximum consists of mainly I 5p orbitals overlapping with less Pb 6s orbitals [67], [76], [110], [111], which reduces the spatial overlap between the electron and hole wavefunctions. Second, the local distribution of MA dipoles along with the octahedral distortions can also assist and explain the weak e-h bimolecular recombination. Frost et al [66] suggested the existence of ferroelectric domains, where each domain consists of a number of perovskite unit cells whose MA dipole moments are aligned in one direction. Electrons and holes in ferroelectric domains (with domains having possibly random net polarization directions) will first locally separate in the domain where they are created, and they will segregate after that in different pathways depending on the polarization directions of neighboring domains. This should result in a long-range separation of electrons and holes with even enhanced gained kinetic energy. This suggestion of Frost et al [66] was experimentally verified by the observation of ferroelectric domains of ~ 100 nm size that was reported later in the same year [112].

Bimolecular recombination can be further reduced, and carrier lifetime further enhanced, in the locally polarized domains by Rashba splitting of conduction and valence bands, as proposed first by Minsung Kim et al [102] and by others later on [103]–[105]. Rashba splitting occurs when an electric field results in symmetry breaking of spin-orbit coupling orbitals [113], [114]. Rashba splitting causes a spin-degenerate band to split into two bands in k-space. The strong spin-orbit coupling from the heavy elements in the perovskite can thus be affected by the local electric field in the polarized domain resulting in Rashba splitting of the valence and conduction bands. The structural distortion caused by the electric dipole and the dipole orientation with respect to the PbI₆ lattice are critical factors to determine the resulting “spin texture” of conduction and valence bands [102], [104]. The momentum splitting of bands transforms the direct bandgap into a slightly in-direct one, requiring the participation of phonon in the e-h recombination process in order to allow momentum conservation, hence reducing the recombination rate. Some dipole-lattice configurations can even result in spin-forbidden recombination channels, further enhancing the carrier lifetime. Giant Rashba splitting has been experimentally observed in MAPbBr₃ perovskite [115].

It has to be mentioned also that Rashba splitting is not the only way to realize direct-to-indirect bandgap transformation. The alignment of the MA polar molecule along certain directions in the octahedral cage can also result in an indirect bandgap structure, as theoretically suggested by Motta et al [106]. In their depiction, the ultrafast rotations of the MA molecule imply that MAPbI₃ will work as a “dynamical bandgap semiconductor” [106], whose bandgap depends on the dynamically changing direction of MA dipole moment.

The domain walls between adjacent domains can also play a vital role in enhancing the e-h separation process [107]. Also, Ma et al [108] theoretically predicted that spatial localization, within few

nanometers, of charge densities of the conduction and valence band edges can take place in MAPbI₃ and contribute to exciton dissociation, further reducing the e-h bimolecular recombination rates. This complicated process is suggested to originate from the random distribution of MA dipole moments, especially in the high temperature tetragonal and cubic phases [108].

The disorder provided by the MA cations could thus offset its undesirable instability impacts on the perovskite structure and proved advantageous for an efficient photovoltaic process to take place. It has to be mentioned here that some of the above mentioned possible scenarios behind the long lifetime of photocarriers in MAPbI₃ carry physical origins that should, in principle, apply to other perovskites having similar configurational and polar conditions. However, the long lifetime of photocarriers could also be demonstrated for perovskites with inorganic non-polar A cations, e.g. CsPbBr₃ [109]. This, indeed, puts some of the above-mentioned scenarios, which depends on the MA cation polarity, at stake. It, however, guides the attention towards other possible polar fluctuations and/or ion displacements in the perovskite lattice, with which photoexcited carriers can also be coupled [109], especially with the mechanical softness of the perovskite lattice in general [116].

In summary, MAPbI₃ can grow with high densities of iodide and MA ion vacancies, which result in serious instability problems. However, the effect of these vacancies on the transport of excited carriers is mitigated by the nature of their shallow intra-band energy levels. Bimolecular recombination is also reduced by several possible scenarios mentioned above. These properties explain the long carrier diffusion length in perovskite solar cells despite their strong instability issues.

As mentioned above, different kinds of mid-gap deep-level traps can also be created, however with higher formation energies. This provided, for example, a good chance to realize MAPbI₃ with low trap densities ($10^9 - 10^{10} \text{ cm}^{-3}$ demonstrated for example in Ref. [96]). Nevertheless, the trap densities have a large likelihood to be created using the currently used solution-processing techniques. Furthermore, it has been shown by Buin et al [49] that the formation energies of deep traps greatly depend on the initial preparation conditions. For example, Pb_I anti-site defect (i.e. I atom replacing Pb) has a formation energy of $\sim 0.2 \text{ eV}$ in I-rich solution environments, which can go higher to 0.38 eV under I-poor conditions. Therefore, high control of preparation conditions, employing solution-processing procedures, is a vital and at the same time difficult step to control the resulting trap densities in grown perovskite films. Indeed, as will be further discussed in Chapter 3, traps will then play the main role in determining the diffusion length and dynamics of excited carriers, directly impacting the main characteristics of the solar cell device, e.g. the open-circuit voltage (V_{oc}).

1.6 Mixed Halide MAPbI_{3-x}Br_x Perovskite

It has been shown above that the ionic transport in MAPbI₃ is allowed by the small activation energy of migration for iodide vacancies. This ability of migration can interestingly explain a class of chemical reactions in which halides can be easily replaced by each other [117]–[127]. Halide exchange reactions

have been demonstrated for many halide combinations [117], [118], [120]–[123], [125]–[127], where a halide anion can be exchanged simply by the introduction of another halide reservoir in a solution or a gas environment. The compositional exchange between the two halides is a spontaneous as well as reversible process [121], and it can be controllably designed, at will, to result in complete [127] or partial replacement [122], [125], [126]. This in fact confirms the less movable nature of the MA-Pb framework in the perovskite lattice, as discussed above. After partial or complete halide exchange, the resulting mixed halide perovskite should possess the tailored physical properties of the intentional halide compositions.

Anion exchange reactions have had interesting applications to control different properties of grown perovskite structures. For example, post-tuning of the perovskite bandgap can be performed while preserving a previously grown morphology using the halide to be replaced [122], [127]. Also, bandgap tuning, through halide exchange, over the entire visible range has been demonstrated for different perovskites [117], [118], [122], [125], [126]. In addition, halide exchange is reported to result in improved robustness of the finally resulting perovskite material against ambient conditions such as moisture [117] and in improved solar cell device efficiency as well [128]–[130].

Photoexcited carrier lifetimes are also reported to be enhanced by halide mixing. For example, the diffusion length of electrons and holes in $\text{MAPbI}_{3-x}\text{Cl}_x$ is reported by Stranks et al [95] to be ~ 10 times longer than in MAPbI_3 . It is interesting to mention that $\text{MAPbI}_{3-x}\text{Cl}_x$ perovskite, resulting from $\text{I}_{3-x}/\text{Cl}_x$ halide mixing, usually produce almost Cl-free perovskite [131] with no change in the bandgap, and it however carries improved carrier lifetime and device performance compared to pristine MAPbI_3 . Several explanations have been proposed to explain the role of Cl doping in enhancing such e-h separation processes [49], [101], [131]–[134]. Here, we refer to the work of Buin et al [49], who showed that the existence of Cl^- ions ultimately result in reducing the concentration of I^- ions in the growth solution during the perovskite growth process, for which the formation energy of some defects, e.g. Pb_I anti-site, increases.

Compared to I/Cl^- halide mixing, I/Br^- mixing have been shown by many authors to be highly miscible resulting in controllable bandgap tuning of the resulting $\text{MAPbI}_{3-x}\text{Br}_x$ perovskite over a wide visible range (~ 1.6 to 2.3 eV) [117], [119], [123], [127], [135]–[137]. However, even a small I/Br^- ratio ($x \sim 0$), which preserves the bandgap of MAPbI_3 , was shown by Dar et al [129] to be determining for the growth of fascinating $\text{MAPbI}_{3-x}\text{Br}_x$ single micro-crystals, and for improving the power conversion efficiency of respective solar cell devices. These $\text{MAPbI}_{3-x}\text{Br}_x$ micro-crystals are studied in Chapter 5 of this manuscript by cathodoluminescence (CL) mapping and energy dispersive X-ray spectroscopy, with which local optical quality of the microcubes could be evaluated.

It has to be finally mentioned that the advantage offered by the efficient halide migration in perovskites, which allows halide exchange reactions mentioned above to be realized, can however be counterpoised by the possibility of halide segregation in the mixed halide alloy [139]–[142]. The constituting halides can segregate, upon photoexcitation [139], [140], [143] or e-beam excitation [143], [144], into different regions creating halide-rich domains of each constituting halide. Also, intensive halide mixing (i.e. for $x \sim 0.5$) is reported to result in severe drop in charge carrier mobilities [145]. As will be

seen in Chapter 5, halide exchange can also result in substantial elemental inhomogeneity in the grown microcrystals.

1.7 Effects of Organic Cation Replacements: Formamidinium vs. Methylammonium

DFT calculations on MAPbI_3 show that the organic cation molecule negligibly contributes to the density of states in both the valence and conduction bands [67], [76], [110], [111], [146]. The electronic states of the organic cation are located far from the bandgap (see Figure 1.7), leaving the PbI_6 structure effectively negatively ionized. In fact, assuming corner-sharing connectivity between adjacent octahedra from all directions (which is the defining condition for 3D perovskites), it can be shown that replacing the organic cation by a positive background in the DFT calculations results in a similar band structure [146], which can be seen in Figure 1.7.

Based on the above argument, it could be validated that the bandgap of PbX_6 structure can be highly altered, and uniquely determined, over a range of ~ 1 eV, by the changing the Pb-X-Pb angles only [146], [147]. Indeed, the Pb-X-Pb angles will define the tilt of PbX_6 octahedra as well as the size of the octahedral cage enclosing the organic cation. Decreasing the Pb-X-Pb angles will decrease the size of the octahedral cage, and vice versa. More importantly, a shorter Pb-X-Pb will directly increase the bandgap. For a perfect cubic structure, the Pb-X-Pb angle is 180° . This high range of bandgap tunability inspired many studies to explore the possible mechanisms and approaches for such an “intrinsic” bandgap tuning [146]–[149].

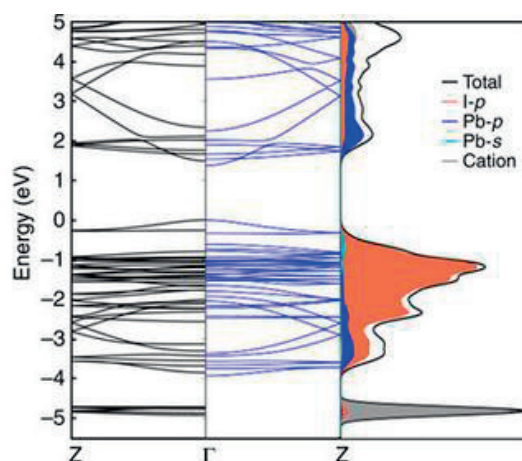


Figure 1.7 Calculated band structures for MAPbI_3 , with the MA organic cation (black, left) and without it (blue, middle), in the low temperature orthorhombic phase. The density of states originating from the I 5p (which dominates the valence band), Pb 6p (which dominates the conduction band), Pb 6s, and CH_3NH_3^+ are shown on the right. It can be noticed that the electronic states of the MA cation are very localized far below the valence band. The graph is taken from Ref. [146].

Indeed, the size and polarity of the organic cation is capable of changing the Pb-X-Pb angles, and it has been theoretically shown that the bandgap of MAPbI₃ can be altered between 1.1-1.9 eV when organic molecules of different sizes are placed in the octahedral cavity [146]. Therefore, besides the disorder it may impose to the structure, discussed in Sec. 1.5, the organic cation can have strong steric effects that can directly alter the perovskite bandgap.

Compared to methylammonium [CH₃NH₃⁺ = MA], the formamidinium cation [CH(NH₂)₂⁺ = FA], see Figure 1.8, has a larger size (0.253 nm for FA compared to 0.217 for MA according to Ref. [44]). Therefore, when MA is replaced by the FA cation, the Pb-X-Pb angles are expected to expand resulting in a smaller band gap. For example, compared to MAPbI₃, whose bandgap is ~ 1.6 eV, FAPbI₃ has a bandgap of ~ 1.48 eV, which lies at the optimal point for the maximum theoretical efficiency in the SQ limit curve (Figure 1.4). The structural properties can also be affected by the cation replacement. For example, the Goldschmidt tolerance factor for FAPbI₃ can be calculated from the above ionic radii to be 0.99, for which, unlike the tetragonal phase of MAPbI₃, FAPbI₃ is expected to have a cubic phase at room temperature.

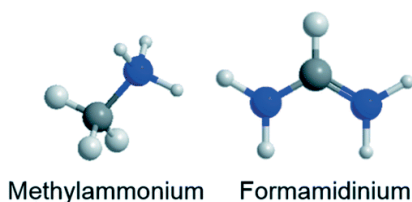


Figure 1.8 (from Ref. [150]) The molecular structure of Methylammonium (MA) and Formamidinium (FA).

The perovskite structure is also reported to gain strikingly improved order and stability when MA is replaced by the FA cation [66], [151], [152]. Similar to the discussion on the disorder offered by the MA cation (see Sec. 1.5), this can be explained by the intrinsic properties of the FA cation itself. First, the polarity of formamidinium is around one order of magnitude less than that of methylammonium (0.24 Debye for FA compared to 2.65 Debye for MA [66]), which implies much less polarity effects on the crystalline positions and subsequent band structural changes. Also, FA is a heavier molecule with a C_{2v} symmetry, which makes it assume a central as well as less movable position in the octahedral cage [66], [151], [152]. The energy barrier of rotation is estimated for FA to be 144 meV which is one order of magnitude higher than that of MA (13 meV) [66]. This restriction of the molecular motion is even enhanced by the possibility to have larger number of hydrogen bonds, with shorter bond lengths, between the FA cation and the surrounding inorganic lattice [152], further stabilizing the structure.

1.8 Formamidinium Lead Bromide (FAPbBr₃)

Starting from MAPbI₃, FAPbBr₃ can be formed by replacing both the organic cation (MA by FA) and the halide (I by Br). Compared to the iodide ion, the bromide ion Br⁻ has a smaller radius, which is expected

to decrease the lattice constant and thus increase the bandgap. As can be consulted in Sec. 1.6, I/Br halide mixing in $\text{MAPbI}_{3-x}\text{Br}_x$ systems can tune the band gap over a wide visible range between 1.6 to ~ 2.3 eV.

MAPbBr_3 and FAPbBr_3 have very similar properties and crystalline structures. Both MAPbBr_3 and FAPbBr_3 have a bandgap energy of ~ 2.3 eV [151]. Taking $R_{\text{MA}} = 0.217$ nm, $R_{\text{FA}} = 0.253$ nm [44], $R_{\text{Pb}} = 0.119$ nm, and $R_{\text{Br}} = 0.196$ nm [45], the Goldschmidt tolerance factor can be calculated for MAPbBr_3 and FAPbBr_3 to be 0.93 and 1.01 respectively. Therefore, both perovskites assume the cubic phase at room temperature, as has been experimentally verified, with a space group of $Pm-3m$ [151], [153], and unit cell parameters of $a = 5.923(1)$ Å for MAPbBr_3 and $a = 5.992(1)$ Å for FAPbBr_3 [151]. Compared to iodide-based perovskites, the exciton binding energy is reported to be higher for both MAPbBr_3 and FAPbBr_3 perovskites than iodine counterparts, which is usually manifested by a clear exciton absorption peak in their absorption spectra even at room temperature [154], [155].

However, compared to MAPbBr_3 , FAPbBr_3 showed a higher phase stability [148], [149], [151], [156], a superior (one order of magnitude) charge carrier diffusion length [151], [153], and a noticeably lower trap density [153]. Those interesting properties have recently made FAPbBr_3 a focus for many research efforts. In fact, the bandgap of FAPbBr_3 (reported to be in the range ~ 2.15 - 2.3 (see for example Refs. [151], [153], [157])) is clearly not sufficient for high efficiency single-junction solar cells. For example, the best efficiencies achieved using bromide based perovskites is ~ 7 - 8% [151], [156], [158], with a maximum possible efficiency of 16.4% (See Chapter 3). However, it provides a low-cost option as a top cell in a tandem solar cell structure [159], with a much higher potential for light emitting applications, as will be discussed in the next section.

1.9 Potential of FAPbBr_3 in Light Emission Applications

As mentioned above, the mitigated traps and slow radiative bimolecular recombination, resulting in long electron and hole diffusion lengths and decent mobilities of charge carriers, are key properties for the striking success of perovskites as solar light harvesting materials. In fact, perovskites also showed to have slow Auger recombination at high densities of photoexcited carriers as well [160]. Interestingly, these properties are also what is required for an efficient semiconductor laser/LED. Additionally, as will be discussed in Chapter 3, for a direct bandgap semiconductor, the demonstration of strong light absorption in a solar cell device should be reflected in efficient light emission characteristics as well.

The year 2014 witnessed the beginning of a very rapidly increasing number of studies on the enormous potential for different perovskite materials as optical gain mediums [160]–[166]. As a signature of stimulated emission, amplified spontaneous emission (ASE) has been already evidenced for perovskites in cavity-free configuration [160], [161], [164], [165], [167], [168], different resonating configurations [162], [163], [169]–[172] as well as in random networks of nanocrystals [166]. Indeed, the simple chemical synthesis of perovskites has been an important factor to realize perovskite lasing in such a variety of configurations.

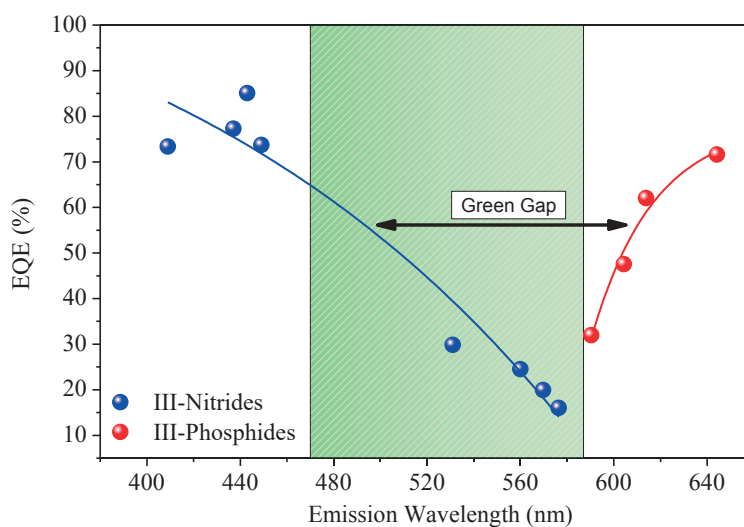


Figure 1.9 Maximum external quantum efficiency (EQE) for III-nitride and III-phosphide LEDs, demonstrating the “green gap” problem. The data points are taken from Ref. [175]. The red and blue lines are guides to the eye. The shaded region is the color range that can be covered by FAPbBr₃ micro and nanocrystals, according to Refs. [151], [153], [157], [173].

The bandgap of bulk FAPbBr₃ is experimentally reported to be ~ 2.15 - 2.3 eV [151], [153], [157], [173] which can be further increased for FAPbBr₃ nanocrystals [174]. As can be seen in Figure 1.9, the reported band-to-band emission of FAPbBr₃ (bulk and nanocrystals) is reported to lie in the range of 470-587 nm [151], [153], [174] nicely covering the “green gap” color region, in which technological limitations prevent the realization of efficient light emitters using traditionally available technologies [175], [176]. The reported high quantum yield from FAPbBr₃ (up to 85% [174]), its simple and low-cost fabrication technologies and wide emission tunability makes FAPbBr₃ among one of the promising light emitting materials in the future. Indeed, FAPbBr₃ has been currently receiving an uprising attention for LED/lasing applications [158], [174], [177]–[180].

1.10 Description of Subsequent Chapters

This thesis mainly covers three optical studies on different organo lead halide perovskites. The optical studies were carried out mainly using photoluminescence (PL), cathodoluminescence (CL) and time-resolved photoluminescence (TRPL) techniques. Chapter 2 describes the three experimental setups. Chapter 3 presents a detailed study on the photovoltaic and amplified spontaneous emission (ASE) of FAPbBr₃ films prepared using different solvent environments. The solvents used are shown to be detrimental for both the morphology and optical quality of the prepared films. The optical quality is evaluated using TRPL, and was used, based on fundamental detailed balance principles of absorption/emission, to estimate the maximum possible V_{OC} of respective solar cell devices under the ideal

radiative limit and in the presence of trap densities as well. Solar cell devices were fabricated, by the group of Prof. Nazeeruddin, EPFL, using the same FAPbBr₃ films, and a record V_{OC} , at the time of publication, of 1.42 V was obtained, and was higher than the typically reported values of the built-in potential set by the device contacts. Perceptions about the charge separation mechanisms in perovskite solar cells are accordingly discussed. Amplified spontaneous emission (ASE) is, for the first time, demonstrated for FAPbBr₃ in this work. The effects of solvent, hole transport layer and excitation wavelengths on the ASE threshold carrier density are investigated. Bandgap renormalization (BGR) was observed as a red-shift in the ASE peak with increasing the excited carrier density, and was estimated to be $\sim 5-7 \times 10^{-9}$ eV.cm.

Chapter 4 mainly addresses a TRPL study on the UV-induced damage in MAPbI₃. UV-induced damage was observed both in bulk MAPbI₃ films (deposited on glass slides) and at MAPbI₃/TiO₂ and MAPbI₃/Al₂O₃ interfaces. Interestingly, the UV-induced damage switches off when samples are cooled to ~ 200 K. Temperature-dependent TRPL measurements were also carried out, and provided additional insights. The possible UV degradation mechanisms are accordingly discussed.

In Chapter 5, a CL study performed on MAPbI_{3-x}Br_x micro-cubic crystals is presented. Thanks to substrate cooling, polychromatic CL maps could be successfully obtained despite the immense damage that has been caused by the electron beam radiation. The CL maps showed an asymmetric emission across the microcrystals, where the emission was highly diminished in the center of the micro-cube, and intensely dominant at the periphery. STEM-EDS maps could clearly attribute this asymmetric emission to the non-homogeneous distribution of methylammonium. Monte Carlo simulations of electron trajectories and CL emission were performed under different acceleration voltages, and the possible carrier recombination pathways are discussed. Chapter 6 gives a summary of the key results and main conclusions in this thesis. It also discusses some conceivable future perspectives.

References

- [1] G. Rose, "Der Perowskit, eine neue Mineralgattung," *Ann. Phys.*, vol. 48, pp. 558, 1839.
- [2] V. M. Goldschmidt, "Die Gesetze der Krystallochemie," *Naturwissenschaften*, vol. 14, no. 21, pp. 477–485, 1926.
- [3] H. D. Megaw, "Crystal structure of barium titanate," *Nature*, vol. 155, no. 3938, pp. 484–485, 1945.
- [4] A. M. Glazer, "The classification of tilted octahedra in perovskites," *Acta Crystallogr. Sec. B*, vol. 28, no. 11, pp. 3384–3392, 1972.
- [5] A. M. Glazer, "Simple ways of determining perovskite structures," *Acta Crystallogr. Sect. A*, vol. 31, no. 6, pp. 756–762, 1975.
- [6] D. B. Mitzi, K. Chondroudis, and C. R. Kagan, "Organic-inorganic electronics," *IBM J. Res. Dev.*, vol. 45, no. 1, pp. 29–45, 2001.
- [7] D. B. Mitzi, "Solution-processed inorganic semiconductors," *J. Mater. Chem.*, vol. 14, no. 15, pp. 2355, 2004.
- [8] D. B. Mitzi, "Templating and structural engineering in organic-inorganic perovskites," *J. Chem. Soc. Dalton Trans.*, vol. 9, no. 1, pp. 1–12, 2001.
- [9] D. B. Mitzi, "Synthesis, Structure, and Properties of Organic-Inorganic Perovskites and Related Materials," *Progress in Inorganic Chemistry*, vol. 48, pp. 1-121, 2007.
- [10] L. J. De Jongh, P. Bloembergen, and J. H. P. Colpa, "Transition temperatures of weakly anisotropic layer-type magnets. Dependence on anisotropy," *Physica*, vol. 58, no. 2, pp. 305–314, 1972.
- [11] R. D. Willett and E. F. Riedel, "A neutron diffraction study of the crystal structures and magnetic studies of $(\text{NH}_3\text{CH}_2\text{CH}_2\text{CH}_2\text{NH}_3)\text{MnCl}_4$ and $(\text{NH}_3\text{CH}_2\text{CH}_2\text{NH}_3)\text{FeCl}_4$: Layer structures with two-dimensional magnetic interactions," *Chem. Phys.*, vol. 8, no. 1–2, pp. 112–122, 1975.
- [12] W. D. van Amstel and L. J. de Jongh, "Magnetic measurements on $(\text{CH}_3\text{NH}_3)_2\text{MnCl}_4$, a quasi two-dimensional Heisenberg antiferromagnet," *Solid State Commun.*, vol. 11, no. 10, pp. 1423–1429, 1972.
- [13] C. R. Kagan, D. B. Mitzi, and C. D. Dimitrakopoulos, "Organic-Inorganic Hybrid Materials as Semiconducting Channels in Thin-Film Field-Effect Transistors," *Science*, vol. 286, no. 5441, pp. 945–947, 1999.
- [14] T. Kondo, T. Azuma, T. Yuasa, and R. Ito, "Biexciton lasing in the layered perovskite-type material $(\text{C}_6\text{H}_{13}\text{NH}_3)_2\text{PbI}_4$," *Solid State Commun.*, vol. 105, no. 4, pp. 253–255, 1998.
- [15] M. Era, S. Morimoto, T. Tsutsui, and S. Saito, "Organic-inorganic heterostructure electroluminescent device using a layered perovskite semiconductor $(\text{C}_6\text{H}_5\text{C}_2\text{H}_4\text{NH}_3)_2\text{PbI}_4$," *Appl. Phys. Lett.*, vol. 65, no. 6, pp. 676, 1994.
- [16] X. Hong, T. Ishihara, and A. V. Nurmikko, "Photoconductivity and electroluminescence in lead iodide based natural quantum well structures," *Solid State Commun.*, vol. 84, no. 6, pp. 657–661, 1992.
- [17] C. Xu, T. Kondo, H. Sakakura, K. Kumata, Y. Takahashi, and R. Ito, "Optical third-harmonic generation in layered perovskite-type material $(\text{C}_{10}\text{H}_{21}\text{NH}_3)_2\text{PbI}_4$," *Solid State Commun.*, vol. 79, no. 3, pp. 245–248, 1991.
- [18] T. Ishihara, J. Takahashi, and T. Goto, "Optical properties due to electronic transitions in two-dimensional semiconductors $(\text{C}_n\text{H}_{2n+1}\text{NH}_3)_2\text{PbI}_4$," *Phys. Rev. B*, vol. 42, no. 17, pp. 11099–11107, 1990.
- [19] A. Kojima, K. Teshima, T. Miyasaka, and Y. Shirai, "Novel photoelectrochemical cell with mesoscopic electrodes sensitized by lead-halide compounds (2)," in *Meeting Abstracts*, The Electrochemical Society, no. 7, pp. 397, 2006.
- [20] A. Kojima, K. Teshima, Y. Shirai, and T. Miyasaka, "Novel photoelectrochemical cell with mesoscopic electrodes sensitized by lead-halide compounds (5)," in *Meeting Abstracts*, The Electrochemical Society, no. 8, pp. 352, 2007.

- [21] A. Kojima, K. Teshima, Y. Shirai, and T. Miyasaka, "Novel photoelectrochemical cell with mesoscopic electrodes sensitized by lead-halide compounds (11)," in *Meeting Abstracts*, The Electrochemical Society, no. 1, pp. 27, 2008.
- [22] T. Miyasaka, A. Kojima, and K. Teshima, "Lead halide perovskites as quantum dot sensitizers for mesoscopic TiO₂ photovoltaic cells," in *Meeting Abstracts*, The Electrochemical Society, no. 9, pp. 742, 2009.
- [23] A. Kojima, K. Teshima, Y. Shirai, and T. Miyasaka, "Organometal Halide Perovskites as Visible-Light Sensitizers for Photovoltaic Cells," *J. Am. Chem. Soc.*, vol. 131, no. 17, pp. 6050–6051, 2009.
- [24] J.-H. Im, C.-R. Lee, J.-W. Lee, S.-W. Park, and N.-G. Park, "6.5% efficient perovskite quantum-dot-sensitized solar cell," *Nanoscale*, vol. 3, pp. 4088-4093, 2011.
- [25] H.-S. Kim, C.-R. Lee, J.-H. Im, K.-B. Lee, T. Moehl, A. Marchioro, S.-J. Moon, R. Humphry-Baker, J.-H. Yum, J. E. Moser, M. Graetzel, and N.-G. Park, "Lead Iodide Perovskite Sensitized All-Solid-State Submicron Thin Film Mesoscopic Solar Cell with Efficiency Exceeding 9%," *Sci. Rep.*, vol. 2, pp. 583–585, 2012.
- [26] M. M. Lee, J. Teuscher, T. Miyasaka, T. N. Murakami, and H. J. Snaith, "Efficient Hybrid Solar Cells Based on Meso-Superstructured Organometal Halide Perovskites," *Science*, vol. 338, no. 6107, pp. 643–647, 2012.
- [27] S. L. Cooper, T. Egami, J. B. Goodenough, and J.-S. Zhou, *Localized to itinerant electronic transition in perovskite oxides* (vol. 98). Springer, 2003.
- [28] D. G. Billing and A. Lemmerer, "Inorganic–organic hybrid materials incorporating primary cyclic ammonium cations: The lead iodide series," *CrystEngComm*, vol. 9, no. 3, pp. 236–244, 2007.
- [29] M. A. Green, A. Ho-Baillie, and H. J. Snaith, "The emergence of perovskite solar cells," *Nat. Photonics*, vol. 8, no. 7, pp. 506–514, 2014.
- [30] R. E. Cohen, "Origin of ferroelectricity in perovskite oxides," *Nature*, vol. 358, no. 6382, pp. 136–138, 1992.
- [31] S. A. T. Redfern, "High-temperature structural phase transitions in perovskite," *J. Phys. Condens. Matter*, vol. 8, no. 43, pp. 8267–8275, 1996.
- [32] T. Baikie, Y. Fang, J. M. Kadro, M. Schreyer, F. Wei, S. G. Mhaisalkar, M. Graetzel, and T. J. White, "Synthesis and crystal chemistry of the hybrid perovskite (CH₃NH₃)PbI₃ for solid-state sensitised solar cell applications," *J. Mater. Chem. A*, vol. 1, no. 18, pp. 5628, 2013.
- [33] C. Li, X. Lu, W. Ding, L. Feng, Y. Gao, and Z. Guo, "Formability of ABX₃ (X = F, Cl, Br, I) halide perovskites," *Acta Crystallogr. Sect. B Struct. Sci.*, vol. 64, no. 6, pp. 702–707, 2008.
- [34] E. Hanamura, N. Nagaosa, M. Kumagai, and T. Takagahara, "Quantum wells with enhanced exciton effects and optical non-linearity," *Mater. Sci. Eng. B*, vol. 1, no. 3, pp. 255–258, 1988.
- [35] X. Hong, T. Ishihara, and A. V. Nurmikko, "Dielectric confinement effect on excitons in PbI₄-based layered semiconductors," *Phys. Rev. B*, vol. 45, no. 12, pp. 6961–6964, 1992.
- [36] K. Tanaka, T. Takahashi, T. Kondo, K. Umeda, K. Ema, T. Umebayashi, K. Asai, K. Uchida, and N. Miura, "Electronic and Excitonic Structures of Inorganic–Organic Perovskite-Type Quantum-Well Crystal (C₄H₉NH₃)₂PbBr₄," *Jpn. J. Appl. Phys.*, vol. 44, no. 8, pp. 5923–5932, 2005.
- [37] W. Shockley and H. J. Queisser, "Detailed Balance Limit of Efficiency of p-n Junction Solar Cells," *J. Appl. Phys.*, vol. 32, no. 3, pp. 510, 1961.
- [38] "Reference Solar Spectral Irradiance: Air Mass 1.5.," Renewable Resource Data Center, National Renewable Energy Laboratory (NREL), [Online]. Available on the website link: <http://rredc.nrel.gov/solar/spectra/am1.5/> [Accessed: 13-Dec-2016].
- [39] C. Kittel, *Introduction to Solid State Physics, Eight Edition*. John Wiley & Sons, 2005.

- [40] "Best Research Cell Efficiency Chart", National Renewable Energy Laboratory (NREL), [Online]. Available on the website link: <https://www.nrel.gov/pv/assets/images/efficiency-chart.png> [Accessed: 13-Dec-2016].
- [41] P. Umari, E. Mosconi, and F. De Angelis, "Relativistic GW calculations on $\text{CH}_3\text{NH}_3\text{PbI}_3$ and $\text{CH}_3\text{NH}_3\text{SnI}_3$ Perovskites for Solar Cell Applications," *Sci. Rep.*, vol. 4, pp. 6050–6051, 2014.
- [42] B. N. Cohen, C. Labarca, N. Davidson, and H. A. Lester, "Mutations in M2 alter the selectivity of the mouse nicotinic acetylcholine receptor for organic and alkali metal cations," *J. Gen. Physiol.*, vol. 100, no. 3, pp. 373–400, 1992.
- [43] N. K. McKinnon, D. C. Reeves, and M. H. Akabas, "5-HT₃ receptor ion size selectivity is a property of the transmembrane channel, not the cytoplasmic vestibule portals," *J. Gen. Physiol.*, vol. 138, no. 4, pp. 453–466, 2011.
- [44] P. P. Boix, S. Agarwala, T. M. Koh, N. Mathews, and S. G. Mhaisalkar, "Perovskite Solar Cells: Beyond Methylammonium Lead Iodide," *J. Phys. Chem. Lett.*, vol. 6, no. 5, pp. 898–907, 2015.
- [45] R. D. Shannon, "Revised Effective Ionic Radii and Systematic Studies of Interatomic Distances in Halides and Chalcogenides," *Acta Crystallogr. Sect. A*, vol. 32, no. 5, pp. 751–767, 1976.
- [46] S. Govinda, P. Mahale, B. P. Kore, S. Mukherjee, M. S. Pavan, C. De, S. Ghara, A. Sundaresan, A. Pandey, T. N. G. Row, and D. D. Sarma, "Is $\text{CH}_3\text{NH}_3\text{PbI}_3$ Polar?," *J. Phys. Chem. Lett.*, vol. 7, no. 13, pp. 2412–2419, 2016.
- [47] M. T. Weller, O. J. Weber, P. F. Henry, A. M. D. Pumpo, and T. C. Hansen, "Complete structure and cation orientation in the perovskite photovoltaic methylammonium lead iodide between 100 and 352 K," *Chem. Commun.*, vol. 51, no. 20, pp. 4180–4183, 2015.
- [48] A. Poglitsch and D. Weber, "Dynamic disorder in methylammoniumtrihalogenoplumbates (II) observed by millimeter-wave spectroscopy," *J. Chem. Phys.*, vol. 87, no. 11, pp. 6373–6378, 1987.
- [49] A. Buin, P. Pietsch, J. Xu, O. Voznyy, A. H. Ip, R. Comin, and E. H. Sargent, "Materials processing routes to trap-free halide perovskites," *Nano Lett.*, vol. 14, no. 11, pp. 6281–6286, 2014.
- [50] J. Burschka, N. Pellet, S.-J. Moon, R. Humphry-Baker, P. Gao, M. K. Nazeeruddin, and M. Graetzel, "Sequential deposition as a route to high-performance perovskite-sensitized solar cells," *Nature*, vol. 499, no. 7458, pp. 316–319, 2013.
- [51] Y.-Y. Zhang, S. Chen, P. Xu, H. Xiang, X.-G. Gong, A. Walsh, and S.-H. Wei, "Intrinsic Instability of the Hybrid Halide Perovskite Semiconductor $\text{CH}_3\text{NH}_3\text{PbI}_3$," *arXiv preprint arXiv: 1506.01301*, 2015.
- [52] S. M. H. Qaid, M. S. Al Sobaie, M. A. M. Khan, I. M. Bedja, F. H. Alharbi, M. K. Nazeeruddin, and A. S. Aldwayyan, "Band-gap tuning of lead halide perovskite using a single step spin-coating deposition process," *Mater. Lett.*, vol. 164, pp. 498–501, 2016.
- [53] Z. Song, S. C. Watthage, A. B. Phillips, B. L. Tompkins, R. J. Ellingson, and M. J. Heben, "Impact of Processing Temperature and Composition on the Formation of Methylammonium Lead Iodide Perovskites," *Chem. Mater.*, vol. 27, no. 13, pp. 4612–4619, 2015.
- [54] A. M. A. Leguy, Y. Hu, M. Campoy-Quiles, M. I. Alonso, O. J. Weber, P. Azarhoosh, M. van Schilfgaarde, M. T. Weller, T. Bein, J. Nelson, P. Docampo, and P. R. F. Barnes, "Reversible Hydration of $\text{CH}_3\text{NH}_3\text{PbI}_3$ in Films, Single Crystals, and Solar Cells," *Chem. Mater.*, vol. 27, no. 9, pp. 3397–3407, 2015.
- [55] Y. Han, S. Meyer, Y. Dkhissi, K. Weber, J. M. Pringle, U. Bach, L. Spiccia, and Y.-B. Cheng, "Degradation observations of encapsulated planar $\text{CH}_3\text{NH}_3\text{PbI}_3$ perovskite solar cells at high temperatures and humidity," *J. Mater. Chem. A*, vol. 3, no. 15, pp. 8139–8147, 2015.
- [56] G. Niu, W. Li, F. Meng, L. Wang, H. Dong, and Y. Qiu, "Study on the stability of $\text{CH}_3\text{NH}_3\text{PbI}_3$ films and the effect of post-modification by aluminum oxide in all-solid-state hybrid solar cells," *J. Mater. Chem. A*, vol. 2, no. 3, pp. 705–710, 2014.

- [57] J. Zhao, B. Cai, Z. Luo, Y. Dong, Y. Zhang, H. Xu, B. Hong, Y. Yang, L. Li, W. Zhang, and C. Gao, "Investigation of the Hydrolysis of Perovskite Organometallic Halide $\text{CH}_3\text{NH}_3\text{PbI}_3$ in Humidity Environment," *Sci. Rep.*, vol. 6, pp. 21976, 2016.
- [58] J. Yang, B. D. Siempelkamp, D. Liu, and T. L. Kelly, "Investigation of $\text{CH}_3\text{NH}_3\text{PbI}_3$ Degradation Rates and Mechanisms in Controlled Humidity Environments Using *in Situ* Techniques," *ACS Nano*, vol. 9, no. 2, pp. 1955–1963, 2015.
- [59] T. Leijtens, G. E. Eperon, S. Pathak, A. Abate, M. M. Lee, and H. J. Snaith, "Overcoming ultraviolet light instability of sensitized TiO_2 with meso-superstructured organometal tri-halide perovskite solar cells," *Nat. Commun.*, vol. 4, pp. 583–585, 2013.
- [60] A. J. Pearson, G. E. Eperon, P. E. Hopkinson, S. N. Habisreutinger, J. T.-W. Wang, H. J. Snaith, and N. C. Greenham, "Oxygen Degradation in Mesoporous $\text{Al}_2\text{O}_3/\text{CH}_3\text{NH}_3\text{PbI}_{3-x}\text{Cl}_x$ Perovskite Solar Cells: Kinetics and Mechanisms," *Adv. Energy Mater.*, vol. 6, no. 13, pp. 1600014, 2016.
- [61] T. Kozawa, A. Onda, and K. Yanagisawa, "Accelerated formation of barium titanate by solid-state reaction in water vapour atmosphere," *J. Eur. Ceram. Soc.*, vol. 29, no. 15, pp. 3259–3264, 2009.
- [62] M. T. Buscaglia, M. Bassoli, V. Buscaglia, and R. Alessio, "Solid-State Synthesis of Ultrafine BaTiO_3 Powders from Nanocrystalline BaCO_3 and TiO_2 ," *J. Am. Ceram. Soc.*, vol. 88, no. 9, pp. 2374–2379, 2005.
- [63] A. Poglitsch and D. Weber, "Dynamic disorder in methylammoniumtrihalogenoplumbates (II) observed by millimeter-wave spectroscopy," *J. Chem. Phys.*, vol. 87, no. 11, p. 6373, 1987.
- [64] O. Knop, R. E. Wasylishen, M. A. White, T. S. Cameron, and M. J. M. Van Oort, "Alkylammonium lead halides. Part 2. $\text{CH}_3\text{NH}_3\text{PbX}_3$ (X=Cl, Br, I) perovskites: cuboctahedral halide cages with isotropic cation reorientation," *Can. J. Chem.*, vol. 68, no. 3, pp. 412–422, 1990.
- [65] A. M. A. Leguy, J. M. Frost, A. P. McMahon, V. G. Sakai, W. Kockelmann, C. Law, X. Li, F. Foglia, A. Walsh, B. C. O'Regan, J. Nelson, J. T. Cabral, and P. R. F. Barnes, "The dynamics of methylammonium ions in hybrid organic-inorganic perovskite solar cells," *Nat. Commun.*, vol. 6, pp. 7124, 2015.
- [66] J. M. Frost, K. T. Butler, F. Brivio, C. H. Hendon, M. Van Schilfgaarde, and A. Walsh, "Atomistic origins of high-performance in hybrid halide perovskite solar cells," *Nano Lett.*, vol. 14, no. 5, pp. 2584–2590, 2014.
- [67] F. Brivio, A. B. Walker, and A. Walsh, "Structural and electronic properties of hybrid perovskites for high-efficiency thin-film photovoltaics from first-principles," *APL Mater.*, vol. 1, no. 4, pp. 14–19, 2013.
- [68] L. Malavasi, C. A. J. Fisher, and M. S. Islam, "Oxide-ion and proton conducting electrolyte materials for clean energy applications: structural and mechanistic features," *Chem. Soc. Rev.*, vol. 39, no. 11, pp. 4370–4387, 2010.
- [69] J. Mizusaki, K. Arai, and K. Fueki, "Ionic conduction of the perovskite-type halides," *Solid State Ionics*, vol. 11, no. 3, pp. 203–211, 1983.
- [70] J. B. Goodenough, "Electronic and ionic transport properties and other physical aspects of perovskites," *Reports Prog. Phys.*, vol. 67, no. 11, pp. 1915–1993, 2004.
- [71] C. Eames, J. M. Frost, P. R. F. Barnes, B. C. O'Regan, A. Walsh, and M. S. Islam, "Ionic transport in hybrid lead iodide perovskite solar cells," *Nat. Commun.*, vol. 6, pp. 7497, 2015.
- [72] Y. Yuan, Q. Wang, Y. Shao, H. Lu, T. Li, A. Gruverman, and J. Huang, "Electric-field-driven reversible conversion between methylammonium lead triiodide perovskites and lead iodide at elevated temperatures," *Adv. Energy Mater.*, vol. 6, no. 2, pp. 1501803, 2016.
- [73] D. W. deQuilettes, W. Zhang, V. M. Burlakov, D. J. Graham, T. Leijtens, A. Osherov, V. Bulović, H. J. Snaith, D. S. Ginger, and S. D. Stranks, "Photo-induced halide redistribution in organic-inorganic perovskite films," *Nat. Commun.*, vol. 7, pp. 11683, 2016.
- [74] A. Walsh, D. O. Scanlon, S. Chen, X. G. Gong, and S.-H. Wei, "Self-Regulation Mechanism for Charged Point

- Defects in Hybrid Halide Perovskites," *Angew. Chem., Int. Ed.*, vol. 127, no. 6, pp. 1811-1814, 2015.
- [75] F. A. Kröger and H. J. Vink, "Relations between the Concentrations of Imperfections in Crystalline Solids," *Solid State Phys.*, vol. 3, pp. 307-435, 1956.
- [76] W.-J. Yin, T. Shi, and Y. Yan, "Unusual defect physics in $\text{CH}_3\text{NH}_3\text{PbI}_3$ perovskite solar cell absorber," *Appl. Phys. Lett.*, vol. 104, no. 6, pp. 063903, 2014.
- [77] E. J. Juarez-Perez, R. S. Sanchez, L. Badia, G. Garcia-Belmonte, Y. S. Kang, I. Mora-Sero, and J. Bisquert, "Photoinduced Giant Dielectric Constant in Lead Halide Perovskite Solar Cells," *J. Phys. Chem. Lett.*, vol. 5, no. 13, pp. 2390-2394, 2014.
- [78] R. Gottesman, E. Haltzi, L. Gouda, S. Tirosh, Y. Bouhadana, A. Zaban, E. Mosconi, and F. De Angelis, "Extremely Slow Photoconductivity Response of $\text{CH}_3\text{NH}_3\text{PbI}_3$ Perovskites Suggesting Structural Changes under Working Conditions," *J. Phys. Chem. Lett.*, vol. 5, no. 15, pp. 2662-2669, 2014.
- [79] R. S. Sanchez, V. Gonzalez-Pedro, J.-W. Lee, N.-G. Park, Y. S. Kang, I. Mora-Sero, and J. Bisquert, "Slow Dynamic Processes in Lead Halide Perovskite Solar Cells. Characteristic Times and Hysteresis," *J. Phys. Chem. Lett.*, vol. 5, no. 13, pp. 2357-2363, 2014.
- [80] E. L. Unger, E. T. Hoke, C. D. Bailie, W. H. Nguyen, A. R. Bowring, T. Heumüller, M. G. Christoforo, and M. D. McGehee, "Hysteresis and transient behavior in current-voltage measurements of hybrid-perovskite absorber solar cells," *Energy Environ. Sci.*, vol. 7, no. 11, pp. 3690-3698, 2014.
- [81] S. Meloni, T. Moehl, W. Tress, M. Franckevičius, M. Saliba, Y. H. Lee, P. Gao, M. K. Nazeeruddin, S. M. Zakeeruddin, U. Rothlisberger, and M. Graetzel, "Ionic polarization-induced current-voltage hysteresis in $\text{CH}_3\text{NH}_3\text{PbX}_3$ perovskite solar cells," *Nat. Commun.*, vol. 7, pp. 10334, 2016.
- [82] C. C. Stoumpos, C. D. Malliakas, and M. G. Kanatzidis, "Semiconducting tin and lead iodide perovskites with organic cations: Phase transitions, high mobilities, and near-infrared photoluminescent properties," *Inorg. Chem.*, vol. 52, no. 15, pp. 9019-9038, 2013.
- [83] S. Govinda, P. Mahale, B. P. Kore, S. Mukherjee, M. S. Pavan, C. De, S. Ghara, A. Sundaresan, A. Pandey, T. N. G. Row, and D. D. Sarma, "Is $\text{CH}_3\text{NH}_3\text{PbI}_3$ Polar?," *J. Phys. Chem. Lett.*, vol. 7, no. 13, pp. 2412-2419, 2016.
- [84] Y. Yamada, T. Yamada, L. Q. Phuong, N. Maruyama, H. Nishimura, A. Wakamiya, Y. Murata, and Y. Kanemitsu, "Dynamic Optical Properties of $\text{CH}_3\text{NH}_3\text{PbI}_3$ Single Crystals as Revealed by One- and Two-photon Excited Photoluminescence Measurements," *J. Am. Chem. Soc.*, vol. 137, no. 33, pp. 10456-10459, 2015.
- [85] J. M. Frost and A. Walsh, "What Is Moving in Hybrid Halide Perovskite Solar Cells?," *Accounts of Chemical Research*, vol. 49, no. 3, pp. 528-535, 2016.
- [86] J. M. Azpiroz, E. Mosconi, J. Bisquert, and F. De Angelis, "Defect migration in methylammonium lead iodide and its role in perovskite solar cell operation," *Energy Environ. Sci.*, vol. 8, no. 7, pp. 2118-2127, 2015.
- [87] Q. Chen, H. Zhou, T.-B. Song, S. Luo, Z. Hong, H.-S. Duan, L. Dou, Y. Liu, and Y. Yang, "Controllable self-induced passivation of hybrid lead iodide perovskites toward high performance solar cells," *Nano Lett.*, vol. 14, no. 7, pp. 4158-4163, 2014.
- [88] L. Wang, C. McCleese, A. Kovalsky, Y. Zhao, and C. Burda, "Femtosecond Time-Resolved Transient Absorption Spectroscopy of $\text{CH}_3\text{NH}_3\text{PbI}_3$ Perovskite Films: Evidence for Passivation Effect of PbI_2 ," *J. Am. Chem. Soc.*, vol. 136, no. 35, pp. 12205-12208, 2014.
- [89] J. Kim, S. H. Lee, J. H. Lee, and K. H. Hong, "The role of intrinsic defects in methylammonium lead iodide perovskite," *J. Phys. Chem. Lett.*, vol. 5, no. 8, pp. 1312-1317, 2014.
- [90] E. Menéndez-Proupin, C. L. B. Ríos, and P. Wahnón, "Nonhydrogenic exciton spectrum in perovskite $\text{CH}_3\text{NH}_3\text{PbI}_3$," *Phys. Status Solidi - Rapid Res. Lett.*, vol. 9, no. 10, pp. 559-563, 2015.
- [91] A. Miyata, A. Mitioglu, P. Plochocka, O. Portugall, J. T.-W. Wang, S. D. Stranks, H. J. Snaith, and R. J. Nicholas,

- "Direct measurement of the exciton binding energy and effective masses for charge carriers in organic-inorganic tri-halide perovskites," *Nat. Phys.*, vol. 11, no. 7, pp. 582–587, 2015.
- [92] J. Even, L. Pedesseau, and C. Katan, "Analysis of multivalley and multibandgap absorption and enhancement of free carriers related to exciton screening in hybrid perovskites," *J. Phys. Chem. C*, vol. 118, no. 22, pp. 11566–11572, 2014.
- [93] Y. Yamada, T. Nakamura, M. Endo, A. Wakamiya, and Y. Kanemitsu, "Photoelectronic responses in solution-processed perovskite $\text{CH}_3\text{NH}_3\text{PbI}_3$ solar cells studied by photoluminescence and photoabsorption spectroscopy," *IEEE J. Photovoltaics*, vol. 5, no. 1, pp. 401–405, 2015.
- [94] G. Xing, N. Mathews, S. Sun, S. S. Lim, Y. M. Lam, M. Grätzel, S. Mhaisalkar, and T. C. Sum, "Long-range balanced electron- and hole-transport lengths in organic-inorganic $\text{CH}_3\text{NH}_3\text{PbI}_3$," *Science*, vol. 342, no. 6156, pp. 344–347, 2013.
- [95] S. D. Stranks, G. E. Eperon, G. Grancini, C. Menelaou, M. J. P. Alcocer, T. Leijtens, L. M. Herz, A. Petrozza, and H. J. Snaith, "Electron-hole diffusion lengths exceeding 1 micrometer in an organometal trihalide perovskite absorber," *Science*, vol. 342, no. 6156, pp. 341–344, 2013.
- [96] Q. Dong, Y. Fang, Y. Shao, P. Mulligan, J. Qiu, L. Cao, and J. Huang, "Electron-hole diffusion lengths $> 175 \mu\text{m}$ in solution-grown $\text{CH}_3\text{NH}_3\text{PbI}_3$ single crystals," *Science*, vol. 347, no. 6225, pp. 967–970, 2015.
- [97] G. Giorgi, J. I. Fujisawa, H. Segawa, and K. Yamashita, "Small photocarrier effective masses featuring ambipolar transport in methylammonium lead iodide perovskite: A density functional analysis," *J. Phys. Chem. Lett.*, vol. 4, no. 24, pp. 4213–4216, 2013.
- [98] C. Wehrenfennig, G. E. Eperon, M. B. Johnston, H. J. Snaith, and L. M. Herz, "High charge carrier mobilities and lifetimes in organolead trihalide perovskites," *Adv. Mater.*, vol. 26, no. 10, pp. 1584–1589, 2014.
- [99] T. Zhao, W. Shi, J. Xi, D. Wang, and Z. Shuai, "Intrinsic and Extrinsic Charge Transport in $\text{CH}_3\text{NH}_3\text{PbI}_3$ Perovskites Predicted from First-Principles," *Sci. Rep.*, vol. 7, pp. 19968, 2016.
- [100] T. M. Brenner, D. A. Egger, A. M. Rappe, L. Kronik, G. Hodes, and D. Cahen, "Are Mobilities in Hybrid Organic-Inorganic Halide Perovskites Actually 'High'?", *Journal of Physical Chemistry Letters*, vol. 6, no. 23, pp. 4754–4757, 2015.
- [101] M. H. Du, "Efficient carrier transport in halide perovskites: theoretical perspectives," *J. Mater. Chem. A*, vol. 2, no. 24, pp. 9091–9098, 2014.
- [102] M. Kim, J. Im, A. J. Freeman, J. Ihm, and H. Jin, "Switchable $S = 1/2$ and $J = 1/2$ Rashba bands in ferroelectric halide perovskites," *Proc. Natl. Acad. Sci. U. S. A.*, vol. 111, no. 19, pp. 6900–6904, 2014.
- [103] A. Amat, E. Mosconi, E. Ronca, C. Quarti, P. Umari, M. K. Nazeeruddin, M. Grätzel, and F. De Angelis, "Cation-induced band-gap tuning in organohalide perovskites: Interplay of spin-orbit coupling and octahedra tilting," *Nano Lett.*, vol. 14, no. 6, pp. 3608–3616, 2014.
- [104] F. Zheng, L. Z. Tan, S. Liu, and A. M. Rappe, "Rashba spin-orbit coupling enhanced carrier lifetime in $\text{CH}_3\text{NH}_3\text{PbI}_3$," *Nano Lett.*, vol. 15, no. 12, pp. 7794–7800, 2015.
- [105] C. Quarti, E. Mosconi, and F. De Angelis, "Interplay of orientational order and electronic structure in methylammonium lead iodide: Implications for solar cell operation," *Chem. Mater.*, vol. 26, no. 22, pp. 6557–6569, 2014.
- [106] C. Motta, F. El-Mellouhi, S. Kais, N. Tabet, F. Alharbi, and S. Sanvito, "Revealing the role of organic cations in hybrid halide perovskite $\text{CH}_3\text{NH}_3\text{PbI}_3$," *Nat. Commun.*, vol. 6, pp. 7026, 2015.
- [107] S. Liu, F. Zheng, N. Z. Koocher, H. Takenaka, F. Wang, and A. M. Rappe, "Ferroelectric Domain Wall Induced Band Gap Reduction and Charge Separation in Organometal Halide Perovskites," *J. Phys. Chem. Lett.*, vol. 6, no. 4, pp. 693–699, 2015.

- [108] J. Ma and L. W. Wang, "Nanoscale charge localization induced by random orientations of organic molecules in hybrid perovskite $\text{CH}_3\text{NH}_3\text{PbI}_3$," *Nano Lett.*, vol. 15, no. 1, pp. 248–253, 2015.
- [109] H. Zhu, M. T. Trinh, J. Wang, Y. Fu, P. P. Joshi, K. Miyata, S. Jin, and X.-Y. Zhu, "Organic Cations Might Not Be Essential to the Remarkable Properties of Band Edge Carriers in Lead Halide Perovskites," *Adv. Mater.*, vol. 29, no. 1, pp. 1603072, 2016.
- [110] Y. Wang, T. Gould, J. F. Dobson, H. Zhang, H. Yang, X. Yao, and H. Zhao, "Density functional theory analysis of structural and electronic properties of orthorhombic perovskite $\text{CH}_3\text{NH}_3\text{PbI}_3$," *Phys. Chem. Chem. Phys.*, vol. 16, no. 4, pp. 1424–1429, 2014.
- [111] W. J. Yin, T. Shi, and Y. Yan, "Unique properties of halide perovskites as possible origins of the superior solar cell performance," *Adv. Mater.*, vol. 26, no. 27, pp. 4653–4658, 2014.
- [112] Y. Kutes, L. Ye, Y. Zhou, S. Pang, B. D. Huey, and N. P. Padture, "Direct observation of ferroelectric domains in solution-processed $\text{CH}_3\text{NH}_3\text{PbI}_3$ perovskite thin films," *J. Phys. Chem. Lett.*, vol. 5, no. 19, pp. 3335–3339, 2014.
- [113] Y. A. Bychkov and E. I. Rashba, "Properties of a 2D electron gas with lifted spectral degeneracy," *JETP Letters*, vol. 39, no. 2, pp. 78–81, 1984.
- [114] Y. A. Bychkov and E. I. Rashba, "Oscillatory effects and the magnetic susceptibility of carriers in inversion layers," *J. Phys. C Solid State Phys.*, vol. 17, no. 33, pp. 6039–6045, 1984.
- [115] D. Niesner, M. Wilhelm, L. Levchuk, A. Osvet, S. Shrestha, M. Batentschuk, C. Brabec, and T. Fauster, "Giant Rashba Splitting in $\text{CH}_3\text{NH}_3\text{PbBr}_3$ Organic-Inorganic Perovskite," *Phys. Rev. Lett.*, vol. 117, no. 12, pp. 126401, 2016.
- [116] Y. Rakita, S. R. Cohen, N. K. Kedem, G. Hodes, and D. Cahen, "Mechanical properties of APbX_3 (A = Cs or CH_3NH_3 ; X = I or Br) perovskite single crystals," *MRS Commun.*, vol. 5, no. 4, pp. 623–629, 2015.
- [117] J. H. Noh, S. H. Im, J. H. Heo, T. N. Mandal, and S. Il Seok, "Chemical management for colorful, efficient, and stable inorganic-organic hybrid nanostructured solar cells," *Nano Lett.*, vol. 13, no. 4, pp. 1764–1769, 2013.
- [118] S. A. Kulkarni, T. Baikie, P. P. Boix, N. Yantara, N. Mathews, and S. Mhaisalkar, "Band-gap tuning of lead halide perovskites using a sequential deposition process," *J. Mater. Chem. A*, vol. 2, pp. 9221–9225, 2014.
- [119] A. Sadhanala, F. Deschler, T. H. Thomas, S. E. Dutton, K. C. Goedel, F. C. Hanusch, M. L. Lai, U. Steiner, T. Bein, P. Docampo, D. Cahen, and R. H. Friend, "Preparation of Single Phase Films of $\text{CH}_3\text{NH}_3\text{Pb}(\text{I}_{1-x}\text{Br}_x)_3$ with Sharp Optical Band Edges," *J. Phys. Chem. Lett.*, vol. 5, no. 15, pp. 2501–2505, 2014.
- [120] N. Pellet, J. Teuscher, J. Maier, and M. Grätzel, "Transforming hybrid organic inorganic perovskites by rapid halide exchange," *Chem. Mater.*, vol. 27, no. 6, pp. 2181–2188, 2015.
- [121] G. Li, J. Y. L. Ho, M. Wong, and H. S. Kwok, "Reversible Anion Exchange Reaction in Solid Halide Perovskites and Its Implication in Photovoltaics," *J. Phys. Chem. C*, vol. 119, no. 48, pp. 26883–26888, 2015.
- [122] D. Zhang, Y. Yang, Y. Bekenstein, Y. Yu, N. A. Gibson, A. B. Wong, S. W. Eaton, N. Kornienko, Q. Kong, M. Lai, A. P. Alivisatos, S. R. Leone, and P. Yang, "Synthesis of Composition Tunable and Highly Luminescent Cesium Lead Halide Nanowires through Anion-Exchange Reactions," *J. Am. Chem. Soc.*, vol. 138, no. 23, pp. 7236–7239, 2016.
- [123] L. Gil-Escrig, A. Miquel-Sempere, M. Sessolo, and H. J. Bolink, "Mixed Iodide-Bromide Methylammonium Lead Perovskite-based Diodes for Light Emission and Photovoltaics," *J. Phys. Chem. Lett.*, vol. 6, no. 18, pp. 3743–3748, 2015.
- [124] D. Solis-Ibarra, I. C. Smith, and H. I. Karunadasa, "Post-synthetic halide conversion and selective halogen capture in hybrid perovskites," *Chem. Sci.*, vol. 6, no. 7, pp. 4054–4059, 2015.
- [125] Q. A. Akkerman, V. D'Innocenzo, S. Accornero, A. Scarpellini, A. Petrozza, M. Prato, and L. Manna, "Tuning the optical properties of cesium lead halide perovskite nanocrystals by anion exchange reactions," *J. Am. Chem. Soc.*, vol. 137, no. 32, pp. 10276–10281, 2015.

- [126] G. Nedelcu, L. Protesescu, S. Yakunin, M. I. Bodnarchuk, M. J. Grotevent, and M. V. Kovalenko, "Fast Anion-Exchange in Highly Luminescent Nanocrystals of Cesium Lead Halide Perovskites (CsPbX_3 , $X = \text{Cl, Br, I}$)," *Nano Lett.*, vol. 15, no. 8, pp. 5635–5640, 2015.
- [127] A. B. Wong, M. Lai, S. W. Eaton, Y. Yu, E. Lin, L. Dou, A. Fu, and P. Yang, "Growth and Anion Exchange Conversion of $\text{CH}_3\text{NH}_3\text{PbX}_3$ Nanorod Arrays for Light-Emitting Diodes," *Nano Lett.*, vol. 15, pp. 5519–5524, 2015.
- [128] S. Colella, E. Mosconi, P. Fedeli, A. Listorti, F. Gazza, F. Orlandi, P. Ferro, T. Besagni, A. Rizzo, G. Calestani, G. Gigli, F. De Angelis, and R. Mosca, "MAPbI_{3-x}Cl_x Mixed Halide Perovskite for Hybrid Solar Cells: The Role of Chloride as Dopant on the Transport and Structural Properties," *Chem. Mater.*, vol. 25, no. 22, pp. 4613–4618, 2013.
- [129] M. Ibrahim Dar, M. Abdi-Jalebi, N. Arora, T. Moehl, M. Grätzel, and M. K. Nazeeruddin, "Understanding the Impact of Bromide on the Photovoltaic Performance of $\text{CH}_3\text{NH}_3\text{PbI}_3$ Solar Cells," *Adv. Mater.*, vol. 27, no. 44, pp. 7221–7228, 2015.
- [130] Y. Zhao and K. Zhu, " $\text{CH}_3\text{NH}_3\text{Cl}$ -assisted one-step solution growth of $\text{CH}_3\text{NH}_3\text{PbI}_3$: Structure, charge-carrier dynamics, and photovoltaic properties of perovskite solar cells," *J. Phys. Chem. C*, vol. 118, no. 18, pp. 9412–9418, 2014.
- [131] M. I. Dar, N. Arora, P. Gao, S. Ahmad, M. Grätzel, and M. K. Nazeeruddin, "Investigation regarding the role of chloride in organic-inorganic halide perovskites obtained from chloride containing precursors," *Nano Lett.*, vol. 14, no. 12, pp. 6991–6996, 2014.
- [132] N. Yantara, F. Yanan, C. Shi, H. A. Dewi, P. P. Boix, S. G. Mhaisalkar, and N. Mathews, "Unravelling the Effects of Cl Addition in Single Step $\text{CH}_3\text{NH}_3\text{PbI}_3$ Perovskite Solar Cells," *Chem. Mater.*, vol. 27, no. 7, pp. 2309–2314, 2015.
- [133] S. T. Williams, F. Zuo, C. C. Chueh, C. Y. Liao, P. W. Liang, and A. K. Y. Jen, "Role of chloride in the morphological evolution of organo-lead halide perovskite thin films," *ACS Nano*, vol. 8, no. 10, pp. 10640–10654, 2014.
- [134] Y. Tidhar, E. Edri, H. Weissman, D. Zohar, G. Hodes, D. Cahen, B. Rybtchinski, and S. Kirmayer, "Crystallization of Methyl Ammonium Lead Halide Perovskites : Implications for Photovoltaic Applications," *J. Am. Chem. Soc.*, vol. 136, no. 38, pp. 13249–13256, 2014.
- [135] P. Fedeli, F. Gazza, D. Calestani, P. Ferro, T. Besagni, A. Zapettini, G. Calestani, E. Marchi, P. Ceroni, and R. Mosca, "Influence of the Synthetic Procedures on the Structural and Optical Properties of Mixed-Halide (Br, I) Perovskite Films," *J. Phys. Chem. C*, vol. 119, no. 37, pp. 21304–21313, 2015.
- [136] N. J. Jeon, J. H. Noh, Y. C. Kim, W. S. Yang, S. Ryu, and S. Il Seok, "Solvent engineering for high-performance inorganic-organic hybrid perovskite solar cells," *Nat. Mater.*, vol. 13, pp. 897–903, 2014.
- [137] Z. Yang, C.-C. Chueh, P.-W. Liang, M. Crump, F. Lin, Z. Zhu, and A. K.-Y. Jen, "Effects of formamidinium and bromide ion substitution in methylammonium lead triiodide toward high-performance perovskite solar cells," *Nano Energy*, vol. 22, pp. 328–337, 2016.
- [138] M. I. Dar, G. Jacopin, M. Hezam, N. Arora, S. M. Zakeeruddin, B. Deveaud, M. K. Nazeeruddin, and M. Grätzel, "Asymmetric Cathodoluminescence Emission in $\text{CH}_3\text{NH}_3\text{PbI}_{3-x}\text{Br}_x$ Perovskite Single Crystals," *ACS Photonics*, vol. 3, no. 6, pp. 947–952, 2016.
- [139] E. T. Hoke, D. J. Slotcavage, E. R. Dohner, A. R. Bowring, H. I. Karunadasa, and M. D. McGehee, "Reversible photo-induced trap formation in mixed-halide hybrid perovskites for photovoltaics," *Chem. Sci.*, vol. 6, no. 1, pp. 613–617, 2015.
- [140] S. J. Yoon, S. Draguta, J. S. Manser, O. Sharia, W. F. Schneider, M. Kuno, and P. V. Kamat, "Tracking Iodide and Bromide Ion Segregation in Mixed Halide Lead Perovskites during Photoirradiation," *ACS Energy Lett.*, vol. 1, no. 1, pp. 290–296, 2016.
- [141] F. Brivio, C. Caetano, and A. Walsh, "Thermodynamic Origin of Photoinstability in the $\text{CH}_3\text{NH}_3\text{Pb}(\text{I}_{1-x}\text{Br}_x)_3$ Hybrid Halide Perovskite Alloy," *J. Phys. Chem. Lett.*, vol. 7, no. 6, pp. 1083–1087, 2016.
- [142] J. S. Yun, J. Seidel, J. Kim, A. M. Soufiani, S. Huang, J. Lau, N. J. Jeon, S. Il Seok, M. A. Green, and A. Ho-Baillie,

- "Critical Role of Grain Boundaries for Ion Migration in Formamidinium and Methylammonium Lead Halide Perovskite Solar Cells," *Adv. Energy Mater.*, vol. 6, no. 13, pp. 1600330, 2016.
- [143] H. Yuan, E. Debroye, K. Janssen, H. Naiki, C. Steuwe, G. Lu, M. Moris, E. Orgiu, H. Uji-i, F. De Schryver, P. Samorì, J. Hofkens, and M. Roeffaers, "Degradation of Methylammonium Lead Iodide Perovskite Structures through Light and Electron Beam Driven Ion Migration," *J. Phys. Chem. Lett.*, vol. 7, no. 3, pp. 561–566, 2016.
- [144] O. Hentz, Z. Zhao, and S. Gradečak, "Impacts of Ion Segregation on Local Optical Properties in Mixed Halide Perovskite Films," *Nano Lett.*, vol. 16, no. 2, pp. 1485–1490, 2016.
- [145] W. Rehman, R. I. Milot, G. E. Eperon, C. Wehrenfennig, J. L. Boland, H. J. Snaith, M. B. Johnston, and L. M. Herz, "Charge-Carrier Dynamics and Mobilities in Formamidinium Lead Mixed-Halide Perovskites," *Adv. Mater.*, vol. 27, no. 48, pp. 7938–7944, 2015.
- [146] M. R. Filip, G. E. Eperon, H. J. Snaith, and F. Giustino, "Steric Engineering of Metal-halide Perovskites with Tunable Optical Band Gaps," *Nat. Commun.*, vol. 5, pp. 5757, 2014.
- [147] J. L. Knutson, J. D. Martin, and D. B. Mitzi, "Tuning the band gap in hybrid tin iodide perovskite semiconductors using structural templating," *Inorg. Chem.*, vol. 44, no. 13, pp. 4699–4705, 2005.
- [148] I. P. Swainson, M. G. Tucker, D. J. Wilson, B. Winkler, and V. Milman, "Pressure response of an organic-inorganic perovskite: Methylammonium lead bromide," *Chem. Mater.*, vol. 19, no. 10, pp. 2401–2405, 2007.
- [149] L. Wang, K. Wang, and B. Zou, "Pressure-Induced Structural and Optical Properties of Organometal Halide Perovskite Based Formamidinium Lead Bromide," *J. Phys. Chem. Lett.*, vol. 7, pp. 2556–2562, 2016.
- [150] G. E. Eperon, S. D. Stranks, C. Menelaou, M. B. Johnston, L. M. Herz, and H. J. Snaith, "Formamidinium lead trihalide: a broadly tunable perovskite for efficient planar heterojunction solar cells," *Energy Environ. Sci.*, vol. 7, no. 3, pp. 982–988, 2014.
- [151] F. C. Hanusch, E. Wiesenmayer, E. Mankel, A. Binek, P. Angloher, C. Fraunhofer, N. Giesbrecht, J. M. Feckl, W. Jaegermann, D. Johrendt, T. Bien and P. Docampo, "Efficient planar heterojunction perovskite solar cells based on formamidinium lead bromide," *J. Phys. Chem. Lett.*, vol. 5, no. 16, pp. 2791–2795, 2014.
- [152] C. Motta, F. El-Mellouhi, and S. Sanvito, "Exploring the cation dynamics in lead-bromide hybrid perovskites," *Phys. Rev. B*, vol. 93, pp. 235412, 2016.
- [153] A. A. Zhumekenov, M. I. Saidaminov, M. A. Haque, E. Alarousu, S. P. Sarmah, B. Murali, I. Dursun, X.-H. Miao, A. L. Abdelhady, T. Wu, O. F. Mohammed, and O. M. Bakr, "Formamidinium Lead Halide Perovskite Crystals with Unprecedented Long Carrier Dynamics and Diffusion Length," *ACS Energy Lett.*, vol. 1, no. 1, pp. 32–37, 2016.
- [154] N. Sestu, M. Cadelano, V. Sarritzu, F. P. Chen, D. Marongiu, R. Piras, M. Mainas, F. Quochi, M. Saba, A. Mura, and G. Bongiovanni, "Absorption F-Sum Rule for the Exciton Binding Energy in Methylammonium Lead Halide Perovskites," *J. Phys. Chem. Lett.*, vol. 6, no. 22, pp. 4566–4572, 2015.
- [155] H. Kunugita, T. Hashimoto, Y. Kiyota, Y. Udagawa, Y. Takeoka, Y. Nakamura, J. Sano, T. Matsushita, T. Kondo, T. Miyasaka and K. Ema, "Excitonic Feature in Hybrid Perovskite $\text{CH}_3\text{NH}_3\text{PbBr}_3$ single crystals," *Chem. Lett.*, vol. 44, no. 6, pp. 852–854, 2015.
- [156] N. Arora, M. I. Dar, M. Abdi-Jalebi, F. Giordano, N. Pellet, G. Jacopin, R. H. Friend, S. M. Zakeeruddin and M. Grätzel, "Intrinsic and Extrinsic Stability of Formamidinium Lead Bromide Perovskite Solar Cells Yielding High Photovoltage," *Nano Lett.*, vol. 16, no. 11, pp. 7155–7162, 2016.
- [157] P. F. Ndione, Z. Li, and K. Zhu, "Effects of alloying on the optical properties of organic-inorganic lead halide perovskite thin films," *J. Mater. Chem. C*, vol. 4, no. 33, pp. 7775–7782, 2016.
- [158] N. Arora, M. I. Dar, M. Hezam, W. Tress, G. Jacopin, T. Moehl, P. Gao, A. S. Aldwayyan, B. Deveaud, M. Grätzel, and M. K. Nazeeruddin, "Photovoltaic and Amplified Spontaneous Emission Studies of High-Quality Formamidinium Lead Bromide Perovskite Films," *Adv. Funct. Mater.*, vol. 26, no. 17, pp. 2846–2854, 2016.

- [159] Z. M. Beiley and M. D. McGehee, "Modeling low cost hybrid tandem photovoltaics with the potential for efficiencies exceeding 20%," *Energy Environ. Sci.*, vol. 5, no. 11, pp. 9173–9179, 2012.
- [160] G. Xing, N. Mathews, S. S. Lim, N. Yantara, X. Liu, D. Sabba, M. Grätzel, S. Mhaisalkar, and T. C. Sum, "Low-temperature solution-processed wavelength-tunable perovskites for lasing," *Nat. Mater.*, vol. 13, no. 5, pp. 476–480, 2014.
- [161] M. Saba, M. Cadelano, D. Marongiu, F. Chen, V. Sarritzu, N. Sestu, C. Figus, M. Aresti, R. Piras, A. G. Lehmann, C. Cannas, A. Musinu, F. Quochi, A. Mura, and G. Bongiovanni, "Correlated electron-hole plasma in organometal perovskites," *Nat. Commun.*, vol. 5, pp. 5049, 2014.
- [162] Q. Zhang, S. T. Ha, X. Liu, T. C. Sum, and Q. Xiong, "Room-temperature near-infrared high-Q perovskite whispering-gallery planar nanolasers," *Nano Lett.*, vol. 14, no. 10, pp. 5995–6001, 2014.
- [163] B. R. Sutherland, S. Hoogland, M. M. Adachi, C. T. O. Wong, and E. H. Sargent, "Conformal organohalide perovskites enable lasing on spherical resonators," *ACS Nano*, vol. 8, no. 10, pp. 10947–10952, 2014.
- [164] F. Deschler, M. Price, S. Pathak, L. E. Klintberg, D.-D. Jarausch, R. Higler, S. Hüttner, T. Leijtens, S. D. Stranks, H. J. Snaith, M. Atatüre, R. T. Phillips, and R. H. Friend, "High photoluminescence efficiency and optically pumped lasing in solution-processed mixed halide perovskite semiconductors," *J. Phys. Chem. Lett.*, vol. 5, no. 8, pp. 1421–1426, 2014.
- [165] T. S. Kao, Y.-H. Chou, C.-H. Chou, F.-C. Chen, and T.-C. Lu, "Lasing behaviors upon phase transition in solution processed perovskite thin films," *Appl. Phys. Lett.*, vol. 105, no. 23, pp. 231108, 2014.
- [166] R. Dhanker, A. N. Brigeman, A. V. Larsen, R. J. Stewart, J. B. Asbury, and N. C. Giebink, "Random lasing in organo-lead halide perovskite microcrystal networks," *Appl. Phys. Lett.*, vol. 105, no.15, pp. 151112, 2014.
- [167] D. Priante, I. Dursun, M. S. Alias, D. Shi, V. A. Melnikov, T. K. Ng, O. F. Mohammed, O. M. Bakr, and B. S. Ooi, "The recombination mechanisms leading to amplified spontaneous emission at the true-green wavelength in $\text{CH}_3\text{NH}_3\text{PbBr}_3$ perovskites," *Appl. Phys. Lett.*, vol. 106, no. 8, pp. 081902, 2015.
- [168] K. Chen, A. J. Barker, F. L. C. Morgan, J. E. Halpert, and J. M. Hodgkiss, "Effect of carrier thermalization dynamics on light emission and amplification in organometal halide perovskites," *J. Phys. Chem. Lett.*, vol. 6, no. 1, pp. 153–158, 2015.
- [169] H. Zhu, Y. Fu, F. Meng, X. Wu, Z. Gong, Q. Ding, M. V. Gustafsson, M. T. Trinh, S. Jin, and X. Y. Zhu, "Lead halide perovskite nanowire lasers with low lasing thresholds and high quality factors," *Nat. Mater.*, vol. 14, no. 6, pp. 636–642, 2015.
- [170] S. D. Stranks, S. M. Wood, K. Wojciechowski, F. Deschler, M. Saliba, H. Khandelwal, J. B. Patel, S. J. Elston, L. M. Herz, M. B. Johnston, A. P. H. J. Schenning, M. G. Debije, M. K. Riede, S. M. Morris, and H. J. Snaith, "Enhanced Amplified Spontaneous Emission in Perovskites Using a Flexible Cholesteric Liquid Crystal Reflector," *Nano Lett.*, vol. 15, no. 8, pp. 4935–4941, 2015.
- [171] Q. Liao, K. Hu, H. Zhang, X. Wang, J. Yao, and H. Fu, "Perovskite microdisk microlasers self-assembled from solution," *Adv. Mater.*, vol. 27, no. 22, pp. 3405–3410, 2015.
- [172] J. Xing, X. F. Liu, Q. Zhang, S. T. Ha, Y. W. Yuan, C. Shen, T. C. Sum, and Q. Xiong, "Vapor Phase Synthesis of Organometal Halide Perovskite Nanowires for Tunable Room-Temperature Nanolasers," *Nano Lett.*, vol. 15, no. 7, pp. 4571–4577, 2015.
- [173] K. Galkowski, A. Mitioglu, A. Miyata, P. Plochocka, O. Portugall, G. E. Eperon, J. T.-W. Wang, T. Stergiopoulos, S. D. Stranks, H. Snaith, and R. J. Nicholas, "Determination of the exciton binding energy and effective masses for methylammonium and formamidinium lead tri-halide perovskite semiconductors," *Energy Environ. Sci.*, vol. 9, no. 3, pp. 962–970, 2016.
- [174] L. Protesescu, S. Yakunin, M. I. Bodnarchuk, F. Bertolotti, N. Masciocchi, A. Guagliardi and M. V. Kovalenko, "Monodisperse Formamidinium Lead Bromide Nanocrystals with Bright and Stable Green Photoluminescence,"

- J. Am. Chem. Soc.*, vol. 138, no. 43, pp. 14202–14205, 2016.
- [175] K. A. Bulashevich, A. V. Kulik, and S. Y. Karpov, “Optimal ways of colour mixing for high-quality white-light LED sources,” *Phys. status solidi*, vol. 212, no. 5, pp. 914–919, 2015.
- [176] M. Auf Der Maur, A. Pecchia, G. Penazzi, W. Rodrigues, and A. Di Carlo, “Efficiency Drop in Green InGaN/GaN Light Emitting Diodes: The Role of Random Alloy Fluctuations,” *Phys. Rev. Lett.*, vol. 116, no. 2, p. 27401, 2016.
- [177] Y. Fu, H. Zhu, A. W. Schrader, D. Liang, Q. Ding, P. Joshi, L. Hwang, X. Y. Zhu, and S. Jin, “Nanowire Lasers of Formamidinium Lead Halide Perovskites and Their Stabilized Alloys with Improved Stability,” *Nano Lett.*, vol. 16, no. 2, pp. 1000–1008, 2016.
- [178] M. F. Aygueler, M. D. Weber, B. M. D. Puscher, D. D. Medina, P. Docampo, and R. D. Costa, “Light-Emitting Electrochemical Cells Based on Hybrid Lead Halide Perovskite Nanoparticles,” *J. Phys. Chem. C*, vol. 119, no. 21, pp. 12047–12054, 2015.
- [179] A. Perumal, S. Shendre, M. Li, Y. K. E. Tay, V. K. Sharma, S. Chen, Z. Wei, Q. Liu, Y. Gao, P. J. S. Buenconsejo, S. T. Tan, C. L. Gan, Q. Xiong, T. C. Sum and H. V. Demir, “High brightness formamidinium lead bromide perovskite nanocrystal light emitting devices,” *Sci. Rep.*, vol. 6, pp. 36733, 2016.
- [180] L. Meng, E.-P. Yao, Z. Hong, H. Chen, P. Sun, Z. Yang, G. Li, and Y. Yang, “Pure Formamidinium-Based Perovskite Light-Emitting Diodes with High Efficiency and Low Driving Voltage,” *Adv. Mater.*, vol. 29, no. 4, pp. 1603826, 2017.

Chapter 2

Experimental Setups

This chapter describes the main experimental setups used in this work. The picosecond time-resolved photoluminescence (TRPL) system, which is used for the time-resolved optical studies on perovskites at relatively low carrier densities, is first described in detail. Second, the time-integrated PL setup with picosecond high energy pulses, used for the ASE measurements, is described. The third section discusses the SEM-based cathodoluminescence setup, which is used for the spatial CL mapping of perovskite microcrystals.

2.1 Picosecond Time-resolved Photoluminescence Setup

Dynamics of excited carriers in semiconductors can take place at different time scales, from picoseconds to nanoseconds and even microseconds. Probing the excited state in semiconductors thus needs ultrafast excitation tools as well as detection systems capable of recording signals, within the appropriate time scale, related to the excited state. Time-resolved photoluminescence (TRPL) is a widely used probe in this regard, and a variety of excitation sources and PL detection equipments have been invented/used for this purpose. In our system, a picosecond pulsed laser is used for excitation, and the detection is carried out using a streak camera and a CCD detector. Below is the description of the excitation line, detection line and cooling system of the TRPL system used in this work, which is schematically depicted in Figure 2.1.

2.1.1 Excitation Line

The optical excitation line consists mainly of a Ti:Sapph resonator that is optically pumped by a frequency doubled Nd:YVO₄ CW laser, ultimately producing picosecond pulses of ~ 2 ps duration, with a tunable wavelength range between ~ 690 - 1080 nm, best optimized at ~ 850 nm. The pulses are further frequency doubled/tripled using a second harmonic/third harmonic generation unit in the optical path,

which allows picosecond pulses at ~ 425 nm and 280 nm to be obtained. Below is a detailed description of the excitation line.

- 1) CW Pump Laser (Millennia Xs, Spectra Physics [1]): The gain medium in this high-power CW laser is a Nd:YVO₄ crystal that is pumped by two high power laser diode bars (each bar consists of 20 laser diodes) of ~ 820 nm emission wavelength, which perfectly overlaps with one of the sharp absorption lines of Nd³⁺. The Nd³⁺ ions in the Yttrium Vanadate (YVO₄) crystal makes an efficient four-level lasing system, where the transition between 4F_{3/2} – 4I_{11/2} produces the most probable emission at 1064 nm. The Nd:YVO₄ crystal is continuously cooled by a convenient chiller. The 1064 nm line is subsequently doubled using a phase-matched Lithium Triborate (LBO) doubling crystal, which is housed in a regulated oven to maintain the optimal working temperature, producing 532 nm laser emission. The doubling LBO crystal has a large acceptance angle and thus insensitive to small misalignments of the crystal. Before the exit, an output coupling system ensures complete reflectance of the 1064 nm light, efficient output coupling of the 532 nm light, and efficient stabilization of the output power (though a beam splitter/photodiode feedback loop regulating the power of the two pump diode bars). An output power of 10 W can be achieved.
- 2) Picosecond Ti:Sapph Resonator (Tsunami 3950C, Spectra Physics [2]): The gain medium here is a Ti:Al₂O₃ rod crystal, cooled by an appropriate chiller, which has the wide absorption band of Ti³⁺ ions between ~ 400 -650 nm. The Ti³⁺ ions in the Sapphire (Al₂O₃) crystal also have a wide emission band between ~ 600 -1100 nm. The overlap between the Ti³⁺ absorption/emission bands limits the minimum wavelength possible for lasing action to 670 nm. Other factors such as mirror coatings, atmospheric absorption (e.g. oxygen, water vapor), pump power etc... can all result in further reduction of the wavelength tuning range. In fact, Tsunami pulsed laser systems come with different options for the mirror set in the cavity (6 mirrors) such that a narrower wavelength range is optimized for a stable and high performance. In our system, the 850 nm Mid (M) mirror set is implemented, which gives an optimized output between 780-900 nm.

The Ti:Sapph rod is located in a folded cavity of six mirrors, with a total cavity length of $L = 1.83$ m. Mode-locking technique is used to generate the picosecond pulses. Briefly, a modulation loss is created in the laser cavity using an acousto-optic modulator (AOM) that is located at one end of the cavity. The AOM frequency, run by a radio frequency (RF) generator, must precisely match the laser repetition rate of 82 MHz ($c/2L$, where c is the speed of light in air) in order to phase-lock all random longitudinal modes in the cavity within the gain bandwidth allowed by the Ti³⁺ emission band, mirror setting and other cavity losses as mentioned above. Pulses of ~ 2 ps duration are thus generated in the laser cavity, with one pulse created every 12.2 ns ($2L/c$). The positive group velocity dispersion (GVD), which develops as pulses travel in the cavity, is compensated in our system by a Gires-Tournois interferometer (GTI) that introduces negative GVD into the chirped pulses.

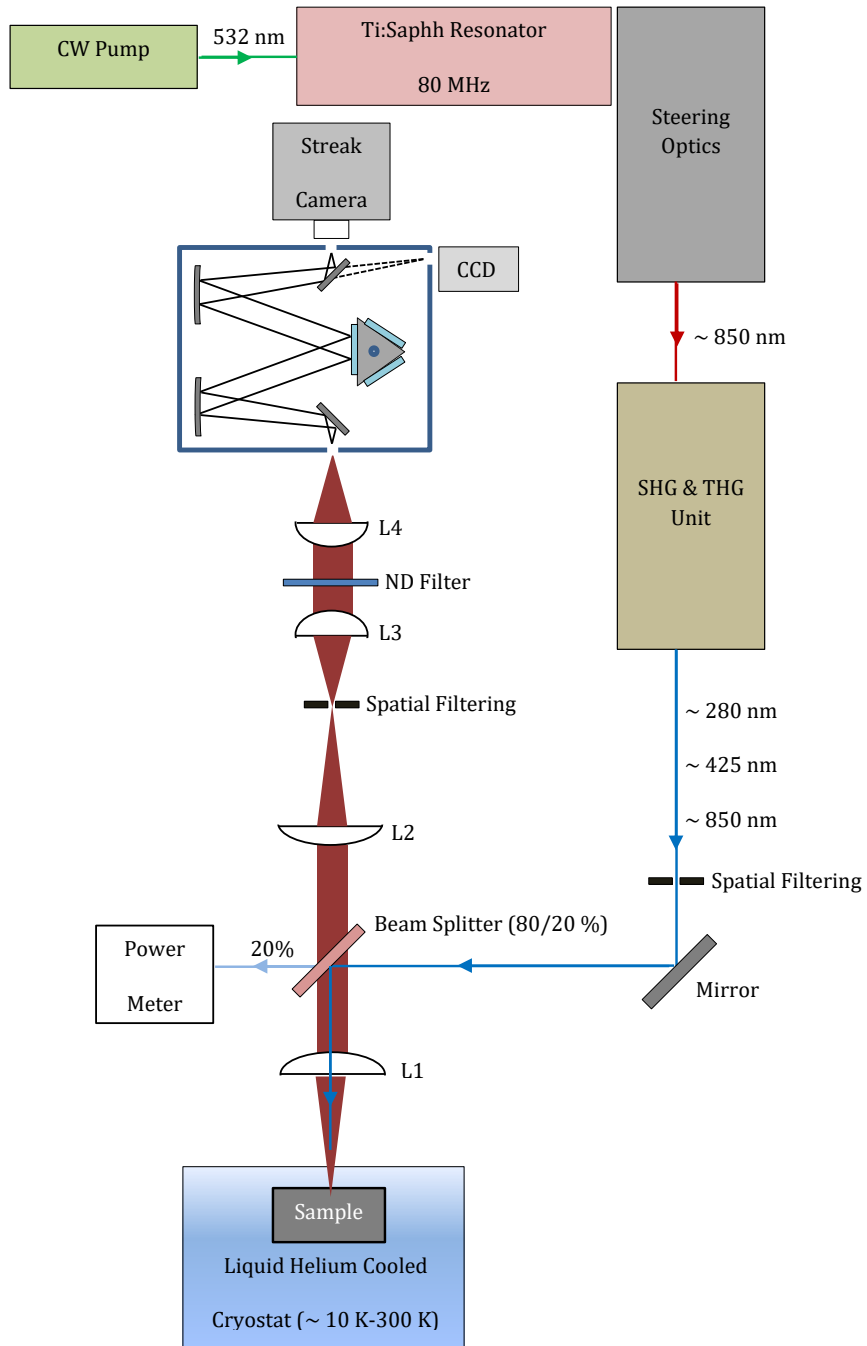


Figure 2.1 A schematic diagram for the Time Resolved Photo Luminescence (TRPL) setup.

- 3) SHG & THG Unit (GWU-Spectra Physics, Model 3980 [3]): This is a Beta Barium Borate (β -BaB₂O₄ or BBO) crystal-based unit for the generation of higher harmonics from the incoming laser pulses. The second harmonic of the 850 nm pulse is generated by the direct travel of the laser pulse through a properly phase-matched BBO crystal. For the third harmonic generation (THG), the fundamental pulse at 850 nm is spatially and temporally overlapped with the SHG pulse of 425 nm in another phase-matched BBO crystal to generate THG pulses of 280 nm wavelength.

The excitation pulse, with chosen wavelength, is subsequently spatially filtered, to ensure a Gaussian-like beam shape, and then reflected towards the sample using a beam splitter with 80%-20% splitting. The 80% line is focused on the sample using an achromatic lens (L1 in Figure 2.1) with a focal length F of 90 mm. For a given excitation wavelength, the diameter of the excitation spot on the sample, Φ , is approximately given by $\Phi = F\left(\frac{2.4\lambda}{\phi}\right)$, where ϕ is the initial beam diameter [4]. For 425 nm pulses, and for an initial beam diameter of ~ 1 -2 mm, the excitation spot diameter can be estimated to be ~ 50 -100 μ m. The 20% portion, after the beam splitter, travels towards a power meter (gentec, model: PH100-SiUV) for energy/power measurements of the pulse.

2.1.2 Detection Line

The PL emission, originating from the excitation spot on the sample, is collected by an appropriate lens system, then focused and dispersed by a spectrometer, whose two output ports are equipped with a streak camera and a CCD chip for PL detection. The details are as follows:

- 1) Focusing & Spatial Filtering Path: The PL emission from the sample is first collected by the same L1 lens used to focus the incoming excitation laser beam, and then re-focused again by the L2 lens, which has the same focal length as L1. At the focal point of the two-lens system, a pinhole is introduced for spatial filtering of the PL emission spot. The PL emission spot is basically a 1:1 image of the PL emission spot first created by the exciting laser beam on the sample. Therefore, it essentially reflects the laser excitation spot as well. Hence, spatial filtering ensures that the detection system will receive PL emission only from the uniformly excited area located at the center of the excitation spot. Although this step is important for accurate analysis of PL dynamics, circumstances such as the fast UV-induced damage of the samples (see Chapter 4) necessitated to eliminate this step in order to gain a higher PL signal. However, the UV-induced damage study involved mainly a comparison between different samples, which rendered this step of minor significance in that case.

The spatially filtered beam is then re-focused by the L3-L4 lenses at the entrance of the spectrometer. A density filter can be introduced, when required, between the two lenses.

- 2) Dispersion Unit (iHR 320 Imaging Spectrometer, Horiba Jobin Yvon): This is a modular Czerny-Turner spectrometer, with a focal length of 320 mm, two entrance ports and two exit ports. Three gratings can be simultaneously mounted on a motorized turret with three facets. Gratings of 300 grooves/mm and

600 grooves/mm, both blazed at 300 nm, were used in this work. The two exit ports of the spectrometer are coupled with a CCD detector and a Streak Camera.

- 3) Detection Units: The spectrally dispersed light is collected either by the CCD camera (Synapse, Horiba Jobin Yvon) or the streak camera (Hamamatsu C5680-27) respectively for time-integrated and time-resolved photoluminescence measurements.
 - a. Time-integrated PL (TIPL) measurements: TIPL measurements are first taken for the incoming emission light using the CCD camera. The CCD camera and the iHR 320 spectrometer are computer-connected to a control software (LabSpec), with which the entrance/exit slit widths can be changed, the emission spot (at zero order) on the CCD can be visualized, and the spectrum wavelength axis can be calibrated (with a reference lamp, for example). In addition to their own scientific significance, TIPL measurements are also important for the spectral calibration of the streak image in the TRPL measurements as will be discussed below.

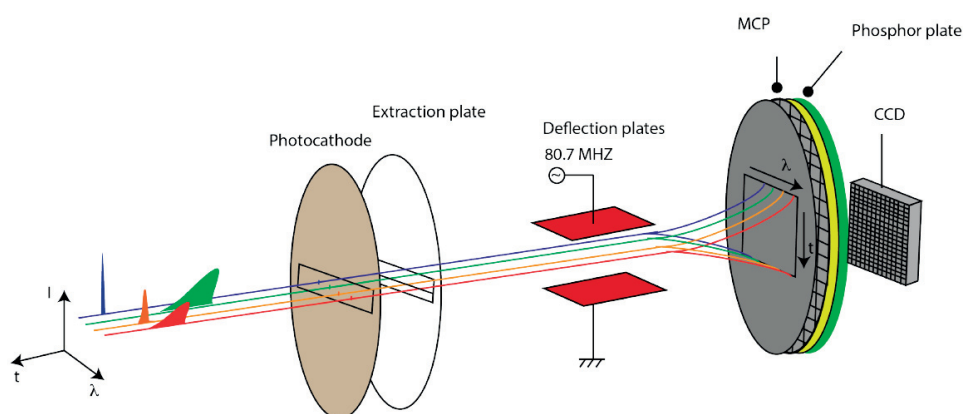


Figure 2.2 A schematic diagram showing the working principle of the streak camera [5]

- b. TRPL measurements: The streak camera is used for the TRPL measurements. The working principle of the streak camera is shown in Figure 2.2. Briefly, the PL emission spatially resolved along the lateral direction is first vertically thinned using a thin slit at the entrance of the streak camera. The resulting rectangular-shaped emission slab is directed towards a photocathode, where photoelectrons are laterally generated as well. The generated photoelectrons pass through a sinusoidal RF generated electric field, with a frequency synchronized with that of the mode-locked laser, and are accordingly deflected. Electrons arriving at different time delays will be differently deflected by the sinusoidal electric field, a process that transforms the temporal information in the received emission pulse into spatial deflection. Deflected electrons, now having their spectral information on the lateral dimension and their temporal information along the vertical direction, are sent on a microchannel plate (MCP), through which they are multiplied and driven to a phosphor screen. Hence, the light intensity map of the phosphor screen reflects the

spectral/temporal dispersion of the emission spot, and is collected after that with another CCD camera (Hamamatsu C4742-95) at the back end of the streak camera tube.

In order to analyze the resulting streak image, the image is first calibrated for the lateral wavelength axis using the spectral TIPL emission measured using the calibrated CCD camera, discussed in part (a) above. Also, the background photocathode emission, which is recorded by taking a streak image with the excitation laser off, has to be subtracted. A programming code was developed, using Mathematica software, to perform the above calibration/correction steps, and to subsequently extract the required spectral/temporal sections of the streak image.

The Hamamatsu C5680-27 streak camera allows a time resolution of 2 ps. However, small timing jitters in the laser repetition rate as well as other laser instabilities cannot be avoided, which lowers the time resolution of the overall optical system to ~ 5 -10 ps.

2.1.3 Vacuum and Cooling Systems

The sample is placed inside an air-evacuated cryostat (Cryophysics) that is cooled by liquid Helium. The liquid Helium is generated by a closed-loop water-cooled Helium compressor (CTI-Cryogenics 8200). The vacuum in the cryostat (base pressure $\sim 10^{-5}$ mbar) is achieved using a rotary pump (PASCAL vacuum pump, Alcatel) and a turbo molecular pump (ACT 200 T, Alcatel). The temperature in the cryostat is controlled by using a proportional-integral-derivative (PID) controller (LakeShore, model 335).

2.2 High Power Picosecond Pulsed Time Integrated PL Setup

PL measurements under high carrier densities were carried out using this setup, which produces ~ 70 picosecond pulses, with a tunable pulse energy ranging between few μJ to > 2 mJ for a wide range of excitation wavelengths (420-2300 nm). Figure 2.3 depicts a schematic for the optical setup. Below is a detailed description of the system.

2.2.1 Excitation Line

The excitation line mainly consists of an Nd:YAG Q-switched laser producing high power 70 ps pulses of 1064 nm and 532 nm wavelengths, followed by a passive optical parametric generator (OPG) unit.

- a) Nd:YAG High Power Pulsed Laser (LOTIS TII, model LS-2151 [6]): This system contains a Q-switched Nd:YAG resonator cavity. The $4F_{3/2} - 4I_{11/2}$ transition (1064 nm) of the triply charged Neodymium ions Nd^{3+} in the Yttrium Aluminum Garnet crystal ($\text{Y}_3\text{Al}_5\text{O}_{12}$ or YAG) makes the most efficient lasing transition. The Nd:YAG crystal is excited by a water-cooled pulsed flash lamp, with pulse duration of

$\sim 120\text{-}150\ \mu\text{s}$. The Q-switching control mechanism is provided by a mode-locking AOM, driven at 100 MHz, and two Pockels cells in the resonator cavity. The laser head also contains a phase-matched Potassium di-Deuterium Phosphate (KD_2PO_4 , KD^*P or DKDP) crystal, placed in a temperature-controlled oven, for second harmonic generation. The system has three output coupling exits, one for the pure fundamental frequency (FF) with 1064 nm wavelength, one for the pure second harmonic (SH) of 532 nm, and one for a mixed FF+SH output, which seeds the OPG-OPA unit as will be discussed below. The resulting laser beams have pulse durations of $\sim 70\text{-}80\ \text{ps}$, with a repetition rate of 15 Hz.

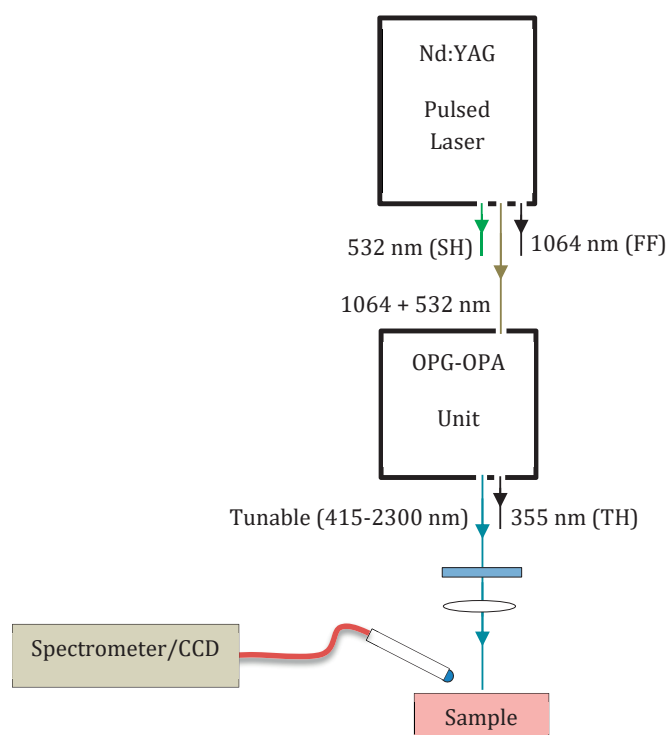


Figure 2.3 A schematic diagram showing the high power picosecond pulsed time-integrated PL setup

- b) OPG-OPA Unit (LOTIS TII, model LT-2215 OPG-PC [7]): This unit is fed by the 1064+532 nm mixed output line from the Nd:YAG Q-switched laser. The beam passes through a Potassium di-Hydrogen Phosphate (KH_2PO_4 or KDP) crystal phase-matched for the generation of third harmonic (TH) at 355 nm. The TH beam is then cleaned by appropriate optics before it can be either directly used for excitation, through a special output coupling, or sent for optical parametric generation (OPG). OPG is a spontaneous parametric down-conversion process, where the TH pump beam is split into signal and idler beams of lower photon energies. The process takes place in a BBO crystal, and wavelength tuning of the signal/idler beams is achieved by computer motorized rotation of the BBO crystal. Optical parametric amplification (OPA) is additionally performed by overlapping the signal/idler beams with the TH pump beam in another BBO crystal. The wavelength of the output amplified beam is then

selected using a variety of output coupling optics. The pulse duration is slightly compressed after the OPG-OPA unit to ~ 50 -70 ps.

2.2.2 Optical Path and PL Detection

The excitation beam from the OPG-OPA unit has a beam diameter of ~ 1 cm. The beam is then focused on the sample surface, using a convex objective lens, to ~ 2 mm. A neutral density filter is placed in the optical path to adjust the excitation power.

The sample is placed on a 6-degree-of-freedom adjustable stage. The PL emission from the sample is detected using a fiber optic-coupled compact "spectrometer/CCD camera" unit (Ocean Optics QE65 Pro).

The resulting PL emission is analyzed according to the discussion presented in Chapter 3. A Python-based programming code, lately developed by Mr. Abdulaziz Alqasem, which allows a rapid Gaussian peak fitting of the dual PL emission peaks from multiple data files, was used for analyzing part of the PL data files.

2.3 Cathodoluminescence Setup

In cathode-luminescence (CL), the sample is excited by electrons instead of photons in the case of PL measurements, and the luminescence spectrum is subsequently collected. Typically, a highly energetic and highly focused electron beam (beam diameter ~ 1 -10 nm) inside the chamber of an electron microscope is used for excitation, which provides a nanometer scale spatial localization to the excitation process. This property is a major advantage of CL spectroscopy allowing, for example, the spatial probing of different locations in a single micro/nanostructure. In a scanning electron microscope (SEM) chamber, thanks to the scanning capability of the e-beam, a map of the CL optical activity of the micro/nanostructure can be obtained.

CL analysis is, however, less straightforward than PL and different factors possibly affecting the CL spectrum during measurements have to be carefully accounted for. For example, the spectral information in the CL spectrum can be altered by many external factors, e.g. e-beam induced damage and vacuum-enhanced radiative emission of some specific defects (e.g. surface defects, oxygen vacancies), which have to be considered in the measurements and analysis of results. The CL intensity is another subtle CL attribute, and careful analysis of CL intensity can unravel deep knowledge about the optical properties of micro/nanostructures. The section below gives a brief account on some necessary issues to be considered in the analysis of CL intensity maps.

2.3.1 Interaction of Electron Beam with Matter

When a highly energetic electron beam (typically few keV) in an SEM chamber impinges a luminescent sample, e.g. direct bandgap semiconductor, a large portion of incident electrons are elastically backscattered with energies comparable to original ones, for which they are called backscattered electrons. Other electrons undergo subsequent inelastic collisions inside the semiconductor. The inelastic scattering events result in the gradual energy loss for incident electrons through X-ray emission, CL, heating (excitation of phonons)...etc. The volume in the sample, in which these processes take place, is called the interaction volume. After successive energy loss events, some electrons can escape the surface with very low energies (~ 200 eV); these electrons are called secondary electrons (SE). The SE signal, measured using an Everhardt Thornley detector, is traditionally used, with e-beam scanning, to create the morphological image of the sample surface.

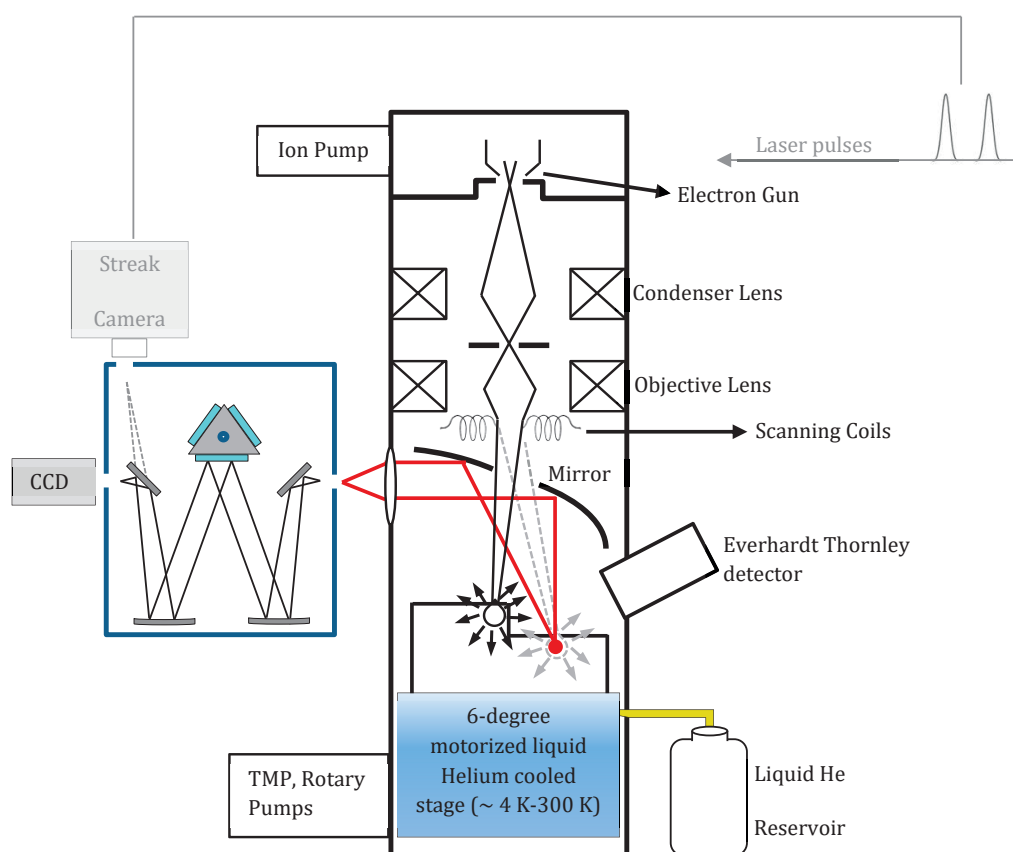


Figure 2.4 A schematic diagram for the SEM-CL system

CL emission takes place when an electron in the VB of a semiconductor is excited to the CB by an incident electron. To distinguish between the two electrons involved in the process, we designate the excited electron in the CB as “carrier”. In this new terminology, then, incident electrons create carriers, whose recombination produces the CL emission. Assuming that carriers recombine where they are created,

i.e. assuming no carrier diffusion, the CL emission essentially originates from the interaction volume, and the CL intensity profile will thus reflect the attributes of the interaction volume. Carrier diffusion is, however, necessary to be considered in the CL analysis, especially for materials with high carrier mobilities. Although the excitation point is highly localized in CL measurements, carrier diffusion will result in a wider recombination volume, from which delocalized accumulated emission will contribute to the received CL signal.

Figure 2.4 shows a schematic for the SEM-CL system used in our work. The optical path of the CL emission is depicted using red lines, and the SEs are shown as arrows originating for two different excitation points. It can be noticed that when the beam excitation point is close to an edge, more SEs, with higher energies as well, will be generated. This edge enhanced SE emission is called the “edge effect”, and it results in reduced CL emission from the edge. For a specific material, the interaction volume increases with the e-beam energy (in keV or kV). Therefore, the sample’s surface is better probed with e-beams having lower kV, which facilitates CL depth-profiling studies to be performed.

2.3.2 Description of the Cathodoluminescence setup (Allalin 4027 Chronos, Attolight)

The SEM-CL system used in this study encloses a field-emission electron gun, which allows e-beam acceleration voltages between 1-10 kV. Instead of the traditionally used parabolic mirror, the CL emission is collected using an achromatic reflective objective with a large numerical aperture (NA = 0.71). The CL emission is then focused into an iHR 320 spectrometer and Synapse CCD camera (see Sec. 2.1.2 for description). The sample stage is coupled with a nano-metric piezoelectric positioning system with 6 degrees of freedom, and is cryo-cooled by using a Helium cold finger connected to a liquid Helium dewar. The coupling between the motorized stage and the cryostat is specially designed for reduced stage vibration and drift especially at low temperatures, and a slow drift of ~ 100 nm/hour was obtained. Although not carried out in this thesis, it is worth to mention that the SEM-CL system is also capable of performing time-resolved CL measurements, where picosecond electron pulses are generated from the optical excitation of the electron gun with laser pulses, and the resulting CL pulses are then temporally and spectrally dispersed on a streak camera CCD.

The CL emission is collected and dispersed using a 150 grooves/mm grating blazed at 500 nm, which allowed the coverage of both PbI_2 and perovskite emission ranges, as discussed in Chapter 5. The generated CL maps were analyzed using a dedicated MATLAB-based software developed by Dr. Gwenole Jacopin. The software allows the generation of panchromatic/monochromatic/polychromatic CL maps as well as line/area specified sectioning of desired regions. CASINO v2.42 [8] software was used for the Monte Carlo simulation studies of electron trajectories and CL emission.

References

- [1] Spectra-Physics, *Millenia Xs, diode-pumped, cw Visible Laser*, User's Manual.
- [2] Spectra-Physics, *Tsunami, Mode-locked Ti:sapphire Laser*, User's Manual.
- [3] Spectra Physics, *Model 3980 Frequency Doubler and Pulse Selector*, User's Manual.
- [4] P. M. Corfdir, *Physics of the Ultrafast Dynamics of Excitons in GaN Nanostructures*. PhD Thesis No. 5094, École Polytechnique Fédérale de Lausanne (EPFL), 2011.
- [5] M. Shahmohammadi, *Ultrafast spectroscopy of wide bandgap semiconductor nanostructures*. PhD Thesis No. 6713, École Polytechnique Fédérale de Lausanne (EPFL), 2015.
- [6] LOTISS TII, *Nd:YAG Actively Model-locked Laser System LS-2151*, User's Manual.
- [7] LOTISS TII, *LT-2215 OPG-PC Beta-Barium Borate Picosecond Optical Parametric Generator*, User's Manual.
- [8] D. Drouin, A. R. Couture, D. Joly, X. Tastet, V. Aimez, and R. Gauvin, "CASINO V2.42 — A Fast and Easy-to-use Modeling Tool for Scanning Electron Microscopy and Microanalysis Users", *Scanning*, vol. 29, no. 3, pp. 92-101, 2007.

Chapter 3

Photovoltaic and Amplified Spontaneous Emission Studies on FAPbBr₃ Thin Films

This chapter presents a detailed investigation on the photovoltaic and amplified spontaneous emission properties of FAPbBr₃ thin films deposited using different solvent environments. First, a theoretical framework that correlates and describes the experimental techniques necessary to present the findings is constructed. Through this construction, the photovoltaic properties in the ideal radiative limit, and under less idealized conditions as well, are calculated for FAPbBr₃-based solar cell devices using the absorption/emission detailed balance principle. The results are compared with the experimental results for FAPbBr₃-based solar cell devices, provided by the group of Prof. Nazeeruddin, EPFL, and the findings are correlated with time-resolved photoluminescence (TRPL) measurements performed on the same samples. Importantly, a record open circuit voltage (V_{OC}) was obtained for FAPbBr₃ films deposited using a 1:1 volume ratio of DMF/DMSO solvents. We find that this high V_{OC} is correlated with a roughly 30 times increase in the carrier lifetime compared to films deposited using DMF solvent only, which exhibited a noticeably lower V_{OC} of 1.14 V. The possible origins of V_{OC} losses are accordingly discussed.

Amplified spontaneous emission (ASE) could also be demonstrated for the same samples, with a threshold carrier density as low as $2 \times 10^{18} \text{ cm}^{-3}$. A detailed investigation on the effects of solvent used in the layer preparation, the HTM layer, and excitation wavelengths is presented. Attractively, carrier thermalization was manifested by only a slight drop in the quantum efficiency. Band gap renormalization (BGR) was observed as a systematic red-shift in the ASE peak with excitation density, and we show that the gain behavior at high carrier densities allows to estimate the BGR directly from the power-dependent ASE spectra. A BGR constant of $5\text{-}7 \times 10^{-9} \text{ eV}\cdot\text{cm}$ was accordingly obtained.

The main body of the work detailed in this chapter resulted in the following two publications:

1. Arora, N., Dar, M. I., Hezam, M., Tress, W., Jacopin, G., Moehl, T., Gao, P., Aldwayyan, A. S., Deveaud B., Gratzel, M. & Nazeeruddin, M. K. (2016). Photovoltaic and Amplified Spontaneous Emission Studies

of High-Quality Formamidinium Lead Bromide Perovskite Films. *Advanced Functional Materials*, 26(17), 2846-2854.

2. Hezam, M., Alqasem, A., Qaid, S., Jacopin, G., Khan, M. N., Arora, N., Dar, M. I., Deveaud, B., Nazeeruddin, M. K., Aldwayyan, A. Investigation of Threshold Carrier Density of Amplified Spontaneous Emission from Optically Pumped Formamidinium Lead Bromide Perovskite Film (submitted).

3.1 Theoretical Background

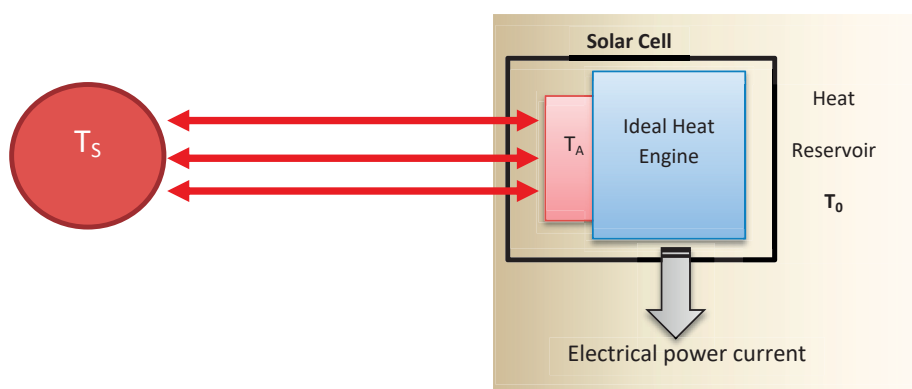


Figure 3.1 A schematic diagram showing the thermodynamic working principle of a solar cell

The main task of a solar cell is to convert the solar energy into a useful electrical current. A general light absorbing material, not necessarily a semiconductor, in the solar cell will be heated upon absorption of solar energy, and a mechanism has to be invented to convert this absorbed thermal energy into electrical work (see Figure 3.1). Therefore, a solar cell can be treated as a heat engine transforming the thermal radiation from the sun, which can be approximated by a black body of temperature $T_S = 5800$ K, into electrical work. Optimally, the absorber can fully absorb the incident solar energy; i.e., when the absorber is a black body as well. According to Kirchhoff's law of thermal radiation, both black bodies (the sun and the absorber) will emit and absorb radiation. The emissive power of the absorber will increase, according to Stefan-Boltzmann law, with the fourth power of its temperature T_A . Therefore, in order to maximize the amount of work to be extracted, the absorber temperature has to be substantially lower than the temperature of the sun so that absorber's emission is minimized. Therefore, the absorption efficiency η_{abs} can be estimated as (assuming similar solid angles of absorber's emission and absorption):

$$\eta_{abs} = 1 - \frac{T_A^4}{T_S^4}$$

However, at the same time, the temperature difference between the absorber and its surroundings (considered as a heat reservoir having a constant temperature T_0 in Figure 3.1), will determine the net

work flux out of the heat engine. Increasing this temperature difference, $T_A - T_0$, increases the efficiency of the heat engine, which can be achieved only by increasing T_A . The maximum theoretical efficiency of the heat engine, called Carnot efficiency η_{Carnot} , is then given by:

$$\eta_{Carnot} = 1 - \frac{T_0}{T_A}$$

Both competing processes, i.e. absorber's emissive power (loss) and higher Carnot efficiency (gain), become more efficient when the absorber's temperature T_A increases. The maximum theoretically possible efficiency of a solar cell is then given by $\eta_{max} = \eta_{abs} \times \eta_{Carnot}$, which maximizes at 85% for $T_A = 2478$ K!

For a body to be black, a continuous spectrum of energy levels needs to be available for the excitation solar spectrum. This situation takes place, approximately, in metals where a continuum of higher energy states is available for electrons to be excited by the solar photons. However, in metals, excited electrons lose the absorbed solar energy by successive generation of phonons in a very short time (\sim ps), resulting in only poor utilization of solar energy.

The bandgap in semiconductors makes a fundamental difference in this regard. Within the conduction band, electrons excited to states higher than the conduction band edge will also thermalize (like in metals) to their quasi-Fermi levels (and the same for holes); however, returning to the valence band after this thermalization step requires, for an ideal semiconductor, the loss of the bandgap energy in one step, which is a much slower process. The long-lived electrons in the conduction band (and also for holes in the valence band) and the various possible e-h separation mechanisms, within the lifetime of generated e-h pairs, provided by different solar cell technologies make it possible to perform solar energy/electrical current conversion using semiconductor absorbers.

In a semiconductor absorber, as astonishingly shown by Wurfel [1], photoexcited charge carriers can reach the sun temperature T_s , before they rapidly thermalize with the lattice, the reservoir in this case. The net energy that can be carried by charge carriers as an electrical current has been shown by Wurfel [1], after a rigorous derivation, to be given by:

$$\text{Net useful energy} = E_F^n - E_F^p = E_g - k_B T_0 \ln \frac{N_c N_v}{np} \quad (3.1)$$

where E_F^n , E_F^p are respectively the quasi-Fermi level energies of electrons and holes, E_g is the band gap, k_B is Boltzmann constant, N_c and N_v are the effective density of states, n and p are the electron and hole densities. In the darkness, $E_F^n = E_F^p$ and Eq. 3.1 reads:

$$np = n_0 p_0 = n_i^2 = N_c N_v \exp\left(-\frac{E_g}{k_B T_0}\right) \quad (3.2)$$

n_i is the intrinsic carrier density (defined by Eq. 3.2), and n_0 and p_0 are the equilibrium electron and hole densities respectively.

3.1.1 Open-Circuit Measurements

Light Intensity-Dependent Open Circuit Voltage (V_{OC})

Now, let's consider the situation when the semiconductor is illuminated, but charge carriers are not extracted, i.e. under open-circuit condition. In this situation, the rate of e-h generation G will equilibrate with their recombination rate R (i.e. $R = G$). Assuming that only radiative bimolecular recombination is in action (i.e. band-to-band e-h recombination with no trap-assisted or Auger non-radiative recombination), the recombination rate then simply reads:

$$R = \beta np$$

where β is the bimolecular recombination coefficient. Since the light illumination intensity is directly proportional to the e-h generation rate G , which is in equilibrium with R , then the quasi-Fermi level splitting will ideally appear as a photovoltage V_{OC} across the semiconductor terminals, and Eq. 3.1 can be written as:

$$eV_{OC} = E_g - k_B T_0 \ln \frac{N_c N_v \beta}{G} \quad (3.3)$$

Eq. 3.3 describes V_{OC} as a function of bandgap, temperature and light intensity (G). It can be noticed that the other parameters N_c , N_v , and β are intrinsic to the semiconductor material used for the photovoltaic device. N_c and N_v are given by:

$$N_c = 2 \left(\frac{2\pi m_n^* k_B T}{h^2} \right)^{\frac{3}{2}}; \quad N_v = 2 \left(\frac{2\pi m_p^* k_B T}{h^2} \right)^{\frac{3}{2}}$$

where m_n^* , m_p^* are the electron (hole) effective masses, and h is the Planck's constant. A closer look at Eq. 3.3 implies that V_{OC} should scale linearly with the logarithm of illumination intensity, i.e. $V_{OC} \propto \ln(G)$, with a slope of $k_B T/e$. This property is useful, as will be further elaborated below, to determine the dominant e-h recombination mechanism in perovskite solar cells.

In the dark, i.e. when the only illumination is the background thermal radiation, the temperature of the ambient, which is also T_0 , will result in a background black body emission flux density Φ_{BB} , given by:

$$\Phi_{BB} dE = \frac{2\pi}{c^2 h^3} \frac{E^2 dE}{\exp\left(\frac{E}{k_B T_0}\right) - 1}$$

The semiconductor absorber will absorb/emit the part of the background radiation Φ_{BB} that lies above the bandgap. The generation rate in the dark G_0 can then be calculated by integrating the emission photon flux (above the bandgap) multiplied by the absorption coefficient of the absorber:

$$G_0 = \Phi_{\text{emission},0} = \int_{E_g}^{\infty} \alpha(E) \Phi_{BB} dE = \beta n_0 p_0 = \beta n_i^2 \quad (3.4)$$

Eq. 3.4 is nothing but the well-known van Roosbroeck-Shockley relation [2], which elucidates the reversibility of emission/absorption processes in a semiconductor.

The maximum V_{OC} that can be achieved under standard solar illumination (AM1.5G) can be estimated by assuming: a full absorbance of the solar spectrum above the bandgap, a one-to-one photon-to-eh pair generation, and the thermalization of excited photocarriers to their respective quasi-Fermi levels. Therefore, in the ideal limit, losses that will impede the development of V_{OC} are the thermalization of excited carrier and their subsequent bimolecular recombination only, which will result in the following absorber's emission:

$$\Phi_{\text{emission}} = \Phi_{\text{emission},0} \exp\left(\frac{eV_{OC}}{k_B T}\right) \quad (3.5)$$

where the exponential factor accounts for the enhanced emission from the absorber due to the separation in quasi-Fermi levels of electrons and holes ($E_F^n - E_F^p = eV_{OC}$). Under equilibrium, $R = G$ which results in the following relation:

$$\text{Number of solar photons above } E_g(\Phi_{\text{incident}}) = \Phi_{\text{emission},0} \exp\left(\frac{eV_{OC}}{k_B T}\right) \quad (3.6)$$

Therefore, the maximum V_{OC} that can be obtained under incident illumination density Φ_{incident} and assuming only radiative recombination, is given by:

$$V_{OC} = \frac{k_B T}{e} \ln\left(\frac{\Phi_{\text{incident}}}{\Phi_{\text{emission},0}}\right) \quad (3.7)$$

The slope of $k_B T/e$ in the V_{OC} versus $\ln(G)$ relation can similarly be noticed in Eq. 3.7. Under standard AM1.5G solar illumination, the theoretical radiative limit for V_{OC} can be estimated by replacing Φ_{incident} with the AM1.5G illumination density, and Eq. 3.7 reads:

$$V_{OC}^{rad} = \frac{k_B T}{e} \ln\left(\frac{\Phi_{AM1.5G}}{\Phi_{\text{emission},0}}\right) \quad (3.8)$$

Figure 3.2 shows $\Phi_{AM1.5G}$ as a function of bandgap, estimated using the available AM1.5G solar spectrum data with $\sim 100 \text{ mW/cm}^2$ intensity from the National Renewable Energy Laboratory (NREL) [3] and $\Phi_{\text{emission},0}$ of a black body radiation of temperature 300 K, along with V_{OC}^{rad} estimated using Eq. 3.8 as a function of semiconductor bandgap. For FAPbBr₃, with a bandgap of $\sim 2.3 \text{ eV}$, $V_{OC}^{rad} = 1.98 \text{ eV}$.

Indeed, an ideal semiconductor with no traps does not exist. In fact, recombination through trap defects is commonly dominant in semiconductors. As discussed in Chapter 1, the solution-processing of perovskites makes them even more subjected to the development of large densities of traps. The trap-assisted recombination can be described by the Shockley-Read-Hall (SRH) theory; for a single dominant trap type, the SRH trap-assisted recombination is given by [4]:

$$R_{SRH} = \frac{np - n_i^2}{\frac{n + N_C \exp\left(-\frac{E_C - E_T}{k_B T}\right)}{N_T \sigma_p v_p} + \frac{p + N_V \exp\left(-\frac{E_T - E_V}{k_B T}\right)}{N_T \sigma_n v_n}} \quad (3.9)$$

Here, E_T is the trap energy level in the bandgap between the conduction band edge E_C and the valence band edge E_V . N_T is the total trap concentration, and $\sigma_{n,v}$ is the capture cross section of electrons(holes), while $v_{n,p}$ is their thermal velocities. For multiple traps of different energy levels and concentrations, the right-hand side of Eq. 3.9 becomes a summation over all trap levels.

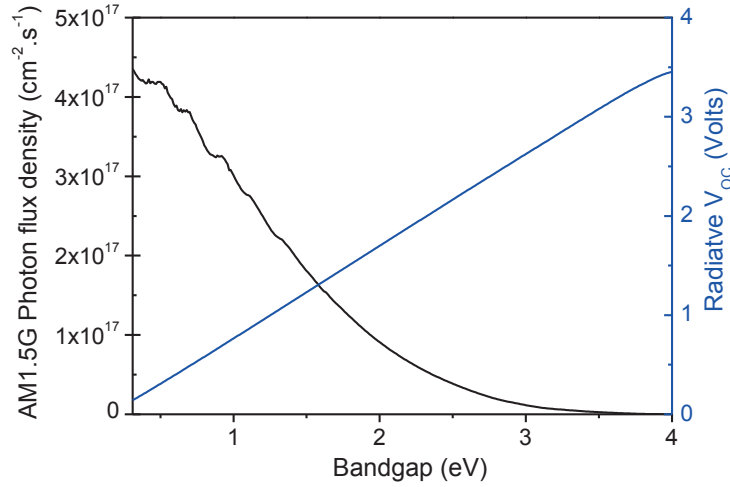


Figure 3.2 Calculated AM1.5G photon flux density and radiative V_{oc} limit as a function of bandgap

A closer look at Eq. 3.9 reveals the following important issues:

- 1) The SRH recombination becomes most efficient when the trap level lies close to the mid-gap, i.e. $E_C - E_T \approx E_T - E_V$. In perovskites, shallow traps closer to the band edges are easier to be created as mentioned in Chapter 1, resulting in slow recombination rates.
- 2) The lifetimes of electrons and holes, $\tau_{n,p}$, are nothing but $(N_T \sigma_{n,p} v_{n,p})^{-1}$ and expectedly, they are inversely proportional to their thermal velocities, to their capture cross sections and to the total trap concentration. For a charged trap, the capture cross section is inversely proportional to the dielectric constant of the material (screening effect). The large dielectric constants reported for perovskites [5], [6] is another possible explanation behind their reduced SRH recombination rates.

Assuming most of the charge carriers are photo-generated, i.e. $n \gg N_C \exp\left(-\frac{E_C - E_T}{k_B T}\right)$ and $p \gg N_V \exp\left(-\frac{E_T - E_V}{k_B T}\right)$, and assuming only one dominant lifetime τ for both electrons and holes (which fits with the fact that effective masses of electrons and holes in perovskites have comparable values), SRH recombination can be approximated by:

$$R_{SRH} \sim \frac{n}{\tau} \left(= \frac{p}{\tau} \right)$$

where τ is the effective lifetime associated with the SRH trap-assisted recombination. As expected from a monomolecular recombination process, the trap-assisted e-h recombination rate scales with the photoexcited carrier density n .

Again, under open-circuit conditions, recombination and generation of charge carriers reach equilibrium, for which:

$$G = R_{SRH} = \frac{n}{\tau}$$

Eq. 3.1 can be exploited again to express V_{OC} in terms of bandgap and illumination intensity for the case of dominant non-radiative SRH recombination, for which we get:

$$eV_{OC} = E_g - 2k_B T_0 \ln \frac{\sqrt{N_c N_v}}{\tau G} \quad (3.10)$$

It can be seen in Eq. 3.10 that the linear relation between V_{OC} versus $\ln(G)$ still holds, but now with the slope doubled to be $2k_B T_0/e$. Figure 3.3 shows the calculated V_{OC} vs. illumination intensity for FAPbBr₃ at different SRH lifetimes. Notice that when the illumination intensity is plotted in logarithmic scale with base 10, a factor of $\ln(e)$ has to be added resulting in a slope of 120 meV/decade. When radiative recombination is dominant, described by Eq. 3.3 above, a slope of 60 meV/decade is obtained. This method of monitoring the intensity-dependent V_{OC} behavior, developed by W. Tress [7]–[10], provides a simple, yet powerful, method to conclude about the origin of recombination processes in solar cell devices. For a situation where both radiative and non-radiative recombination are significant, the slope ranges between 1-2 multiples of $k_B T_0/e$. From Figure 3.3, some important indications about the maximum achievable V_{OC} in perovskite-based solar cells can be anticipated:

- 1) As the SRH lifetime is inversely proportional to the total trap concentration, and taking into consideration the comparable mobilities of electrons and holes, the SRH lifetime can be used as a practical indicator of the total trap density in the perovskite film. Hence, the most obvious approach to increase V_{OC} in the device will be to apply better fabrication strategies that ensure less trap densities, which are expected to be high in solution-processing environments. It can also be noticed from Figure 3.3 that SRH lifetime of $\gtrsim 1 \mu\text{s}$ almost allows us to reach the radiative limit of V_{OC} ; this lifetime value is comparable to the radiative lifetime in FAPbBr₃, as will be discussed below.
- 2) When contact materials are added to sandwich the perovskite from both sides, which is typically the case when solar cell devices are fabricated, then additional advantages and disadvantages will come up. In fact, the nature of the perovskite/contact interface plays an important role in this regard. The contact materials can be arguably considered to work in one of the following two extreme scenarios (see the schematic diagram in Figure 3.4):

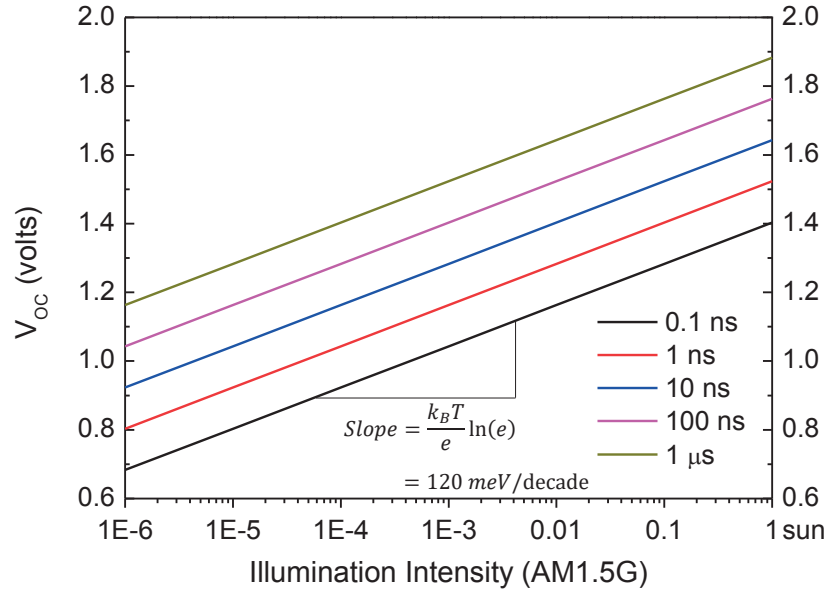


Figure 3.3 V_{OC} vs illumination intensity from AM1.5G source, calculated for FAPbBr₃ of 500 nm thickness with different SRH lifetimes. The bandgap was taken to be 2.3 eV, electron and hole effective masses m_e^* and m_h^* of $0.26 m_e$ each (such that their reduced mass m_r is $0.13 m_e$ according to Ref. [6], which is the only reference found for estimating m_e^* and m_h^* in FAPbBr₃).

- a. Contact materials are efficient e-h separators: as in the case of dye-sensitized solar cells (DSSCs) for example. In this case, charge separation takes place only at the interface. In this scenario: the current flow in the short circuit configuration will be primarily determined by the separation efficiency; however, V_{OC} will be limited to the difference between the work functions of the two contacts. Any energy level difference at the perovskite/contact interfaces will be a loss in V_{OC} . Therefore, a strategy to increase V_{OC} is to reduce those differences, which are usually the difference between CB of perovskite and CB of the electron transport material (ETM) on one terminal, and the difference between perovskite VB and HOMO level of the hole transport material (HTM) at the other contact. After separation, the e-h recombination will be largely reduced as electrons and holes are now spatially separated in different parts of the device (in DSSCs, recombination time is in the range of milliseconds [11]).
- b. Contact materials are efficient selective contacts only: which means electrons at the perovskite/HTM interface are energetically blocked by the LUMO level of HTM, and holes at the perovskite/ETM interface is blocked by CB of ETM, as can be seen in Figure 3.4. However, the e-h separation does not take place at the interface, and it happens earlier before charge carriers arrive at the contacts. If the diffusion length of electrons and holes is long enough, then diffusion and contact selectivity will be a sufficient mechanism for charge separation and current flow. In this case, there will be no V_{OC} losses originating from the energetics of ETM/perovskite and perovskite/HTM interfaces, and V_{OC} will in principle be limited only by its radiative limit. Any losses to V_{OC} will originate thereafter during carrier thermalization inside the contact materials, and not at the interfaces.

There have been some recent important investigations [12]–[14] concluding that, under solar illumination levels, e-h pairs are effectively separated in most available perovskites. This provides a conductive e-h plasma as the primary phase of carrier population, and thus eliminating the need for interfacial separation (as in the case of organic solar cells, in which the high-binding-energy low-mobility excitons can only be dissociated at the interface between two polymers with different electron affinities [9]). This conclusion yet does not completely exclude the existence of separation mechanism at the interfaces. In fact, strong separation efficiencies have been reported between perovskites and some strong ETM electron acceptors, such as PCBM (see for example Refs. [15]–[17]), and strong HTM electron donors, such as Spiro-OMeTAD (see for example Refs. [15]–[18]). At the same time, weak or even no separation have also been reported for other systems; most importantly at CH₃NH₃PbI₃/TiO₂ interface (see Refs. [19], [20] and the results in Chapter 4), with which perovskite solar cells could be fabricated with record efficiencies. Furthermore, as will be seen below in the results of this chapter, V_{OC} that exceeds the built-in potential (as reported in the literature) set by the device contacts in FAPbBr₃-based perovskite solar cell devices is reported, probably for the first time, in this work. Therefore, the working scenario in a perovskite solar cell depends on the materials used in the device architecture and can eventually be a combination of both scenarios above. In both cases, the intrinsic e-h separation mechanisms discussed in Chapter 1 provides, with no additional V_{OC} losses, the fundamental separation mechanism in the perovskite material itself. Additionally, the built-in potential between the two contacts can also be useful in further guiding the photocarriers towards their respective sides, especially with improved crystalline quality [21].

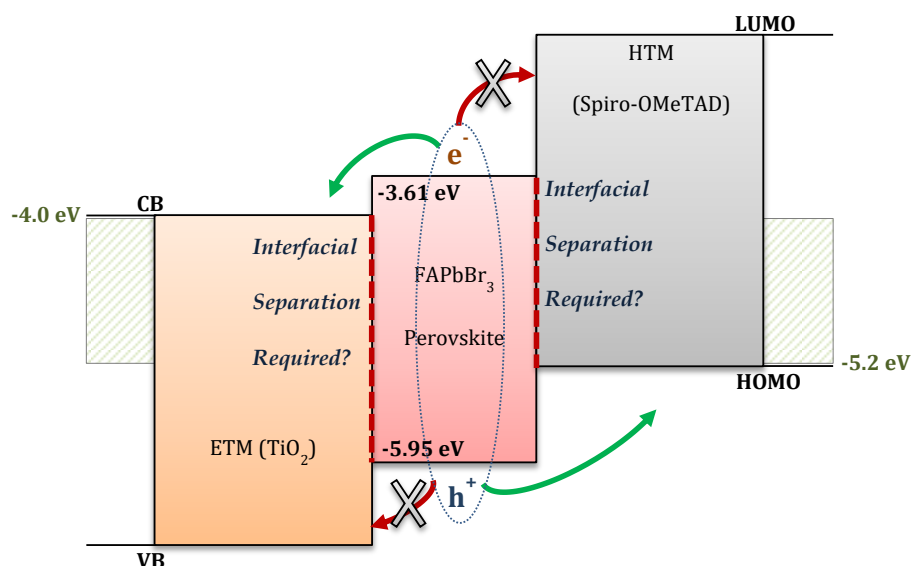


Figure 3.4 A schematic diagram illustrating the energy leveling condition in a perovskite solar cell, and the role of selective contacts.

Another loss mechanism at the interfaces that should not be neglected is the surface recombination. For example, Peng et al [21] reported the fabrication of a perovskite solar cell that is made of a single crystalline MAPbBr₃ film with ultralow trap density, and V_{OC} was still far from the radiative limit. Surface recombination can create significant losses, especially with metal contacts [10]. The highly sensitive nature of perovskite surface to ambient conditions also supports the development of surface complexes/recombination centers as will be discussed later in this chapter. In this regard, passivation methods and inert fabrication and testing environments are important considerations to be taken [21].

Time-resolved Photoluminescence

The recombination mechanisms can be more directly investigated using time-resolved photoluminescence (TRPL). In fact, both radiative and trap-assisted non-radiative recombination will compete in the measured PL decay. Based on the above discussions, the resulting rate equation will look like:

$$\frac{dn(t)}{dt} = -\beta n^2(t) - \frac{1}{\tau} n(t) \quad (3.11^*)$$

Solving Eq. 3.11* gives:

$$n(t) = \frac{1}{\tau\beta} \frac{1}{e^{\frac{t}{\tau}} \left(\frac{1}{\tau\beta n_0} - 1 \right) + 1} \quad (3.12)$$

where n_0 is the initial carrier density upon excitation. The contributions of SRH and radiative recombination in Eq. 3.12 can be decoupled by taking the first order approximation for $\exp(t/\tau) \sim 1 + t/\tau$ (which is valid for time intervals shorter than the non-radiative lifetime τ). Then, Eq. 3.12 becomes:

$$n(t) \approx \frac{n_0}{\left(n_0\beta - \frac{1}{\tau} \right) t - 1}$$

This simplified equation gives a first order approximation of the competition between trap-assisted recombination and bimolecular recombination. It can be revealed from this equation that the lifetime associated with the bimolecular recombination is given by $(n_0\beta)^{-1}$. For excitation densities at $n_0 \sim 10^{15} \text{ cm}^{-3}$, which can be considered as a high excitation density limit for solar radiation [22], and taking $\beta \sim 10^{-9} \text{ cm}^3 \cdot \text{s}^{-1}$, as reported by Ref. [23] for FAPbBr₃, a lower bound of the radiative lifetime can be given at $\sim 1 \mu\text{s}$. With the reported PL decay lifetimes of perovskites in the nanosecond range, this long lifetime reliably suggests that SRH recombination is the dominant recombination mechanism for excited photocarriers in perovskite solar cells. As mentioned above, a practical approach to reach the radiative limit is then to reduce the trap concentration until a SRH lifetime of $\sim 1 \mu\text{s}$ is achieved.

At high excitation densities n_0 , the radiative lifetime increases approaching the SRH lifetime τ . At that specific point, Eq. 3.12 wrongly results in $n(t) \propto \frac{1}{\tau\beta}$. In fact, at such high excitation densities, Auger non-radiative recombination starts to influence the transient dynamics, and hence must be accounted for by introducing a tri-molecular term in Eq. 3.11*, which then reads:

$$\frac{dn(t)}{dt} = -Cn^3(t) - \beta n^2(t) - \frac{1}{\tau}n(t) \quad (3.11)$$

Eq. 3.11 is also known as the *ABC* model, where *A*, *B*, *C* stands for τ^{-1} , β , and the Auger recombination coefficient *C* respectively in the equation. Auger recombination is a non-radiative process, in which the recombination energy of an electron-hole pair is given to a third carrier instead of being emitted as a photon. Auger recombination takes place at very high carrier densities in the range $\sim 10^{18}$ - 10^{19} cm⁻³ [24], orders of magnitude higher than carrier densities under solar illumination.

3.1.2 Short Circuit Measurements

J-V Measurements

Under short-circuit configuration, electrons and holes at the device terminals, already separated by the scenarios mentioned above, will flow to the external load providing the electrical current *I*. The total current density *J* (current/area) for an ideal absorber, limited by radiative recombination only, will be equal to the absorbed photon flux above the bandgap minus the flux of absorber's emission, which, as shown in Eq. 3.6, will depend on the photovoltage *V* that has been developed by illumination across the device terminals. Under short circuit configuration, *V* equals zero. Usually, the power *P* in a solar cell is not extracted at *V* = 0; instead, it is extracted at the maximum power point where the multiplication of current density and voltage is maximized ($P = I \times V$). Therefore, for any voltage *V* across the device and under standard illumination conditions, the expected photocurrent from the device in the radiative limit is given by:

$$J = \text{Solar photons above } E_g(\Phi_{AM1.5G, E_g}) - \Phi_{emission,0} \exp\left(\frac{eV}{k_B T}\right) \quad (3.13)$$

The maximum photocurrent density, called short-circuit current density J_{SC} , is given when *V* is set to zero in Eq. 3.13. Figure 3.5 shows the calculated J_{SC} vs. bandgap in the radiative limit. The standard solar flux $\Phi_{AM1.5G}$ as a function of bandgap is also shown for comparison. For FAPbBr₃, with a bandgap of 2.3 eV, the maximum obtainable current density is 8.9 mA/cm².

The maximum efficiency of a solar cell is estimated from the ratio between the maximum delivered power and the incident AM1.5G photon flux (100.2 mW/cm² in the AM1.5G solar spectrum of Ref. [3]). For a certain bandgap, Eq. 3.8 and Eq. 3.13 can be used to find the maximum power at which the multiplication of *J* and *V* is maximized. This process is carried out for FAPbBr₃, and the resulting *J-V* and *P-V* curves are

shown in Figure 3.6. For FAPbBr₃, the maximum power P_{MAX} occurs at $V_{MAX} = 1.87$ V and $J_{MAX} = 16.44$ mA/cm². The maximum efficiency as a function of bandgap in general is calculated this way, and was previously shown in Chapter 1, Figure 1.4. For FAPbBr₃ with a bandgap of 2.3 eV, the maximum efficiency is estimated to be ~ 16.4%.

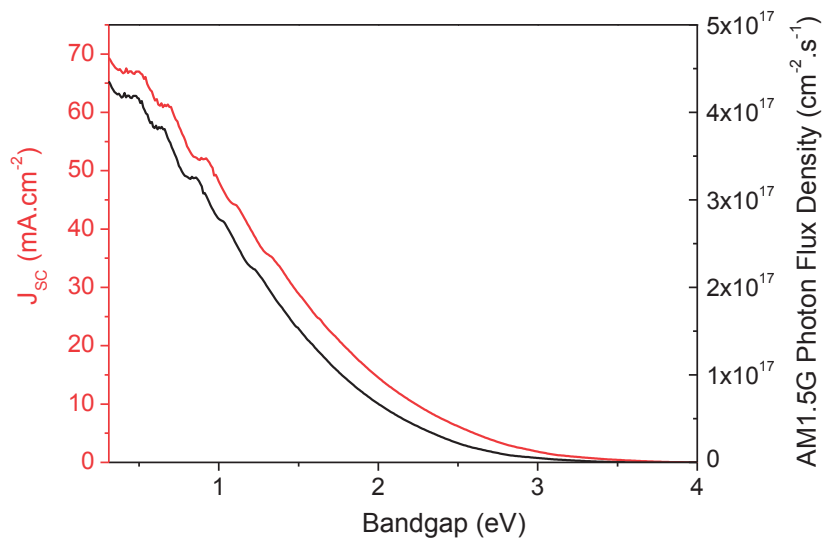


Figure 3.5 Calculated radiative J_{sc} limit and AM1.5G photon flux density as a function of bandgap

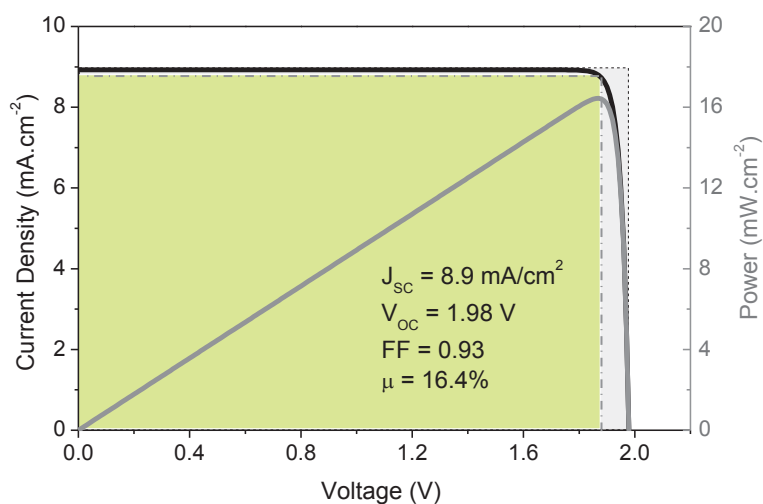


Figure 3.6 Calculated J - V and P - V curves for a FAPbBr₃ solar cell in the radiative limit operating under AM1.5G illumination

The ratio $\frac{\text{Maximum delivered power}}{V_{oc} J_{sc}}$ is called the fill factor FF and, as can be seen in Figure 3.6, FF represents the filling ratio between the two rectangles formed by $V_{MAX} \times J_{MAX}$ and $V_{oc} \times J_{sc}$. Alternatively, the device efficiency can be calculated using the simple formula V_{oc} (in Volts) $\times J_{sc}$ (in mA/cm²) $\times FF$. The

maximum FF of an ideal FAPbBr₃ solar cell device is calculated to be 0.93. As a function of bandgap, it can be shown, using the above arguments, that the FF is an asymptotically increasing function of bandgap within the visible range, as shown in Figure 3.7.

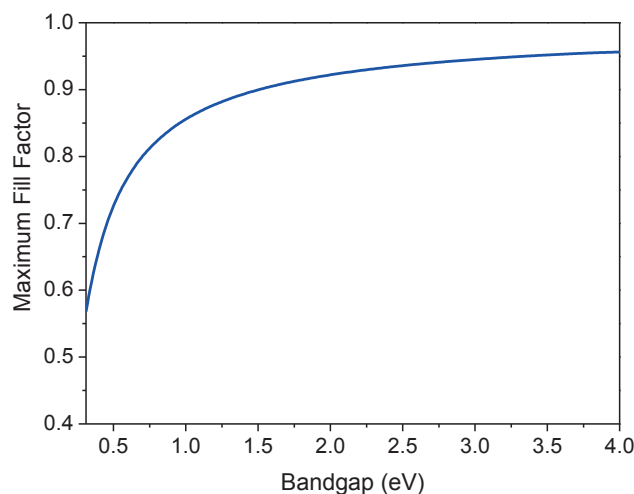


Figure 3.7 Calculated FF as a function of bandgap in the radiative limit under AM1.5G illumination.

IPCE and Electroluminescence Measurements

The reciprocity relation between absorption and emission of a semiconductor discussed above must also be embodied in the corresponding devices when the semiconductor is used for light absorption and light emission applications. In other words, an efficient solar cell must be an efficient light emitting diode (LED) as well. In a solar cell, the spectral quantum efficiency is measured, as a function of incident photon energy, from evaluating the ratio of (output short-circuit current density)/(incident photon flux) for each monochromatic photon energy (wavelength). This technique is referred to as IPCE, standing for Incident-Photon-to-Current Efficiency, or EQE_{PV} , standing for photovoltaic External Quantum Efficiency. The $EQE_{PV}(E)$ spectrum generally follows the absorption spectrum, with its onset at the bandgap energy. Integration of $EQE_{PV}(E)$ (multiplied by the spectral photon flux and the fundamental electronic charge) over the whole absorption range ideally produces the value of J_{SC} .

In LEDs, the electrical injection of current produces a light flux with photon energy of the order of the semiconductor bandgap. This is called electroluminescence. The quantum efficiency of an LED device as a function of applied voltage/current settings can be similarly estimated, which we denote EQE_{LED} .

EQE_{PV} and EQE_{LED} are experimentally measured values that basically quantify the efficiency of absorption/emission processes in a semiconductor device under real, non-ideal conditions. Therefore, the question is whether they can be used to generalize the detailed balance theory such that non-ideality factors, e.g. non-radiative recombination, can also be included. U. Rau could successfully do this

generalization to the detailed balance theory, and details can be consulted in his pioneering paper [25]. An important result of his work is the reciprocity relation between the open circuit voltage V_{OC} and EQE_{LED} , with which the photovoltage loss resulting from non-radiative recombination $\Delta V_{nonrad.}$ can be estimated by the following equation [25]:

$$\Delta V_{nonrad.} = V_{OC}^{rad} - V_{OC} = -\frac{k_B T}{e} \ln(EQE_{LED}) \quad (3.14)$$

At full quantum efficiency of 1, i.e. a perfect emitter, the non-radiative loss in V_{OC} is zero and V_{OC} will be equal to its radiative limit.

3.1.3 Beyond Illumination Level of Solar Radiation: Light Amplification

As mentioned above, the electron and hole quasi-Fermi levels separation in a semiconductor determines the radiative limit of its V_{OC} . Instantly upon excitation, excited electrons in the conduction band and excited holes in the valence band will be each under a non-equilibrium thermal condition. After that, both electrons and holes will rapidly thermalize within their respective bands to their respective quasi-Fermi levels. This thermalization process (measured for example by Ref. [15] to take place in ~ 0.4 ps in MAPbI₃) is much faster than the e-h inter-band recombination (\sim ns). Therefore, electrons and holes can safely be approximated by quasi-Fermi Dirac distributions in their respective bands.

At low illumination densities, as in the case under solar illumination levels, E_F^n lies below the conduction band edge, while E_F^p lies above the valence band edge. At higher illumination levels, the splitting between the two quasi-Fermi levels $E_F^n - E_F^p$ increases pushing E_F^n and E_F^p deeper in their respective bands, as shown in Figure 3.8. As more carriers are available in the conduction band in this case, the detailed thermodynamic balance between absorption and stimulated emission will then favor a higher rate of stimulated emission. It can be shown that light amplification, i.e. gain, can be realized only when the quasi-Fermi level splitting achieves the following condition [24], [26]:

$$f_c(E) - f_v(E) > 0 \quad (3.15)$$

where $f_c(E)$ and $f_v(E)$ are now, respectively, the occupation probabilities of conduction band and valence band under quasi-thermal equilibrium, and are given by [24]:

$$f_c(E) = \frac{1}{1 + \exp\left(\frac{E_{c, ph} - E_F^n}{k_B T}\right)} \quad ; \quad f_v(E) = \frac{1}{1 + \exp\left(\frac{E_{v, ph} - E_F^p}{k_B T}\right)} \quad (3.16)$$

where $E_{c, ph}$ and $E_{v, ph}$ are functions of the incident photon energy E such that $E = E_{c, ph} - E_{v, ph}$. From Eq. 3.15, we find that:

$$E_F^n - E_F^p > E_{c, ph} - E_{v, ph} \quad (= \text{energy of the emitted photon}) \quad (3.17)$$

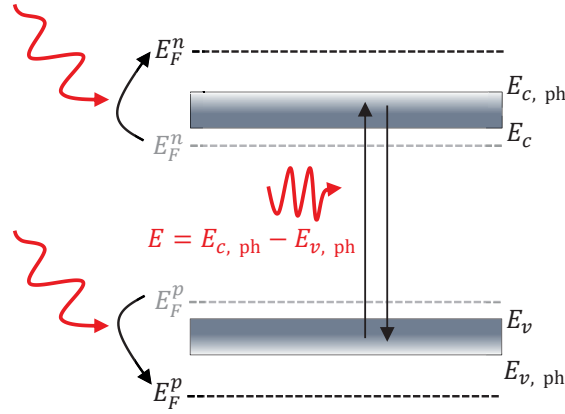


Figure 3.8 Illustration of the Bernard–Durrafourg condition for stimulated emission in semiconductors

Eq. 3.17 is known as the Bernard–Durrafourg condition [26], and it implies that only those emitted photons whose energies are below the quasi-Fermi levels splitting and above the bandgap can be amplified. Therefore, in order to realize amplification of the semiconductor’s spontaneously emitted photons, the separation has to be increased through a higher population of carriers until $E_F^n - E_F^p$ exceeds the bandgap. Once the Bernard-Durrafourg condition is realized, the spontaneously emitted photons may be amplified by the structure. This sequential process of *amplification* (by stimulated emission, without the presence of mirrors allowing a laser feedback) of previously *spontaneously emitted* photons is called *Amplified Spontaneous Emission (ASE)*.

In an ideal semiconductor of a direct bandgap, and for photons at a given energy E , the optical gain factor can be written as [24], [27]:

$$g(E) = -\alpha(E) = -\alpha_0(E)[f_c(E) - f_v(E)] \quad (3.18)$$

where $\alpha_0(E)$ is the absorption coefficient of the empty conduction band. As indicated by Eq. 3.18, the gain factor and absorption coefficient are directly governed by the inversion factor $f_c(E) - f_v(E)$. At low carrier injection levels, $f_c(E) - f_v(E) < 0$ and α is a positive quantity. When the Bernard–Durrafourg condition is achieved, we have a negative absorption coefficient, indicating gain.

For semiconductors with small exciton binding energies, $\alpha_0(E)$ simply follows the form of density of states of band-to-band transitions ($\alpha_0(E) \propto \sqrt{E - E_g}$). For semiconductors with larger exciton binding energies, the oscillator strength is enhanced and modified by the Coulomb interaction between electrons and holes. This first allows creating discrete states below the conduction band that represent *bound* electron-hole pairs, the *excitons*. These sub-bandgap exciton states can be approximated (assuming a hydrogen-like system) by:

$$E_n^b = E_g - \frac{E_b}{n^2} = E_g - \frac{R \mu}{\epsilon_r^2 n^2}, \quad n = 1, 2, 3 \dots$$

The quantity E_b is the exciton binding energy. μ and ϵ_r are respectively the reduced mass of the exciton and the dielectric constant, and R is the Rydberg constant (13.6 eV). The electron-hole correlation will also increase the “continuum” absorption above the excitonic states, resulting in a sharp discontinuity in the absorption spectrum at the bandgap, rather than the slowly increasing $\sqrt{E - E_g}$ function. This absorption enhancement is the so-called Sommerfeld enhancement factor F_{enh} , which takes the form [13], [28]:

$$F_{enh} = \frac{2\pi \cdot \sqrt{\frac{E_b}{E - E_g}}}{1 - \text{Exp}(-2\pi \cdot \sqrt{\frac{E_b}{E - E_g}})} \quad (3.19)$$

Considering the excitonic effects above, $\alpha_0(E)$ can be given by [13], [24], [28], [29]:

$$\alpha_0(E) \propto \sqrt{E - E_g} \cdot \theta(E - E_g) F_{enh} + \sum_{n=1}^{\infty} \frac{2E_b^{\frac{3}{2}}}{n^3} \delta(E - E_n^b) \quad (3.20)$$

where $\theta(E - E_g)$ and $\delta(E - E_n^b)$ are the Heaviside step function and the Dirac delta function respectively. The first term in Eq. 3.20 represents the Sommerfeld enhanced continuum absorption. It can be noticed that the numerator of F_{enh} (see Eq. 3.19) cancels the $\sqrt{E - E_g}$ term of density of states, resulting in a sharp discontinuity of absorption at the band edge. The second term in Eq. 3.20 represents the absorption of excitonic states below the bandgap.

Knowing $\alpha_0(E)$, which is usually measured using the linear absorption spectrum, the gain factor as a function of carrier density n and/or temperature can be estimated, for which analytical expressions for $E_F^n(n, T)$ and $E_F^p(n, T)$ must be derived. Various approximations have been developed for this purpose; one of them that applies to a wide range of carrier densities in bulk semiconductors is the Joyce-Dixon expression [30]:

$$E_F^n(n, T) = E_c + k_B T \ln\left(\frac{n}{N_c}\right) + k_B T \sum_{i=1}^4 A_i \left(\frac{n}{N_c}\right)^i$$

$$E_F^p(n, T) = E_v + k_B T \ln\left(\frac{p}{N_v}\right) + k_B T \sum_{i=1}^4 A_i \left(\frac{p}{N_v}\right)^i$$

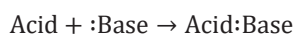
where $A_1 = 3.53553 \times 10^{-1}$; $A_2 = -4.95009 \times 10^{-3}$; $A_3 = 1.48386 \times 10^{-4}$; $A_4 = -4.42563 \times 10^{-6}$.

At very high carrier densities, the Coulomb interaction between electrons and holes can induce additional effects. Auger recombination is one effect that has been mentioned above, which can severely reduce the gain. Also, both the bandgap and exciton binding energy are pushed to lower values at higher carrier densities, a process called re-normalization, until all excitons are ionized into electron-hole plasma at a carrier density threshold state called the “Mott transition” [31], [32].

3.2 Description of Samples

Two FAPbBr₃ films, FA(1) and FA(2), deposited on a 300 nm mesoporous layer of TiO₂, were prepared by Dr. Neha Arora within a collaboration with the group of Prof. Nazeeruddin, EPFL. Details of sample and device preparations can be found in Ref. [33]. In brief, a sequential deposition technique was used where a film of PbBr₂ (previously deposited by spin coating a solution of PbBr₂ dissolved in a specific solvent) is spin coated, heated at 80 °C for ~ 15 minutes, and then transformed to FAPbBr₃ by dipping into an isopropanol solution of FABr. FA(1) and FA(2) differ in the solvent used to prepare the PbBr₂ films: in FA(1), dimethylformamide (DMF) is used, while in FA(2), a 1:1 volume ratio of DMF and dimethyl sulfoxide (DMSO) is used.

In this work, the solvent proved to have a determining role in the resulting morphology and quality of the films, and so on the device and ASE characteristics. The role of DMSO and DMF solvents on the PbBr₂ films can be explained as follows. First, metal halides in general work as good Lewis acids [34]; i.e., in the presence of Lewis bases, an acid-base complex can be formed according to the following equation:



where the two vertically aligned dots represent the electron pair donated by the Lewis base (a Lewis base is defined as an electron-pair donor while an acid is an electron-pair acceptor). In fact, both DMF and DMSO are Lewis bases, so they can donate an electron-pair to PbBr₂ forming PbBr₂.Base complexes. However, when DMF and DMSO are compared, DMSO has a stronger basicity [34]. Also, DMSO has a higher coordination ratio with PbBr₂ than DMF; two DMSO molecules coordinate with one Pb atom [35], while in DMF the coordination is 1:1 with even a longer bond length [36]. The high boiling point of DMSO (189 °C compared to 152 °C for DMF), with above mentioned stronger basicity and coordination, will further allow PbBr₂.DMSO complexes to stay even after deposition. Therefore, when both DMF and DMSO are present (as in sample FA(2)), DMSO can be considered as the dominating Lewis base, while DMF mostly provides the reaction environment in this case.

The main advantage of having a PbBr₂.DMSO complex is that this slows down the crystallization process of PbBr₂. Fast crystallization of PbBr₂ during the spin-coating process makes it hard to control the film growth, and the PbBr₂.DMSO complex formation actually introduces an intermediate step to control the growth speed. After this “retarded-crystallinity” spin-coating process, both DMSO and DMF molecules rapidly escape from the film when heated at ~ 70-80 °C or above [33], [34].

3.3 Results and Discussion

3.3.1 Time-resolved PL and Photovoltaic Studies

Figure 3.9 shows the resulting morphology of the FAPbBr₃ films, FA(1) and FA(2), revealed by Field Emission Scanning Electron Microscopy (FE-SEM) images. The sample FA(1) shows a non-uniform

coverage of the perovskite film, most probably due to the faster uncontrollable growth when the DMF solvent is used. Single crystals of submicron sizes that are non-uniformly distributed over the poorly covered surface can also be noticed. On the contrary, when DMSO is present, FA(2) showed a superior, almost continuous coverage of the film with larger grain sizes. This striking difference in film coverage between FA(1) and FA(2) clarifies the vital role of solvent in the resulting morphology of the films.

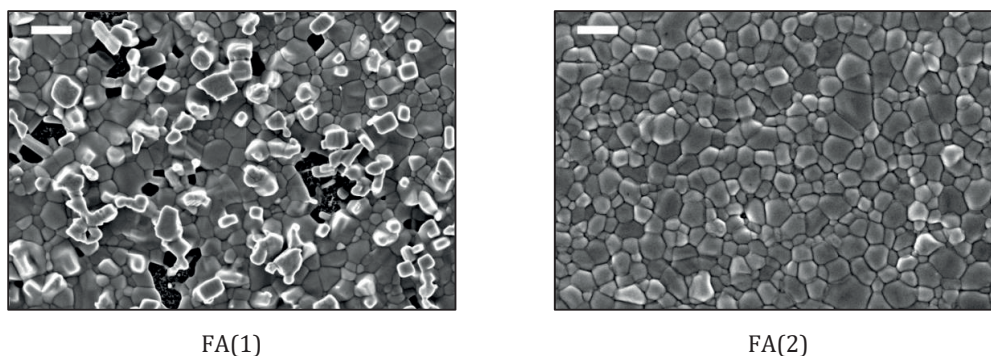


Figure 3.9 Top-view FE-SEM images for FA(1) (left) and FA(2) (right) samples. Scale bar = 1 μm .

The poor film coverage in FA(1) can facilitate the formation of parasitic contacts in the solar cell structure when HTM and gold materials are subsequently deposited to terminate the cell, which can strongly reduce the overall efficiency of the device. That was in fact noticed as will be discussed below (see Figure 3.11). However, the question still holds whether the nature of the solvent used also affects the intrinsic properties of the grown films, rather than their morphologies only. Time-resolved photoluminescence (TRPL) measurements were carried out on bare FA(1) and FA(2) samples and the results are shown in Figure 3.10. It is evident from Figure 3.10 that FA(2) has a better optical quality, manifested by more than one order of magnitude longer PL lifetime compared to FA(1). The PL decay of FA(2) shows a single exponential decay with a lifetime of ~ 31 ns. On the other hand, the PL decay of FA(1) has two decay channels, with lifetimes of ~ 0.3 ns and 2.1 ns, with the shorter lifetime (0.3 ns) contributing for about two-third to the overall PL decay. Therefore, it can be concluded that the solvent plays a significant role in the determination of the film optical quality as well.

As discussed in Sec. 3.1, the PL decay can be used as a qualitative measure of the total concentration of traps in perovskite films. Hence, it can be concluded that FA(1) has developed a higher density of traps than FA(2). This result is also confirmed by time-integrated photoluminescence (TIPL) measurements shown in Figure 3.11 at 15 and 300 K. At 300 K, FA(2) showed a PL emission that is ~ 10 times stronger than FA(1). This contrast between the two samples was not so strong when the measurements were performed at 15 K (Figure 3.11b). At 15 K, comparable values for FA(1) and FA(2) are obtained. At low temperature, non-radiative recombination channels are reduced resulting in the recovery of the PL signal for both samples (notice that the y-axis in both Figure 3.11a and Figure 3.11b has the same scale). The fact that the films assume an orthorhombic crystalline phase at 15 K [6] (compared to the cubic phase at room temperature), which is observed as a ~ 50 meV red-shift in the PL spectra at 15 K in Figure 3.11, does not

change our conclusion. In fact, at low temperature, higher crystalline order and lesser thermal vibrations will also contribute to increasing the PL intensity. However, the PL recovery of FA(1) from one order of magnitude less than that of FA(2) to a comparable PL intensity confirms that there was more “switching-off” of the non-radiative recombination in FA(1) compared to FA(2).

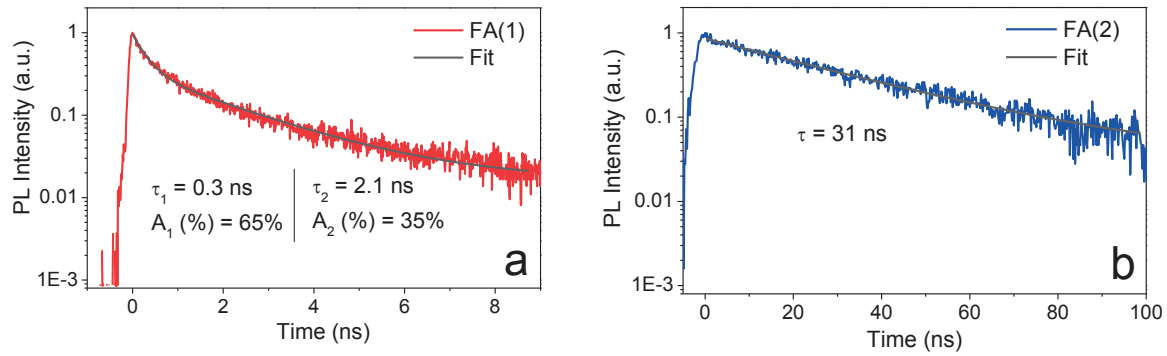


Figure 3.10 TRPL measurements for FA(1) and FA(2) at 300 K. The samples were excited with ~ 2 ps pulses of 425 nm wavelength and energy density ranging between ~ 0.05 - $0.5 \mu\text{J}/\text{cm}^2$, which corresponds to 1-10 mW/cm^2 .

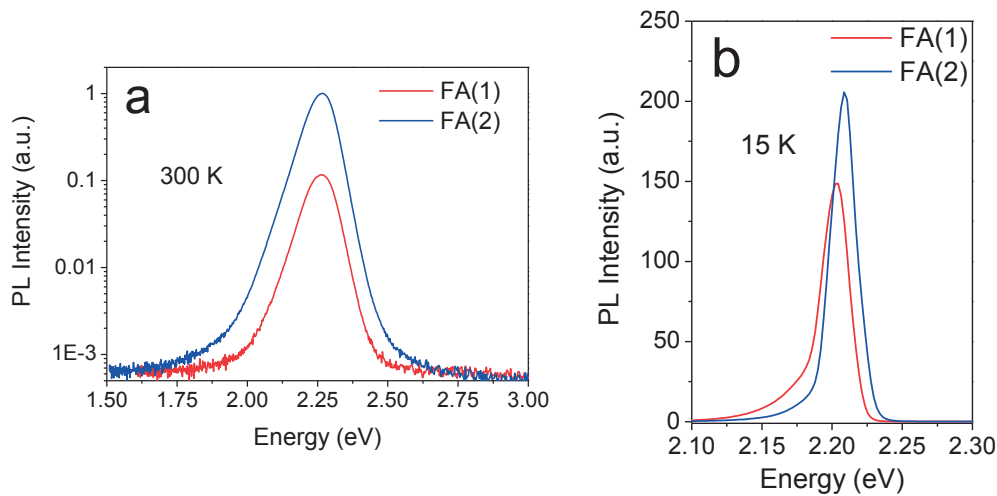


Figure 3.11 TIPL measurements for FA(1) and FA(2) at 15 and 300 K. The y-axis scale is the same for both figures. The samples were excited with ~ 2 ps pulses of 425 nm wavelength and energy density ranging between ~ 0.05 - $0.5 \mu\text{J}/\text{cm}^2$, which corresponds to 1-10 mW/cm^2 .

According to Sec. 3.1, we can conclude that, at room temperature, the trap-assisted recombination is dominant since the lifetimes are in the range ~ 0.3 - 31 ns for both samples, which is far from the radiative bimolecular recombination lifetime estimated in Sec. 3.1 to be $\geq 1 \mu\text{s}$ under 1 sun ($\sim 10^{15} \text{cm}^{-3}$). During the TRPL experiments, the average pulse energy was kept in the range between 0.05 - $0.5 \mu\text{J}/\text{cm}^2$ per pulse, which corresponds, taking into account the film absorption as will be detailed in the ASE studies below, to

an excited carrier density of $\sim 10^{15}$ - 10^{16} cm^{-3} . This value is within the upper range of AM1.5G illumination density, and it so excludes the possibility that bimolecular recombination importantly contributes to the PL decays in Figure 3.10.

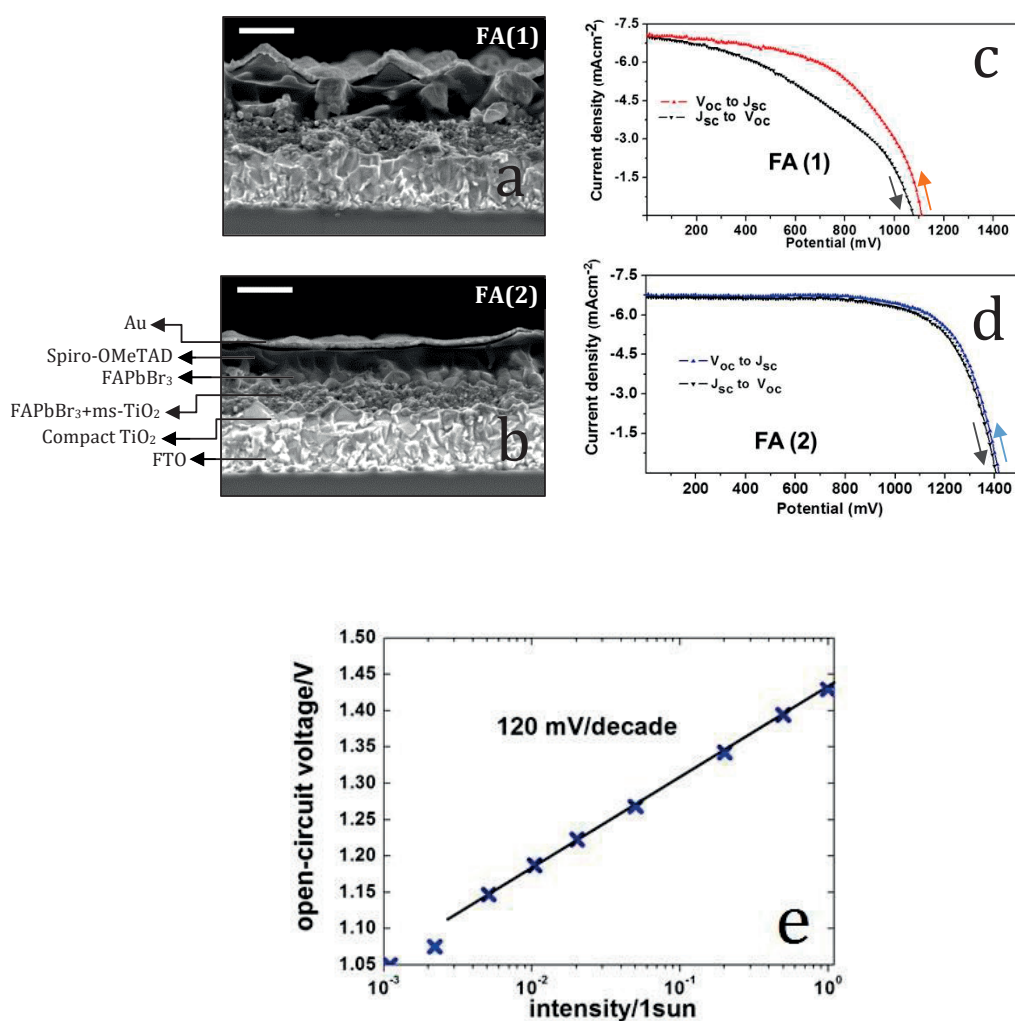


Figure 3.12 (a,b) Cross-sectional FE-SEM images for FA(1) (a) and FA(2) (b). Scale bar = 500 nm. (c-d) J-V curves for FA(1) (c) and FA(2) (d) under AM1.5G illumination. (e) V_{oc} versus light illumination intensity for FA(2).

Table 3.1 J_{sc} , V_{oc} , FF and PCE values extracted from Figure 3.12 for FA(1) and FA(2) devices

Sample	J_{sc} (mA/cm ²)	V_{oc} (V)	FF	PCE (%)
FA(1)	7.1	1.14	0.67	5.4
FA(2)	6.8	1.42	0.72	7.0

The cross-sectional FE-SEM images and J-V curves of solar cell devices, fabricated by deposition of Spiro-OMeTAD as HTM layer and gold (Au) as a top contact, are shown in Figure 3.12. Light intensity dependent V_{OC} measurements were also carried out, and a typical V_{OC} versus light intensity (in log scale) is also shown in the same figure. From Figure 3.12d, sample FA(2) showed a strikingly high V_{OC} of 1.42 V, which was a record at the time of publication; however, FA(1) showed a much reduced V_{OC} of 1.14 V and a considerable hysteresis as can be seen in Figure 3.12c. FA(1), however, showed a relatively higher J_{SC} , due to its higher thickness as can be revealed by the cross sectional FE-SEM images. The overall power conversion efficiencies were 5.4% and 7% respectively for FA(1) and FA(2) samples. Table 3.1 summarizes the values of J_{SC} , V_{OC} , FF and efficiencies for both cells. The light intensity dependent V_{OC} (Figure 3.12e) shows a linear relation between the logarithm of light intensity and V_{OC} , whose slope is calculated to be 120 meV/decade. The slope did not decrease over few decades of light intensity up to 1 sun, which, according to Eq. 3.10, further confirms that SRH recombination is the dominant mechanism of recombination.

The high contrast in V_{OC} between FA(1) and FA(2) can be attributed to two reasons. The non-homogeneous coverage of FA(1), as seen in the top view FE-SEM in Figure 3.9 and confirmed by the cross-sectional FE-SEM image in Figure 3.12, is one reason. In fact, parasitic contacts between the HTM and TiO₂ layers can be clearly seen in Figure 3.12a. This was not the case for FA(2) where the TiO₂/FAPbBr₃/HTM/Au multilayers have remarkable continuity and homogeneity in the lateral directions. The existence of parasitic contacts works as a shunt resistance in the device, which has a direct impact on reducing both V_{OC} and FF , in agreement with the J - V results. The second important reason behind the reduced V_{OC} is the inherent optical qualities of the FAPbBr₃ films, which are reflected above by their PL decays. As discussed in Figure 3.3, a trap-assisted lifetime sets an upper limit for the maximum achievable V_{OC} . Eq. 3.10 is used to estimate the maximum possible V_{OC} for both films, assuming electron and hole effective masses m_e^* and m_h^* of $0.26 m_e$ [6] and employing the corresponding film thicknesses. The maximum V_{OC} is calculated for FA(1) and FA(2) to be 1.46 V and 1.70 V respectively. This result informs that, even with the record V_{OC} value for FA(2) of 1.42 V, there is still room for further improvement. In fact, 1.53 V was later achieved by Arora et al [37], who fabricated the samples presented in this chapter as well, with FAPbBr₃ films having comparable PL lifetimes. This accomplishment was achieved by engineering the FAPbBr₃/TiO₂ interface, without any further improvement to the FAPbBr₃ film itself [37]. This, in fact, reveals the power of using the carrier lifetime to first estimate the maximum achievable V_{OC} , and to surmise, based on that, about the other origins of V_{OC} losses. For FA(1), the larger difference between experimental and calculated V_{OC} indicates that origins other than the trap-assisted recombination in the FAPbBr₃ film are also responsible for the reduced V_{OC} , such as the existence of parasitic contacts discussed above.

The record V_{OC} of 1.42 V for FA(2) is larger than the typically reported built-in potential that is set by the TiO₂ and Spiro-OMeTAD. The vacuum energy levels of CB of TiO₂ and HOMO of SpiroOMeTAD are reported, for example by Ref. [38], to be located at ~ -4.0 eV and -5.2 eV, setting a built-in potential between the device terminals of ~ 1.2 eV. According to these values, the energetics of the contact materials, based on the above reported values, do not define the maximum possible V_{OC} in our devices, which could support the

conclusion that no separation occurs at the interfaces. However, inside the contact materials after that, carriers will undergo thermalization in their respective contacts, and the energetics of the contact materials would ultimately define the final voltage difference. Therefore, the statement that our record V_{OC} exceeded the built-in potential between the two contacts is still a hard claim to be concluded, and a revision of energy levels for both FAPbBr₃ and contact materials need to be considered.

Electroluminescence measurements were carried out by forward biasing the devices with injection currents comparable to the J_{SC} values (between ~ 5 - 10 mA/cm²), and EQE_{LED} was found to be in the range of $\sim 10^{-7}$ - 10^{-8} . Using Eq. 3.14, the loss of V_{OC} due to non-radiative recombination is estimated to be ~ 0.4 - 0.5 volts, which sets an expected V_{OC} of ~ 1.5 V. This is, indeed, approximately what is obtained for the FA(2) sample.

It is important to mention here that the V_{OC} estimated by Eq. 3.10 and Eq. 3.14 have different meanings. V_{OC} estimated by Eq. 3.10, using TRPL decay, estimates the maximum obtainable V_{OC} given a certain SRH carrier lifetime. In other words, it reflects an intrinsic non-ideality in the perovskite film itself, and has nothing to do with additional interfacial recombinations/transport issues. On the other side, Eq. 3.14, measuring EQE_{LED} , predicts V_{OC} for the measured device, and thus will be affected by non-idealities in the contacts and/or in the charge transport as well. This way, TRPL measurements, with the use of Eq. 3.10, helps decoupling the interfacial effects that can possibly degrade V_{OC} from the intrinsic optical quality of the perovskite film itself, which can definitely guide the work towards further development of the device.

3.3.2 Amplified Spontaneous Emission Studies

The detailed balance principle ensures the reciprocity between absorption and emission processes in a light absorbing material. In fact, materials used for solar cells show varying behaviors in this regard. For example, with Silicon, the most used solar cell material, EQE_{LED} is very low hardly reaching 1% [39]. In contrast, solar cells made of organic materials, despite their poor photovoltaic efficiency, have a much larger EQE_{LED} of up to $\sim 30\%$ [40]. This contrasted behavior can be understood by the interplay between the mobility of carriers and non-radiative recombination inside the light absorber. In organic solar cells, with very low non-radiative recombination and exciton-based charge separation mechanism [9], the “slow” high-binding-energy excitons (binding energy \sim few hundreds of meV, mobility $\sim 10^{-2}$ - 10^{-3} cm²V⁻¹s⁻¹ [9]) have a better chance to recombine and emit photons than to dissociate and be collected at the device terminals. In silicon solar cells for example, as the other extreme, the high carrier mobility ($\sim 10^2$ - 10^3 cm²V⁻¹s⁻¹ [41]) allows a more efficient charge collection, and so higher photovoltaic efficiency. However, the non-radiative recombination is responsible in this case for the reduced emission efficiency. Here, perovskite materials come as an intermediate material with “decent” mobilities (~ 50 - 300 cm²V⁻¹s⁻¹ [42]), “decent” exciton binding energies as well (~ 10 - 100 meV [14]), and “shallower” traps in the bandgap. These properties make perovskites in general very promising to succeed in light emitting applications as they already did in photovoltaics.

As discussed in Chapter 1, FAPbBr₃ has its own special characteristics among other perovskites that make it more promising for light emitting applications, most importantly the wide tunability of FAPbBr₃ emission over the “green gap” region (see Figure 1.9). In fact, there have been many reports already on the successful application of FAPbBr₃ in LEDs [43]–[45]. This in fact leads one step further to questioning whether light amplification in FAPbBr₃ is also possible at higher carrier densities, motivated by a few successful examples on iodide-based perovskites that appeared during the course of this work [13], [17], [46]–[50], and other older works on 2D perovskites [51]–[53]. Interestingly, amplified spontaneous emission (ASE), for the first time for this important perovskite material, could be realized for both samples FA(1) and FA(2), with a threshold carrier density as low as $2 \times 10^{18} \text{ cm}^{-3}$. This ASE demonstration was carried out on the same FA(1) and FA(2) samples that were optimized for the mesoporous solar cell devices, without any further optimization for ASE performance, flooring great expectation for efficient FA-based perovskite green semiconductor lasers in the future.

Figure 3.13a & b shows the evolution of ASE while increasing the pump fluence of 450 nm laser excitation pulses of ~ 70 picosecond pulse duration. At low pump fluence, the PL spectrum shows a broad peak centered at 2.326 eV, which corresponds to spontaneous emission (SE). At the threshold pump fluence, ASE is associated with the emergence of a sharp peak at the lower energy side of the broad band, centered at 2.226 eV and 2.214 eV for FA(1) and FA(2) respectively.

There have been few reports in the literature on the origin of these two peaks in different perovskite materials. Xing et al [17] suggested the occurrence of excitonic ASE, rather than from ionized photocarriers, at the lower energy side of the exciton band, that satisfies the population inversion condition below the Mott transition. This interpretation is built up following the rigorous study on (Zn,Cd)Se/ZnSe quantum well lasers carried out by Ding and co-workers [54]. Although a clear excitonic band can be noticed in our samples as seen in the absorption spectra (see Figure 3.14), fulfilling the other conditions required by Ref. [54] to have such excitonic gain is questionable for perovskite materials. Specifically, the requirement of having appreciable inhomogeneous broadening compared to homogenous thermal broadening [54] is not the case in perovskite materials [55]–[58]. Kondo et al attributed the emergence of the lower-energy ASE peak to biexcitons [51]. In fact, a 2D multilayered perovskite material, having a high exciton binding energy as discussed in Chapter 1, was used in their study. A high exciton binding energy increases the probability of biexciton formation. With our 3D perovskite, having around one order of magnitude lower exciton binding energy [59], [60], this proposition is also doubtful. Priante et al proposed that the two peaks originate from surface defects, with the higher energy one having a limited density of states (DOS) while the lower energy peak has a much higher DOS [61]. Their explanation was inspired by the fact that with high quality single crystals only a single peak was observed [62], while the two peaks appeared from polycrystalline samples prepared under very mild conditions [61]. Chen et al [63] carried out ultrafast broadband PL and absorption studies and observed a short-lived (10 ps) PL emission that originates from uncorrelated hot carriers above the bandgap. This is followed by a stronger and sharper ASE peak on the low energy side after hot carriers have thermalized [63]. According to this scenario, ASE originates from band-to-band transitions, while SE originates from the recombination of uncorrelated carriers above the

bandgap that takes place before carriers thermalize. Indeed, in all cases, sample preparation conditions, to which perovskites are highly sensitive, can result in highly contrasted behaviors, for which different origins of the two peaks are also possible.

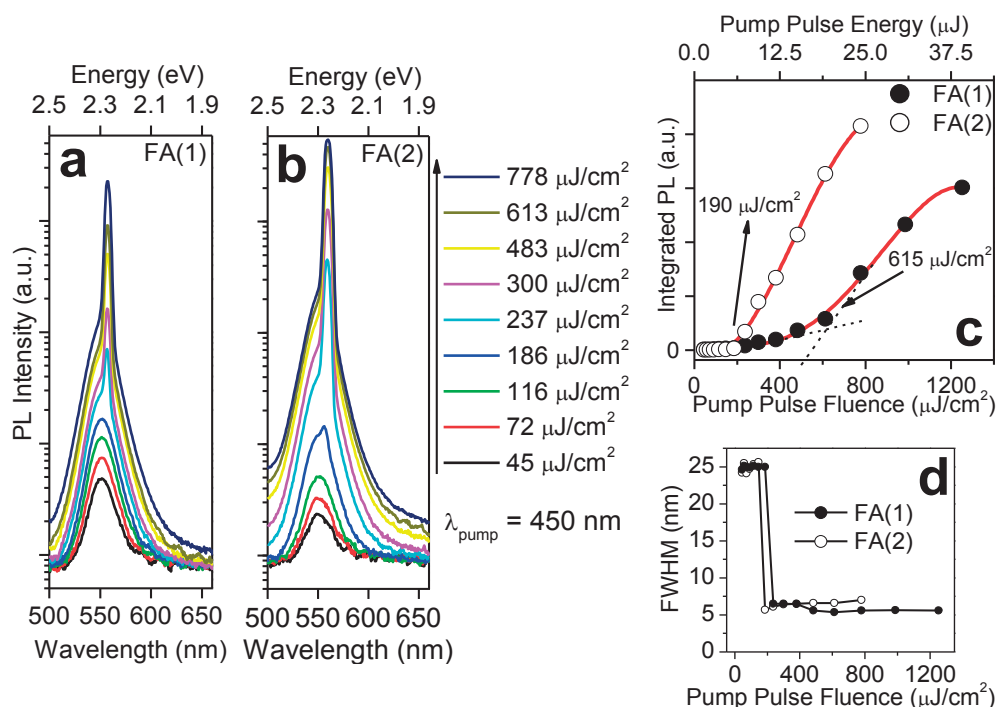


Figure 3.13 Evaluation of the PL spectra with increasing pump pulse fluence for FA(1) (a) and FA(2) (b) samples. The y-axes are of the same logarithmic scale for the two figures. (c) Integrated PL intensity versus pump fluence for FA(1) (solid circles) and FA(2) (open circles) samples showing, respectively, the ASE threshold at 190 $\mu\text{J}/\text{cm}^2/\text{pulse}$ and 615 $\mu\text{J}/\text{cm}^2/\text{pulse}$, and (d) Evolution of FWHM with increasing pump fluence for FA(1) (solid circles) and FA(2) (open circles).

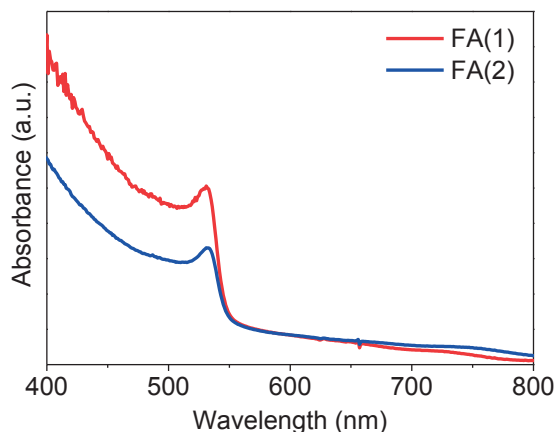


Figure 3.14 Absorbance spectra for FA(1) and FA(2).

From Figure 3.13b, sample FA(2) showed a sharp SE to ASE transition at a pump fluence of 190 $\mu\text{J}/\text{cm}^2$ per pulse. This fluence value corresponds to an ASE threshold carrier density of $\sim 2 \times 10^{18} \text{ cm}^{-3}$, calculated from the absorbance spectra (see Figure 3.14) and sample thicknesses (estimated from Figure 3.12), assuming 70% filling of perovskite in the ms-TiO₂ layer. This value is within reported values for threshold carrier densities in MAPbI₃ perovskites [13], [17], possibly indicating that Br and I contribute equally to the density of states in the perovskite lattice, with the organic cation still contributes minimal, as discussed in Chapter 1, even with the FA ion. FA(1) showed (Figure 3.13a), on the other hand, a slower ASE growth with increasing pump fluence. This rendered it more difficult to define the lasing threshold that we estimated to be $\sim 615 \mu\text{J}/\text{cm}^2$ using the two-segment method. This threshold value corresponds to a threshold carrier density of $\sim 7 \times 10^{18} \text{ cm}^{-3}$ which is still within the same order of magnitude as FA(1). FA(2) showed a higher quantum efficiency (as can be deduced from the larger slope in the linear region), while FA(1) suffered from a reduced quantum efficiency, faster ASE saturation and, although having more generation volume of the perovskite emitter than FA(1), less quantum yield. Indeed, this strong contrast between the two samples clearly illustrates the importance of chemical growth environment in the optical and gain characteristics of grown perovskite films.

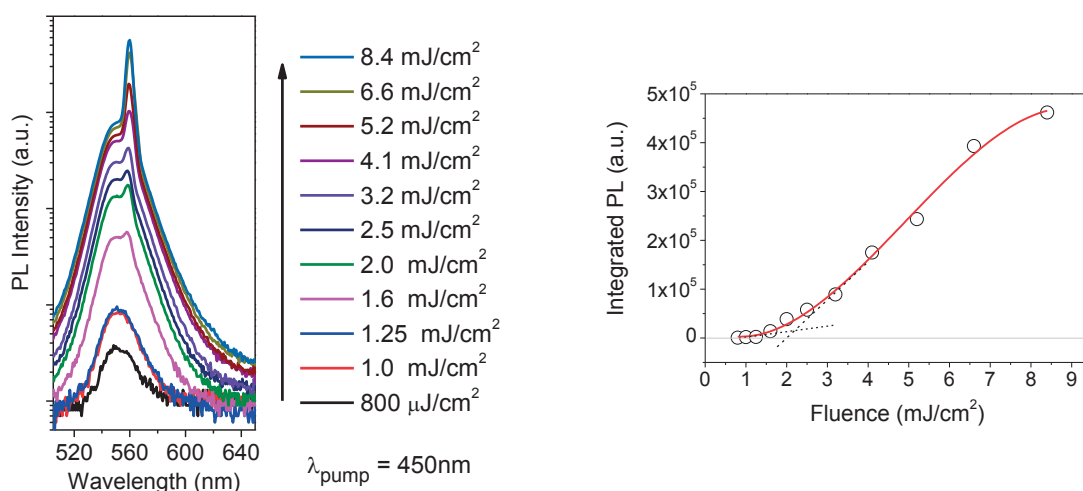


Figure 3.15 (a) Evolution of PL intensity with increasing pump fluence across the ASE threshold when the Spiro-OMeTAD layer is deposited on perovskite layer in FA(2) sample. (b) Integrated PL intensity vs. pump fluence for sample FA(2) with deposited Spiro-OMeTAD layer. The ASE threshold is estimated to be $\sim 2.2 \text{ mJ}/\text{cm}^2/\text{pulse}$, almost 3-4 times the ASE threshold for HTM-free sample ($\sim 615 \mu\text{J}/\text{cm}^2/\text{pulse}$)

PL Quenching by Spiro-OMeTAD

The successful realization of ASE in disordered samples like FA(1) and FA(2), where the FAPbBr₃ material is distributed in a mixed phase within a 300 mesoporous TiO₂ network and an additional $\sim 300 \text{ nm}$ perovskite capping layer on top, is in fact very promising. We went one step further, and examined the

effect of the deposition of the HTM layer on the film, which is a necessary step towards electrically injected devices. Spiro-OMeTAD is reported to be a strong PL quenching material, because of the efficient electron transfer across the HTM/perovskite interface [15]–[18]. This is expected to directly result in increasing the threshold pumping energy required to achieve the ASE state. This, however, does not necessarily mean an increase in the ASE threshold carrier density, which is a characteristic of the perovskite layer itself. The increased ASE threshold power will however reflect the efficiency of the electron transfer process across the HTM/perovskite interface. Figure 3.15 shows the results for the SE/ASE emission from sample FA(1) when a layer of Spiro-OMeTAD is deposited on top of the perovskite layer. As expected, the ASE threshold energy density was increased by ~ 3 -4 times, as can be seen in Figure 3.15. The ASE threshold pump fluence increased from $615 \mu\text{J}/\text{cm}^2/\text{pulse}$ for the HTM-free sample, to $\sim 2.2 \text{ mJ}/\text{cm}^2/\text{pulse}$ when Spiro-OMeTAD was deposited.

Investigation of Threshold Carrier Densities under Different Excitation Wavelengths¹

The dependence of ASE on the excitation wavelength was investigated on the FA(2) sample. Amplified spontaneous emission (ASE) studies were carried out on FA(2) using two different excitation wavelengths, 440 nm and 500 nm, which correspond to different optical densities of 0.71 and 0.47, respectively. Figure 3.16a & b shows the SE/ASE spectra under both excitations. Figure 3.16c & d respectively show the behavior of the integrated PL and its FWHM upon increasing the pump density under the two excitation wavelengths. Clearly, the ASE behavior is strongly affected by the excitation wavelength. Different excitation wavelengths, absorbed differently based on the absorption spectrum, indeed result, for the same excitation density, in different free-carrier densities. Therefore, the ASE threshold density depends on the excitation wavelength in a way that follows the absorption spectrum. Under 440 nm excitation, ASE state was achieved with a threshold energy density of $\sim 200 \mu\text{J}/\text{cm}^2$. On the other hand, excitation with 500nm necessitates a higher threshold energy density of $\sim 255 \mu\text{J}/\text{cm}^2$. Excitation with 500 nm also results in a slower differential quantum efficiency, which can be deduced from the lower slope of the PL vs. pump energy density curves in Figure 3.16c. Figure 3.16e shows the behavior of ASE peak position with pump energy density under both excitation wavelengths. Under both excitation wavelengths, the ASE peak redshifts with increasing pump density. Such a behavior can be understood as a result of bandgap renormalization (BGR) in the perovskite crystal under high excitations as mentioned in the introduction of this chapter. Under both excitations, the ASE peak red-shifts by $\sim 1.5 \text{ nm}$ over the whole

¹ This study was carried out on sample FA(2) ~ 8 months after the measurements related to Figure 3.13, with the sample kept in ambient air over this whole period. Although the ASE threshold was relatively higher ($200 \mu\text{J}/\text{cm}^2$ at 440 nm compared to $190 \mu\text{J}/\text{cm}^2$ at less absorbing 450 nm wavelength), and that a surface change could be detected by a fast transient in transmission measurements as discussed below, and thus accounted for, these results really bring about significant optimism regarding the long-range stability of FAPbBr₃ perovskite. (It has to be mentioned also that the transient behavior in the absolute transmittance measurements was completely absent for freshly grown sample, a result that was confirmed after this thesis was submitted, confirming the critical stability issues that have to be considered when perovskite films/devices are studied)

pump energy density range under study, corresponding to a bandgap renormalization by ~ 7 -8 meV, as will be discussed below.

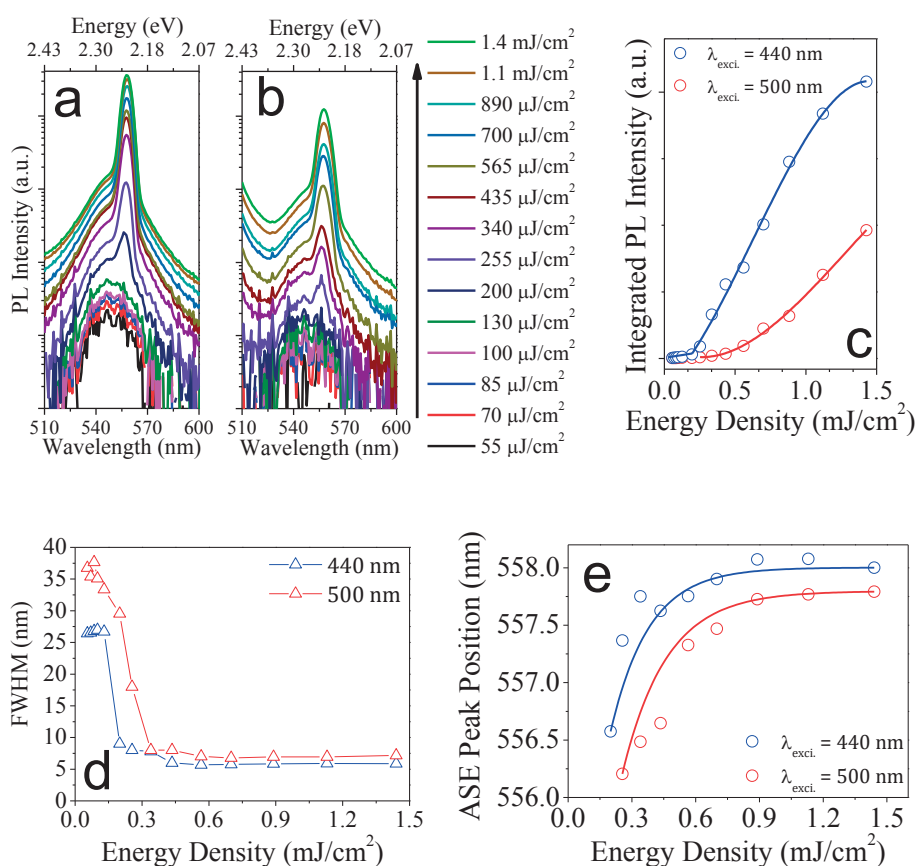


Figure 3.16 Evolution of PL spectra with pulse energy density under (a) 440 nm excitation and (b) 500 nm excitation. (c) Integrated PL intensity vs. pulse energy density under both excitations. (d) FWHM vs. pulse energy density under both excitations. (e) ASE peak position vs. pulse energy density under both excitations.

In order to accurately determine the carrier densities involved in our measurements, the absorption behavior of the perovskite film was further examined under the high-energy density picosecond pulses used to generate the ASE. Absolute transmittance measurements were carried out and a contradictory difference was observed between the two excitation wavelengths. Figure 3.17 shows the absolute transmittance for different pump energies under both excitations. The absolute transmittance under 440 nm (solid blue circles) starts very close to that of 500 nm (solid red circles) before it rapidly increases by ~ 60 -70% (open blue circles). This increase in transmittance under 440nm excitation takes place in few seconds, and it is faster under higher excitation power. After this rapid increase, the absolute transmittance, as well the ASE, remain stable. Unlike under 440nm excitation, the absolute transmittance under 500nm excitation has no such transient behavior. We attribute this increase of absolute transmittance to the existence of a highly absorbing surface layer on the perovskite film that is removed by

the higher energy 440nm pulses. There have been few recent reports about the existence of molecules/complexes that can adsorb either at the TiO₂/perovskite interface or on perovskite surface, which can highly affect the absorption and other optical properties of perovskite films [64]–[66]. Further investigation needs to be carried out to better unravel the origin of this transient behavior.

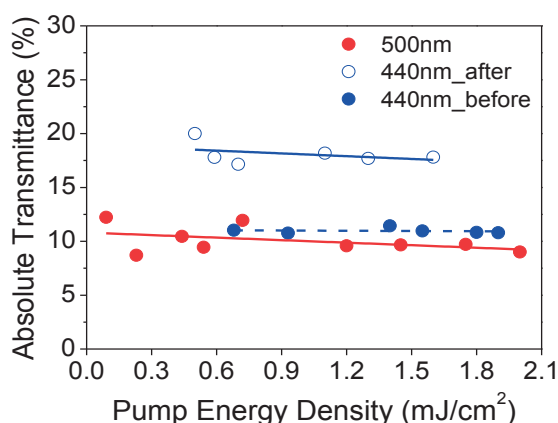


Figure 3.17 Results obtained from absolute transmittance measurements for the FAPbBr₃/ms-TiO₂/FTO sample vs. pump energy densities under 440 nm and 500 nm pump excitations. Under 440 nm excitation, absolute transmittance rapidly increases from the level of blue solid circles to that of blue open ones, as explained in the text.

The ASE power dependence as a function of injected carrier density (n) is depicted in Figure 3.18. The carrier densities are calculated using the absorbance spectrum and film thickness, with the additional absorption of the surface layer under 500 nm excitation taken into account. The transition from SE to ASE takes place with a clear onset at about $\sim 4.5 \times 10^{18} \text{ cm}^{-3}$. This onset density is the same under both excitations. Therefore, the contrasted dependence on energy density under both excitation wavelengths in Figure 3.16c can be explained when both the different optical densities as well as incident photon densities under the two excitations are taken into account. The quantum efficiency under both excitations also behaves differently from Figure 3.16c. Interestingly, both excitations resulted in similar quantum efficiency behaviors, with a slightly reduced slope under 440nm that could be explained by thermal effects due to the higher phonon-assisted thermalization of photocarriers under 440nm.

The bandgap renormalization (BGR) was estimated for the two cases using the spectra shown in Figure 3.16a & b. As mentioned above, BGR is a many-body renormalization effect of the charge carriers in semiconductors. Under high population density conditions, interactions of mobile electrons and holes result in a screening of the Coulomb interaction and so reduce their repulsion, ultimately resulting in a reduction of their average energy, and therefore to a red-shift of the bandgap. Consequently, the magnitude of BGR is inversely proportional to the distance between carriers, and so proportional to $n^{1/3}$. A well-accepted expression for BGR is [28]: $\Delta E_{BGR} = 2 \gamma n^{1/3}$ where γ is called the bandgap renormalization factor.

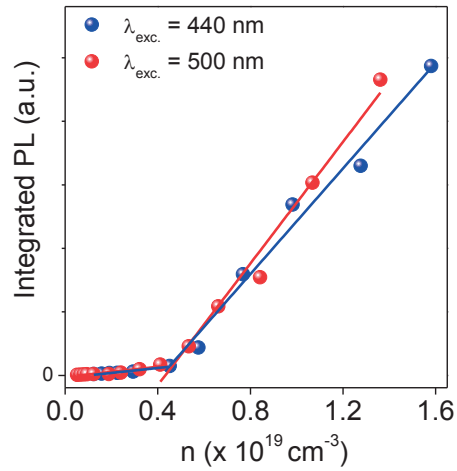


Figure 3.18 Integrated PL versus injected carrier density n . The ASE threshold carrier density is estimated to be the same under 440 nm and 500 nm excitations at $\sim 4.5 \times 10^{18} \text{ cm}^{-3}$. The higher carrier thermalization under 440 nm might be responsible for the slightly lower quantum efficiency.

We inspect now the possibility whether the value of redshift in the ASE emission peak with increasing pump power can be used to estimate the BGR. Indeed, ASE is expected to appear at the maximum of the gain region. In a bulk material with strong excitonic absorption, the position of this maximum as a function of carrier density is almost constant since the absorption exhibits an almost steplike function because of the Sommerfeld enhancement factor (Eq. 3.19 and Eq. 3.20). As a consequence, the ASE peak position as a function of the fluence should essentially reflect the variation of the bandgap as a function of the carrier density. To clarify this behavior, the gain versus pump energy curves need to be generated for FAPbBr₃ under different excitation densities.

To generate the gain spectra, the bandgap and exciton binding energy were first estimated by fitting the absorbance spectrum using Eq. 3.20. The absorption spectrum for FA(2) is re-drawn in Figure 3.19 (blue curve). It can be noticed that the spectrum shows an absorption edge at $\sim 2.38 \text{ eV}$ and a noticeable excitonic peak at $\sim 2.33 \text{ eV}$ below the continuum absorption. An absorption background of ~ 0.3 was subtracted from the absorption spectrum to remove the wavelength independent component of light scattering [67]. The absorption spectrum was re-calculated using Eq. 3.20 where the two terms for excitonic and continuum absorption were considered and convoluted with an appropriate Gaussian line shape function in order to account for line broadening. The best fitting parameters result in a bandgap energy of 2.375 eV , exciton binding energy of 53 meV (comparable to values reported by Ref. [59] and Ref. [60]), and an exciton line broadening of 70 meV , and the calculated spectra are also shown in Figure 3.19.

The gain spectra were then calculated using the values of carrier effective masses (electrons and holes) for FAPbBr₃ in Ref. [68], exciton binding energy of 53 meV calculated above, and the continuum absorbance calculated above with a step function at the bandgap. The gain spectra are plotted in Figure

3.20. At the band edge, the step-like behavior of the gain function becomes more pronounced at higher carrier densities, which results in the ASE peak reflecting the bandgap behavior as well.

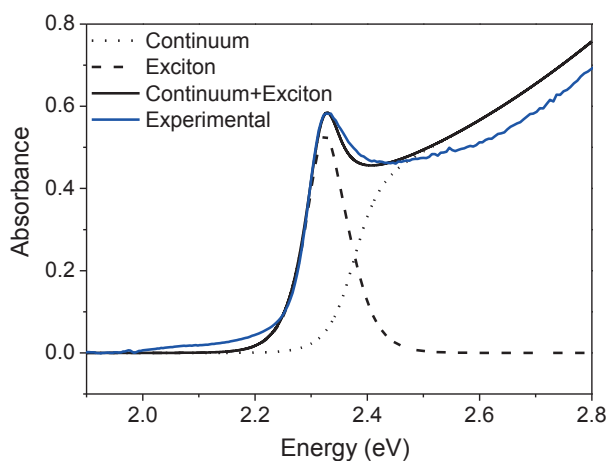


Figure 3.19 Absorbance and PL spectra of the FAPbBr₃ film. The calculated bandgap and exciton absorption spectra along with their summed spectrum are shown in black. Two PL spectra at low and high pump energy densities are shown in green for comparison. The Two PL spectra are not to scale.

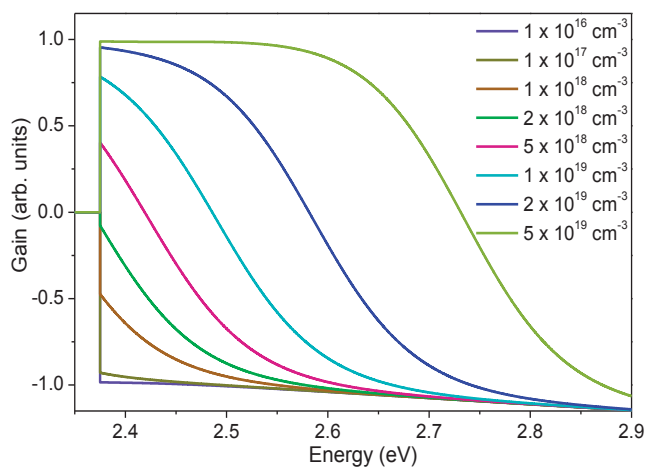


Figure 3.20 Gain vs. energy spectra calculated for different carrier densities. As the carrier density increase, the Sommerfeld enhancement results in a step-like behavior of the gain at the band edge.

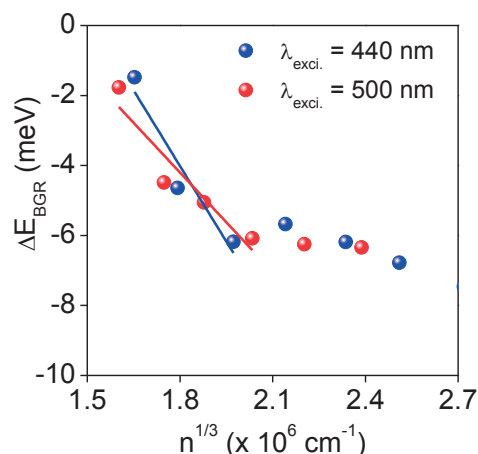


Figure 3.21 BGR versus $n^{1/3}$ (injected) under both 440nm and 500 nm excitations.

Figure 3.21 shows the ΔE_{BGR} vs. $n^{1/3}$ plots for the two excitation wavelengths. BGR, expectedly, increases with increasing carrier density. A maximum BGR value of ~ 7 -8 meV is achieved, corresponding to a maximum red-shift of 1.5 nm at a pump energy density of ~ 0.9 mJ/cm². This small BGR is expected for unconfined photocarriers in a three dimensional structure [31]. BGR saturates at higher pump densities (above ~ 0.9 mJ/cm²). We interpret this as being due to the 3D and cavity-free structure of our sample and the relatively large laser spot size of ~ 2 mm, as a result of which different scattering and other gain loss mechanisms can likely result in a gain saturation condition. Hence, the carrier density does not increase significantly when increasing the fluence. Since the BGR only depends on the carrier density, the energy shift is almost negligible above 0.9 mJ/cm², which can be further hidden by the spectral resolution in our setup of ~ 0.16 nm. Therefore, the bandgap renormalization coefficient was estimated using only the lower carrier density points, and it was estimated to be ~ 5 -7 $\times 10^{-9}$ eV.cm under both excitations. This value is close to values reported for GaAs [28]. Our results indicate that perovskites, despite their currently unresolved stability issues, behave similarly as a standard semiconductor and hence could be further described using the same available formalisms. It has to be mentioned here that the pump energy values in Figure 3.16e and Figure 3.21 corresponds to carrier densities above the ASE threshold, which excludes the possibility of self-absorption to be responsible for the red-shift in the ASE peak.

In conclusion, perovskite solar cells based on high quality FAPbBr₃ films showed a record V_{oc} that is higher than the built-in potential reported for the difference between the work functions of the device contact materials. The solvent environment used during the perovskite growth showed a vital role in achieving this high V_{oc} . Using the same films, ASE was demonstrated for the first time for FAPbBr₃, and ASE threshold carrier density of 2×10^{18} cm⁻³ was obtained.

References

- [1] P. Würfel, *Physics of solar cells: from basic principles to advanced concepts*. John Wiley & Sons, 2009.
- [2] W. Van Roosbroeck and W. Shockley, "Photon-radiative recombination of electrons and holes in germanium," *Phys. Rev.*, vol. 94, no. 6, pp. 1558–1560, 1954.
- [3] "Reference Solar Spectral Irradiance: Air Mass 1.5.," Renewable Resource Data Center, National Renewable Energy Laboratory (NREL), [Online]. Available on the website link: <http://rredc.nrel.gov/solar/spectra/am1.5/> [Accessed: 13-Dec-2016].
- [4] W. Shockley and W. T. Read, "Statistics of the Recombination of Holes and Electrons," *Phys. Rev.*, vol. 87, no. 46, pp. 835–842, 1952.
- [5] E. J. Juarez-Perez, R. S. Sanchez, L. Badia, G. Garcia-Belmonte, Y. S. Kang, I. Mora-Sero, and J. Bisquert, "Photoinduced Giant Dielectric Constant in Lead Halide Perovskite Solar Cells," *J. Phys. Chem. Lett.*, vol. 5, no. 13, pp. 2390–2394, 2014.
- [6] K. Galkowski, A. Mitioglu, A. Miyata, P. Plochocka, O. Portugall, G. E. Eperon, J. T.-W. Wang, T. Stergiopoulos, S. D. Stranks, H. Snaith, and R. J. Nicholas, "Determination of the exciton binding energy and effective masses for methylammonium and formamidinium lead tri-halide perovskite semiconductors," *Energy Environ. Sci.*, vol. 9, no. 3, pp. 962–970, 2016.
- [7] W. Tress, K. Leo, and M. Riede, "Dominating recombination mechanisms in organic solar cells based on ZnPc and C60," *Appl. Phys. Lett.*, vol. 102, no. 16, pp. 163901, 2013.
- [8] W. Tress, *Device Physics of Organic Solar Cells*. PhD Dissertation, Technische Universität Dresden, 2011.
- [9] W. Tress, *Organic Solar Cells* (Springer Series in Materials Science, vol. 208). Springer, 2014.
- [10] N.-G. Park, T. Miyasaka, and M. Grätzel, *Organic-Inorganic Halide Perovskite Photovoltaics*, Chapter 6. Springer, 2016.
- [11] H. M. Ghaithan, S. M. H. Qaid, M. Hezam, J. P. Labis, M. Alduraibi, I. M. Bedja, and A. S. Aldwayyan, "Laser induced photocurrent and photovoltage transient measurements of dye-sensitized solar cells based on TiO₂ nanosheets and TiO₂ nanoparticles," *Electrochim. Acta*, vol. 212, pp. 992–997, 2016.
- [12] A. Miyata, A. Mitioglu, P. Plochocka, O. Portugall, J. T.-W. Wang, S. D. Stranks, H. J. Snaith, and R. J. Nicholas, "Direct measurement of the exciton binding energy and effective masses for charge carriers in organic-inorganic tri-halide perovskites," *Nat. Phys.*, vol. 11, no. 7, pp. 582–587, 2015.
- [13] M. Saba, M. Cadelano, D. Marongiu, F. Chen, V. Sarritsu, N. Sestu, C. Figus, M. Aresti, R. Piras, A. G. Lehmann, C. Cannas, A. Musinu, F. Quochi, A. Mura, and G. Bongiovanni, "Correlated electron-hole plasma in organometal perovskites," *Nat. Commun.*, vol. 5, pp. 5049, 2014.
- [14] M. Saba, F. Quochi, A. Mura, and G. Bongiovanni, "Excited State Properties of Hybrid Perovskites," *Acc. Chem. Res.*, vol. 49, no. 1, pp. 166–173, 2016.
- [15] G. Xing, N. Mathews, S. Sun, S. S. Lim, Y. M. Lam, M. Grätzel, S. Mhaisalkar, and T. C. Sum, "Long-range balanced electron- and hole-transport lengths in organic-inorganic CH₃NH₃PbI₃," *Science*, vol. 342, no. 6156, pp. 344–347, 2013.
- [16] S. D. Stranks, G. E. Eperon, G. Grancini, C. Menelaou, M. J. P. Alcocer, T. Leijtens, L. M. Herz, A. Petrozza, and H. J. Snaith, "Electron-hole diffusion lengths exceeding 1 micrometer in an organometal trihalide perovskite absorber," *Science*, vol. 342, no. 6156, pp. 341–344, 2013.
- [17] G. Xing, N. Mathews, S. S. Lim, N. Yantara, X. Liu, D. Sabba, M. Grätzel, S. Mhaisalkar, and T. C. Sum, "Low-temperature solution-processed wavelength-tunable perovskites for lasing," *Nat. Mater.*, vol. 13, no. 5, pp. 476–480, 2014.

- [18] H.-S. Kim, C.-R. Lee, J.-H. Im, K.-B. Lee, T. Moehl, A. Marchioro, S.-J. Moon, R. Humphry-Baker, J.-H. Yum, J. E. Moser, M. Graetzel, and N.-G. Park, "Lead Iodide Perovskite Sensitized All-Solid-State Submicron Thin Film Mesoscopic Solar Cell with Efficiency Exceeding 9%," *Sci. Rep.*, vol. 2, pp. 583–585, 2012.
- [19] G. Xing, B. Wu, S. Chen, J. Chua, N. Yantara, S. Mhaisalkar, N. Mathews, and T. C. Sum, "Interfacial Electron Transfer Barrier at Compact TiO₂/CH₃NH₃PbI₃ Heterojunction," *Small*, vol. 11, no. 29, pp. 3606–3613, 2015.
- [20] Q. Chen, H. Zhou, T.-B. Song, S. Luo, Z. Hong, H.-S. Duan, L. Dou, Y. Liu, and Y. Yang, "Controllable self-induced passivation of hybrid lead iodide perovskites toward high performance solar cells," *Nano Lett.*, vol. 14, no. 7, pp. 4158–4163, 2014.
- [21] W. Peng, L. Wang, B. Murali, K. T. Ho, A. Bera, N. Cho, C. F. Kang, V. M. Burlakov, J. Pan, L. Sinatra, C. Ma, W. Xu, D. Shi, E. Alarousu, A. Goriely, J. H. He, O. F. Mohammed, T. Wu, and O. M. Bakr, "Solution-Grown Monocrystalline Hybrid Perovskite Films for Hole-Transporter-Free Solar Cells," *Adv. Mater.*, vol. 28, no. 17, pp. 3383–3390, 2016.
- [22] T. C. Sum, N. Mathews, G. Xing, S. S. Lim, W. K. Chong, D. Giovanni, and H. A. Dewi, "Spectral Features and Charge Dynamics of Lead Halide Perovskites: Origins and Interpretations," *Acc. Chem. Res.*, vol. 49, no. 2, pp. 294–302, 2016.
- [23] W. Rehman, R. I. Milot, G. E. Eperon, C. Wehrenfennig, J. L. Boland, H. J. Snaith, M. B. Johnston, and L. M. Herz, "Charge-Carrier Dynamics and Mobilities in Formamidinium Lead Mixed-Halide Perovskites," *Adv. Mater.*, vol. 27, no. 48, pp. 7938–7944, 2015.
- [24] E. Rosencher and B. Vinter, *Optoelectronics*. Cambridge University Press, 2002.
- [25] U. Rau, "Reciprocity relation between photovoltaic quantum efficiency and electroluminescent emission of solar cells," *Phys. Rev. B*, vol. 76, no. 8, pp. 085303, 2007.
- [26] M. G. A. Bernard and G. Duraffourg, "Laser Conditions in Semiconductors," *Phys. status solidi*, vol. 1, no. 7, pp. 699–703, 1961.
- [27] T. Suhara, *Semiconductor laser fundamentals*. CRC Press, 2004.
- [28] Y. Yang, D. P. Ostrowski, R. M. France, K. Zhu, J. van de Lagemaat, J. M. Luther, and M. C. Beard, "Observation of a hot-phonon bottleneck in lead-iodide perovskites," *Nat. Photonics*, vol. 10, pp. 53–59, 2016.
- [29] N. Sestu, M. Cadelano, V. Sarritzu, F. P. Chen, D. Marongiu, R. Piras, M. Mainas, F. Quochi, M. Saba, A. Mura, and G. Bongiovanni, "Absorption F-Sum Rule for the Exciton Binding Energy in Methylammonium Lead Halide Perovskites," *J. Phys. Chem. Lett.*, vol. 6, no. 22, pp. 4566–4572, 2015.
- [30] W. B. Joyce and R. W. Dixon, "Analytic approximations for the Fermi energy of an ideal Fermi gas," *Appl. Phys. Lett.*, vol. 31, no. 5, pp. 354–356, 1977.
- [31] G. Trankle, H. Leier, A. Forchel, H. Haug, C. Ell, and G. Weimann, "Dimensionality dependence of the band-gap renormalization in two- and three-dimensional electron-hole plasmas in GaAs," *Phys. Rev. Lett.*, vol. 58, no. 4, pp. 419–422, 1987.
- [32] M. Shahmohammadi, G. Jacopin, G. Rossbach, J. Levrat, E. Feltin, J.-F. Carlin, J.-D. Ganière, R. Butté, N. Grandjean, and B. Deveaud, "Biexcitonic molecules survive excitons at the Mott transition," *Nat. Commun.*, vol. 5, pp. 5251, 2014.
- [33] N. Arora, M. I. Dar, M. Hezam, W. Tress, G. Jacopin, T. Moehl, P. Gao, A. S. Aldwayyan, B. Deveaud, M. Grätzel, and M. K. Nazeeruddin, "Photovoltaic and Amplified Spontaneous Emission Studies of High-Quality Formamidinium Lead Bromide Perovskite Films," *Adv. Funct. Mater.*, vol. 26, no. 17, pp. 2846–2854, 2016.
- [34] J. W. Lee, H. S. Kim, and N. G. Park, "Lewis Acid-Base Adduct Approach for High Efficiency Perovskite Solar Cells," *Acc. Chem. Res.*, vol. 49, no. 2, pp. 311–319, 2016.

- [35] H. Miyamae, Y. Numahata, and M. Nagata, "The crystal structure of lead(II) iodide-dimethylsulphoxide(1/2), $\text{PbI}_2(\text{dms})_2$," *Chem. Lett.*, vol. 9, no. 6, pp. 663–664, 1980.
- [36] A. Wakamiya, M. Endo, T. Sasamori, N. Tokitoh, Y. Ogomi, S. Hayase, and Y. Murata, "Reproducible Fabrication of Efficient Perovskite-based Solar Cells: X-ray Crystallographic Studies on the Formation of $\text{CH}_3\text{NH}_3\text{PbI}_3$ Layers," *Chem. Lett.*, vol. 43, pp. 711–713, 2014.
- [37] N. Arora, M. I. Dar, M. Abdi-Jalebi, F. Giordano, N. Pellet, G. Jacopin, R. H. Friend, S. M. Zakeeruddin and M. Grätzel, "Intrinsic and Extrinsic Stability of Formamidinium Lead Bromide Perovskite Solar Cells Yielding High Photovoltage," *Nano Lett.*, vol. 16, no. 11, pp. 7155–7162, 2016.
- [38] M. A. Green, A. Ho-Baillie, and H. J. Snaith, "The emergence of perovskite solar cells," *Nat. Photonics*, vol. 8, no. 7, pp. 506–514, 2014.
- [39] M. A. Green, J. Zhao, A. Wang, P. J. Reece, and M. Gal, "Efficient silicon light-emitting diodes," *Nature*, vol. 412, no. 6849, pp. 805–808, 2001.
- [40] S.-Y. Kim, W.-I. Jeong, C. Mayr, Y.-S. Park, K.-H. Kim, J.-H. Lee, C.-K. Moon, W. Brütting, and J.-J. Kim, "Organic light-emitting diodes with 30% external quantum efficiency based on a horizontally oriented emitter," *Adv. Funct. Mater.*, vol. 23, no. 31, pp. 3896–3900, 2013.
- [41] K. Kano, *Semiconductor devices*, vol. 3. Prentice Hall, 1998.
- [42] T. M. Brenner, D. A. Egger, A. M. Rappe, L. Kronik, G. Hodes, and D. Cahen, "Are Mobilities in Hybrid Organic-Inorganic Halide Perovskites Actually 'High'?", *Journal of Physical Chemistry Letters*, vol. 6, no. 23, pp. 4754–4757, 2015.
- [43] M. F. Aygueler, M. D. Weber, B. M. D. Puscher, D. D. Medina, P. Docampo, and R. D. Costa, "Light-Emitting Electrochemical Cells Based on Hybrid Lead Halide Perovskite Nanoparticles," *J. Phys. Chem. C*, vol. 119, no. 21, pp. 12047–12054, 2015.
- [44] A. Perumal, S. Shendre, M. Li, Y. K. E. Tay, V. K. Sharma, S. Chen, Z. Wei, Q. Liu, Y. Gao, P. J. S. Buenconsejo, S. T. Tan, C. L. Gan, Q. Xiong, T. C. Sum and H. V. Demir, "High brightness formamidinium lead bromide perovskite nanocrystal light emitting devices," *Sci. Rep.*, vol. 6, pp. 36733, 2016.
- [45] L. Meng, E.-P. Yao, Z. Hong, H. Chen, P. Sun, Z. Yang, G. Li, and Y. Yang, "Pure Formamidinium-Based Perovskite Light-Emitting Diodes with High Efficiency and Low Driving Voltage," *Adv. Mater.*, vol. 29, no. 4, pp. 1603826, 2017.
- [46] Q. Zhang, S. T. Ha, X. Liu, T. C. Sum, and Q. Xiong, "Room-temperature near-infrared high-Q perovskite whispering-gallery planar nanolasers," *Nano Lett.*, vol. 14, no. 10, pp. 5995–6001, 2014.
- [47] B. R. Sutherland, S. Hoogland, M. M. Adachi, C. T. O. Wong, and E. H. Sargent, "Conformal organohalide perovskites enable lasing on spherical resonators," *ACS Nano*, vol. 8, no. 10, pp. 10947–10952, 2014.
- [48] F. Deschler, M. Price, S. Pathak, L. E. Klintberg, D.-D. Jarausch, R. Higler, S. Hüttner, T. Leijtens, S. D. Stranks, H. J. Snaith, M. Atatüre, R. T. Phillips, and R. H. Friend, "High photoluminescence efficiency and optically pumped lasing in solution-processed mixed halide perovskite semiconductors," *J. Phys. Chem. Lett.*, vol. 5, no. 8, pp. 1421–1426, 2014.
- [49] T. S. Kao, Y.-H. Chou, C.-H. Chou, F.-C. Chen, and T.-C. Lu, "Lasing behaviors upon phase transition in solution processed perovskite thin films," *Appl. Phys. Lett.*, vol. 105, no. 23, pp. 231108, 2014.
- [50] R. Dhanker, A. N. Brigeman, A. V. Larsen, R. J. Stewart, J. B. Asbury, and N. C. Giebink, "Random lasing in organo-lead halide perovskite microcrystal networks," *Appl. Phys. Lett.*, vol. 105, pp. 151112, 2014.
- [51] T. Kondo, T. Azuma, T. Yuasa, and R. Ito, "Biexciton lasing in the layered perovskite-type material $(\text{C}_6\text{H}_{13}\text{NH}_3)_2\text{PbI}_4$," *Solid State Commun.*, vol. 105, no. 4, pp. 253–255, 1998.

- [52] M. Era, S. Morimoto, T. Tsutsui, and S. Saito, "Organic-inorganic heterostructure electroluminescent device using a layered perovskite semiconductor (C₆H₅C₂H₄NH₃)₂PbI₄," *Appl. Phys. Lett.*, vol. 65, no. 6, pp. 676-678, 1994.
- [53] X. Hong, T. Ishihara, and A. V. Nurmikko, "Photoconductivity and electroluminescence in lead iodide based natural quantum well structures," *Solid State Commun.*, vol. 84, no. 6, pp. 657-661, 1992.
- [54] J. Ding, M. Hagerott, T. Ishihara, H. Jeon, and A. V. Nurmikko, "(Zn,Cd)Se/ZnSe quantum-well lasers: Excitonic gain in an inhomogeneously broadened quasi-two-dimensional system," *Phys. Rev. B*, vol. 47, no. 16, pp. 10528-10542, 1993.
- [55] M. I. Dar, G. Jacopin, S. Meloni, A. Mattoni, N. Arora, A. Boziki, S. M. Zakeeruddin, U. Rothlisberger, and M. Grätzel, "Origin of unusual bandgap shift and dual emission in organic-inorganic lead halide perovskites," *Sci. Adv.*, vol. 2, no. 10, pp. e1601156, 2016.
- [56] C. Wehrenfennig, M. Liu, H. J. Snaith, M. B. Johnston, and L. M. Herz, "Homogeneous Emission Line Broadening in the Organo Lead Halide Perovskite CH₃NH₃PbI_{3-x}Cl_x," *J. Phys. Chem. Lett.*, vol. 5, no. 8, pp. 1300-1306, 2014.
- [57] K. Wu, A. Bera, C. Ma, Y. Du, Y. Yang, L. Li, and T. Wu, "Temperature-dependent excitonic photoluminescence of hybrid organometal halide perovskite films," *Phys. Chem. Chem. Phys.*, vol. 16, no. 41, pp. 22476-22481, 2014.
- [58] H. Kunugita, T. Hashimoto, Y. Kiyota, Y. Udagawa, Y. Takeoka, Y. Nakamura, J. Sano, T. Matsushita, T. Kondo, T. Miyasaka, K. Ema, "Excitonic Feature in Hybrid Perovskite CH₃NH₃PbBr₃ single crystals," *Chem. Lett.*, vol. 44, pp. 852-854, 2015.
- [59] N. Kitazawa, Y. Watanabe, and Y. Nakamura, "Optical properties of CH₃NH₃PbX₃ (X = halogen) and their mixed-halide crystals," *J. Mater. Sci.*, vol. 37, no. 17, pp. 3585-3587, 2002.
- [60] V. D'Innocenzo, G. Grancini, M. J. P. Alcocer, A. R. S. Kandada, S. D. Stranks, M. M. Lee, G. Lanzani, H. J. Snaith, and A. Petrozza, "Excitons versus free charges in organo-lead tri-halide perovskites," *Nat. Commun.*, vol. 5, pp. 3586, 2014.
- [61] D. Priante, I. Dursun, M. S. Alias, D. Shi, V. A. Melnikov, T. K. Ng, O. F. Mohammed, O. M. Bakr, and B. S. Ooi, "The recombination mechanisms leading to amplified spontaneous emission at the true-green wavelength in CH₃NH₃PbBr₃ perovskites," *Appl. Phys. Lett.*, vol. 106, no. 8, pp. 81902, 2015.
- [62] D. Shi, V. Adinolfi, R. Comin, M. Yuan, E. Alarousu, A. Buin, Y. Chen, S. Hoogland, A. Rothenberger, K. Katsiev, Y. Losovyj, X. Zhang, P. A. Dowben, O. F. Mohammed, E. H. Sargent, and O. M. Bakr, "Low trap-state density and long carrier diffusion in organolead trihalide perovskite single crystals," *Science*, vol. 347, no. 6221, pp. 519-522, 2015.
- [63] K. Chen, A. J. Barker, F. L. C. Morgan, J. E. Halpert, and J. M. Hodgkiss, "Effect of carrier thermalization dynamics on light emission and amplification in organometal halide perovskites," *J. Phys. Chem. Lett.*, vol. 6, no. 1, pp. 153-158, 2015.
- [64] T. Leijtens, G. E. Eperon, S. Pathak, A. Abate, M. M. Lee, and H. J. Snaith, "Overcoming ultraviolet light instability of sensitized TiO₂ with meso-superstructured organometal tri-halide perovskite solar cells," *Nat. Commun.*, vol. 4, pp. 2885, 2013.
- [65] T. Ma, D. Tadaki, M. Sakuraba, S. Sato, A. Hirano-Iwata, and M. Niwano, "Effects of interfacial chemical states on the performance of perovskite solar cells," *J. Mater. Chem. A*, vol. 4, no. 12, pp. 4392-4397, 2016.
- [66] M. Shirayama, M. Kato, T. Miyadera, T. Sugita, T. Fujiseki, S. Hara, H. Kadowaki, D. Murata, M. Chikamatsu, and H. Fujiwara, "Degradation mechanism of CH₃NH₃PbI₃ perovskite materials upon exposure to humid air," *J. Appl. Phys.*, vol. 119, no. 11, p. 115501, 2016.
- [67] Y. Tian and I. G. Scheblykin, "Artifacts in absorption measurements of organometal halide perovskite materials: What are the real spectra?," *Journal of Physical Chemistry Letters*, vol. 6, no. 13, pp. 3466-3470, 2015.

- [68] N. K. Kumawat, M. N. Tripathi, U. V Waghmare, and D. Kabra, "Structural, Optical and Electronic Properties of Wide Bandgap Perovskites: Experimental & Theoretical Investigation," *J. Phys. Chem. A*, vol. 120, no. 22, pp. 3917-3923, 2016.

Chapter 4

Time-resolved Photoluminescence Studies on MAPbI₃/Metal Oxide Interfaces

This chapter investigates the UV-induced degradation of MAPbI₃ using time-resolved and time-integrated photoluminescence. The role of interface metal oxide materials (e.g. TiO₂, Al₂O₃) in the degradation process is also investigated. Importantly, we show that UV degradation, under 280 nm picosecond pulses, is not only associated with the presence of TiO₂ catalytic surface or oxygen in the ambient as reported by different previously published works. Rather, a fast UV damage is observed for a pristine MAPbI₃ film under vacuum, indicating an intrinsic UV degradation mechanism. This degradation resulted in the creation of fast picosecond PL decay channels, attributed to UV-created traps, compared to long nanosecond PL decays under blue 425 nm excitation. Starting from this finding, low temperature and time resolved PL measurements are carried out and studied. Strikingly, the UV damage was completely switched off below ~ 230 K, accompanied with long nanosecond PL dynamics again. The possible degradation mechanisms proposed in the available literature are examined for our results. Bond dissociation in thermally liberated MA ions is suggested to make the primary step in UV degradation, after which other mechanisms, with no UV energy threshold, might also contribute to the degradation process.

The main body of this work is expected to result in the following publication:

Hezam, M., Jacopin, G., Qin, P., Aldwayyan, A., Nazeeruddin, M. K., Deveaud, B. Elucidating UV-degradation Mechanisms in Methylammonium Lead Halide Perovskite. (to be submitted)

4.1 Introduction

As briefly discussed in Chapter 1, perovskite solar cells emerged initially from dye-sensitized solar cells (DSSCs), where dye molecules, adsorbed on a mesoporous TiO_2 scaffold with high surface area, were intended to be replaced by perovskite quantum dots (QDs) with tunable and higher absorption coefficients. Replacement of dyes with semiconductor QDs have, in general, been a hardly succeeding field [1]–[4], and the first research efforts on perovskite solar cells, carried out between ~2006-2011 by the group of T. Miyasaka and the group of N-G Park [5]–[10], were within the series of trials in this field. In a typical DSSC, a dye molecule absorbs the solar photon, and the excited electron is immediately injected (within a femtosecond time scale [11]) into the conduction band of an underlying mesoporous TiO_2 (ms- TiO_2) layer. Subsequently, the ms- TiO_2 layer plays the role of as an electron transport material (ETM) to the photo-anode. Ions of I^-/I_3^- in the liquid electrolyte surrounding the dye/ TiO_2 network serve as a hole-transport material (HTM) and thus complete the electric circuit. Although it has been already established that, unlike in DSSCs, the ms- TiO_2 (or metal oxides in general, e.g. ZnO , SnO_2) is not a necessary layer in perovskite solar cells [12], [13], perovskite solar cells with mesoporous TiO_2 under-layers are still among the best performing devices [14]–[18].

In fact, the mesoporous under-layer showed to be important for better film uniformity, and for reduced grain size of the perovskite film. These properties are expected, in mesoporous perovskite solar cells, to be responsible for the reduction of J-V hysteresis, compared to corresponding flat devices [16], [19]. Beyond that, there has been some debate about charge separation efficiency across the perovskite/ TiO_2 interface. First, a perovskite solar cell device with ms- Al_2O_3 , which has a CB level higher than that of the MAPbI_3 perovskite preventing electron transfer, was early demonstrated in 2012 [12] with a record efficiency of 11%, and higher efficiencies later on [13]. In the same period of time, charge separation across the $\text{MAPbI}_3/\text{TiO}_2$ interface had been debatable by some contradicting results [12], [14].

Besides the debate on $\text{MAPbI}_3/\text{TiO}_2$ charge separation efficiency, the poor stability of the $\text{MAPbI}_3/\text{TiO}_2$ interface under different environmental conditions (e.g. moisture, temperature, air (oxygen), UV light) has been reported by many people [20]–[26]. In many of these studies, UV is reported to catalyze many deteriorating processes at the $\text{MAPbI}_3/\text{TiO}_2$ interface [25], [27]–[31]. The study in this chapter goes along these lines and uses time-resolved photoluminescence (TRPL) to investigate both UV-induced damage and charge separation at the $\text{MAPbI}_3/\text{TiO}_2$ interface. In short, we show that the UV-induced degradation is not only associated with UV-induced damage by photoexcited TiO_2 , and that an intrinsic UV-induced damage in the MAPbI_3 perovskite bulk also exists. We attribute this damage to UV-induced bond dissociation in the MA cation, which is weakly bound to the inorganic PbI_6^- framework at room temperature. Results from temperature-dependent TRPL and time integrated photoluminescence (TIPL) were performed in a complementary fashion, and an activation energy of ~ 20 meV was estimated for this process, in agreement with the reported thermal energies reported for the liberation of MA ion movements in the MAPbI_3 structure.

4.2 Description of Samples

Two widely accepted methods are currently employed in the spin-coating deposition of MAPbI₃ on mesoporous metal oxide layers. In the first method, which we call single-step deposition [14], a desired ratio of PbI₂ and MAI is first dissolved in a specific solvent, commonly γ -butyrolactone (GBL). The solution is then simply spin-coated on the mesoporous layer, and the resulting film is heated for 15-30 minutes at ~ 100 °C to prompt the perovskite crystallization process. In the second method, called the sequential deposition [15], a solution of PbI₂ only is first prepared and deposited on the mesoporous layer. The resulting film is sequentially soaked in a MAI solution, where the crystallization process immediately starts. Figure 4.1 shows a schematic that allows to picture the difference between the two methods. There have been many reports on the different outcomes when using the two methods [32]–[34], and both have been widely implemented with different perovskite materials [14]–[18]. As can be anticipated from Figure 4.1, the sequential method is expected to result in a higher concentration of traps due to the low temperature growth and the possibility of unreacted PbI₂ during the MAI soaking process.

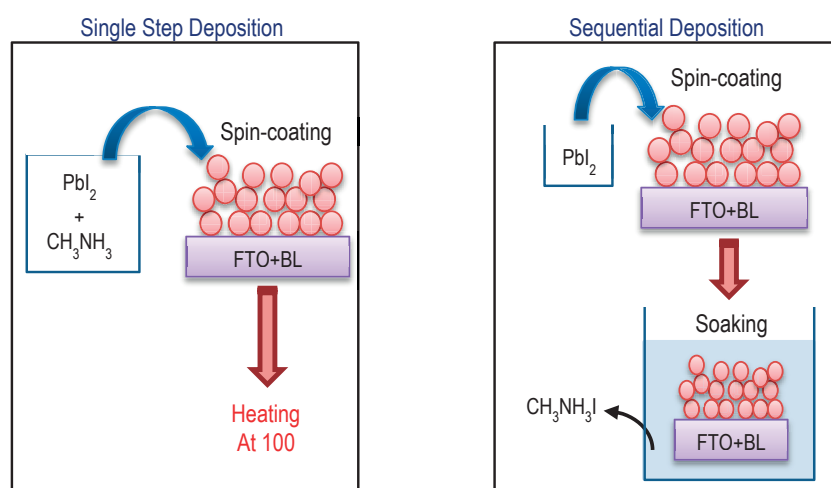


Figure 4.1 Schematic diagrams showing steps of CH₃NH₃PbI₃ spin-coating deposition using the single step deposition (left) and the sequential deposition (right) methods

For comparison, Figure 4.2 shows TRPL for MAPbI₃ deposited on Al₂O₃ scaffold using both techniques. As expected, the single-step deposition results in a much slower PL decay compared to sequential deposition. The sample deposited using sequential deposition shows a multi-exponential sub-nanosecond PL decay, whereas the sample deposited using the single step deposition has a much longer PL decay, whose time constant(s) is larger than the measurement time window of the streak camera (~ 1.5 ns). Therefore, as this study is concerned with the measurements of PL decay dynamics when UV-induced defects are additionally created, which happen to occur with similar time scale of PL decay time constants of sequentially deposited samples (as will be seen below), single-step deposition was adopted for the UV degradation studies in this chapter.

All samples were prepared by Dr. Peng Qin in collaboration with the group of Prof. Nazeeruddin, EPFL. The single-step method was used to spin-coat MAPbI₃ on mesoporous TiO₂ (sample MAPbI₃/ms-TiO₂) and mesoporous Al₂O₃ (sample MAPbI₃/ms-Al₂O₃). For comparison, a thin film of MAPbI₃ was also spin-coated on a flat glass substrate (sample MAPbI₃_Film). All samples were prepared with a total MAPbI₃ weight concentration of 40% in the GBL solvent. The sequential sample, used for the TRPL comparison in Figure 4.2, was prepared using the same molarity of PbI₂ and MAI required for 40% concentration, but with the sequential method adopted during deposition. Further details on the preparation procedure can be found elsewhere [35], [36].

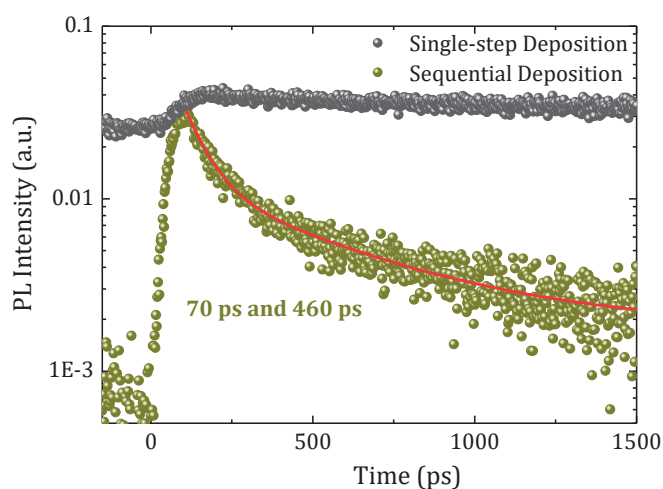


Figure 4.2 Comparison between TRPL decays for MAPbI₃ deposited on Al₂O₃ scaffold using the single-step and sequential deposition methods. The samples were excited using 425 nm pulses and laser power of 200 μ W.

Temperature-dependent TIPL and TRPL measurements were carried out under vacuum ($\sim 10^{-5}$ mbar) at different temperatures using both UV excitation (280 nm pulses, photon energy = 4.4 eV) and blue excitation (425 nm pulses, photon energy = 2.9 eV). The laser power was kept at ~ 200 μ W, which corresponds to a photon flux density of $\sim 10^{11}$ photons/cm² per pulse.

4.3 Studies on UV-induced damage at MAPbI₃/metal oxide interface

4.3.1 Room Temperature Measurements

Figure 4.3a shows the time-integrated PL of samples MAPbI₃/ms-TiO₂, MAPbI₃/ms-Al₂O₃ and MAPbI₃_Film at room temperature when excited with 280 nm UV pulses. All samples showed broad spontaneous emission peaks with FWHM broadening of ~ 90 meV. For all samples, however, a fast degradation of the TIPL signal, over seconds, was observed. Figure 4.3b shows a typical UV-induced degradation of PL intensity over time for the MAPbI₃_Film sample under UV excitation. Three important

points can be concluded from Figure 4.3b. First, this result unambiguously confirms that UV-induced degradation is not only associated with UV-induced damage by photoexcited TiO₂, as previously reported by some publications [25], [27], [28], and that an intrinsic UV-induced damage also exists. Second, the UV-induced damage is irreversible as can be seen in the figure, which indicates the creation of non-radiative defect traps in the material. Third, despite the fast damage, a residual PL signal of $\sim 5\%$ continues to be present for a long period of time. This, fortunately, allowed us to carry out time-resolved PL measurements using the streak camera, and the results are shown in Figure 4.4. In all TRPL measurements below, we waited for ~ 5 minutes of continuous UV excitation before the PL signal for the streak images was accumulated. Therefore, the TRPL dynamics presented below represent the state of the material after UV-induced traps are already created.

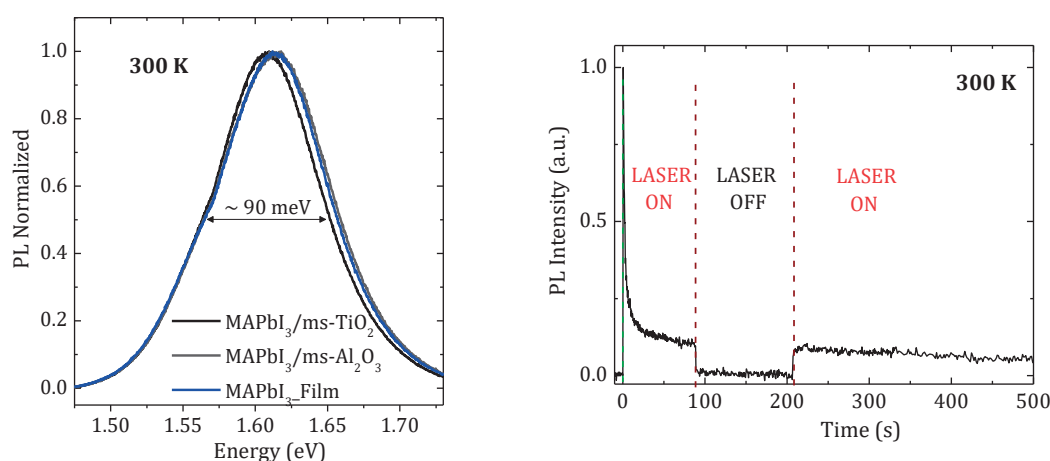


Figure 4.3 (a) TIPL of prepared samples at 300 K. (b) PL intensity degradation with time induced by the UV excitation for MAPbI₃_Film at 300 K.

Figure 4.4a shows the TRPL dynamics when the samples are excited with UV pulses, while Figure 4.4b shows the TRPL dynamics when blue 425 nm pulses are used for excitation (where the damage was completely absent). The high contrast between the two excitations can be clearly noticed. In Figure 4.4a, all samples showed fast sub-nanosecond decays, which can be attributed to the traps created by UV degradation. PL decay curves could be fitted for all samples using a minimum of two exponential decay functions. The PL decay of MAPbI₃/ms-TiO₂ is the fastest, where the exponential fitting gives decay time constants of 15 ps and 290 ps. The PL decay of MAPbI₃/ms-Al₂O₃ showed a relatively slower dynamics, with fitting time constants of 30 ps and 280 ns. In both mesoporous samples, the faster decay component weights $> 95\%$ in the fitting function. PL decay of the thin film sample MAPbI₃_Film showed a noticeably slower decay with time constants of 105 ps and 790ps, with $\sim 50\%$ weight for each decay component. These results indicate clearly the existence of different surface-based UV-degradation mechanisms, whose created defects are responsible for the faster decay in the mesoporous samples. These UV-induced surface

traps are clearly more efficient, as non-radiative recombination centers, than traps created by the intrinsic bulk UV-degradation, which are also confirmed in our results.

Interestingly, under 425 nm excitation (Figure 4.4b), all samples showed similar and much longer PL decays. Quantitative figures could not be obtained for the PL decay time constants as the exponential fitting –although possible– can never be conclusive, since the decay time is longer than the measurement time interval of ~ 1.5 ns [37]. Compared to PL decays under UV excitation, the PL decays measured here are also associated with an appreciable relative residual background before the PL rising starts, further confirming that the PL decay is longer than the measurement time window. We attribute the different residual backgrounds between the different samples, under 425 nm excitation, to the different MAPbI₃ loading on the ms-TiO₂, ms-Al₂O₃ and glass substrates. As no PL damage is observed under 425 nm, under such low photon flux density, we attribute the long PL decays in Figure 4.4b to the SRH non-radiative recombination of traps developed during the film deposition. This way, we can conclude that the short PL decays under UV excitation (Figure 4.4a) is mainly dominated by traps developed by UV degradation.

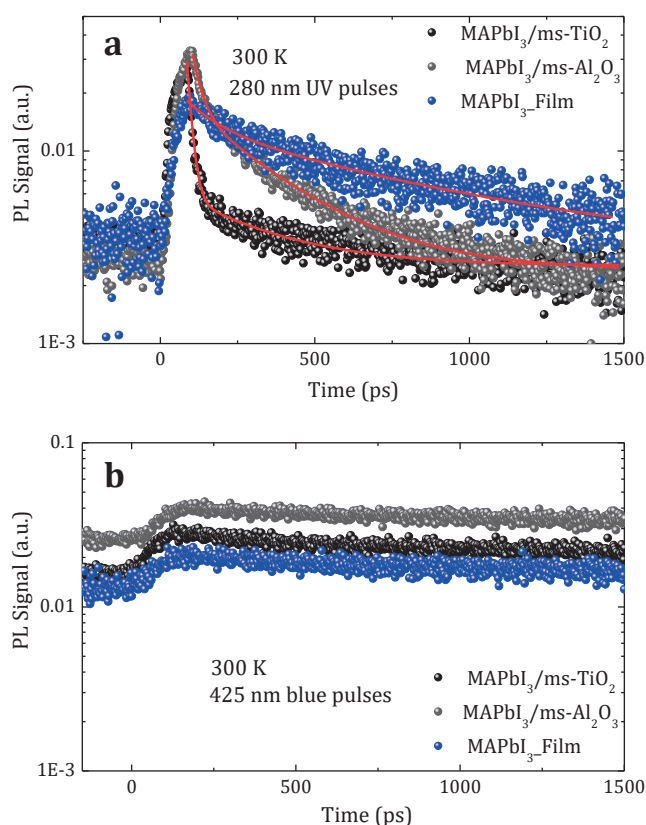


Figure 4.4 TRPL results for all samples under excitation of (a) 280 nm UV pulses and (b) 425 nm blue pulses.

UV degradation in MAPbI₃ has been studied by various groups, and the actual mechanism of UV degradation has been a highly debated topic [25], [27], [28]. In our work, we have at least three different UV degradation processes: bulk degradation, degradation at the MAPbI₃/ms-TiO₂, and degradation at the

MAPbI₃/ms-Al₂O₃ interface. Among these, UV-created traps at the MAPbI₃/ms-TiO₂ interface are clearly the most efficient, reflected by the fastest PL decay dynamics in Figure 4.4a. Indeed, many recent papers have reported this TiO₂/MAPbI₃ UV damage to be the main UV degradation mechanism [25], [27], [28]. However, direct UV-induced damage in the MAPbI₃ bulk is clearly demonstrated in our work, up to our best knowledge, for the first time. In the following section, the few possible degradation mechanisms proposed in the available literature will be evaluated. After this discussion, we propose the direct dissociation of molecular bonds in the MA ions as the primary step in UV degradation, which will be subsequently tested using low temperature measurements.

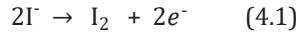
UV Degradation at the TiO₂/MAPbI₃ interface

UV-induced degradation induced at the TiO₂/MAPbI₃ interface was first explained by Leijtens et al [25] to result from the adsorption/desorption of oxygen on the TiO₂ surface. In fact, oxygen adsorption/desorption on TiO₂ surfaces is a well-studied problem [38], [39]. Ti has a coordination of Ti⁴⁺ in TiO₂. However, when an oxygen vacancy is developed at the surface, e.g. during sample preparation, Ti becomes under-coordinated as Ti³⁺, resulting in an active surface site. Oxygen molecules in the ambient are reported to adsorb very efficiently on those oxygen vacancy surface sites. Hence, adsorption will directly depend on the density of oxygen vacancies (defects) on the surface, which can be high for our samples, because, first, they are solution-processed and, second, mesoporous (i.e. they have a high surface area). It has been shown by Lu et al [38] that the sticking probability of O₂ molecule to a vacancy site, or equivalently to an under-coordinated Ti³⁺ site, is near unity. The Ti³⁺ states produce mid-gap energy levels, which lie at ~ 0.7-1 eV below the CB of TiO₂ [40]. At very low temperatures (~ 100-200 K), O₂ keeps its molecular identity (as a superoxide O₂⁻) at the vacancy site making a (V_o-O₂⁻) complex. This enhances the band-bending at the surface. At higher temperature (at ~ 250 K), the molecular identity is still there (most likely as a peroxide O₂²⁻) but with a different configuration and stronger binding to the surface. The doubly charged peroxide will further enhance the band bending property at the surface. Only at temperatures higher than 400 K, all molecular oxygen is dissociated into atomic oxygen filling all the vacancy sites and passivating the traps [38].

The photo desorption of oxygen molecules can happen only if the energy of the excitation photon is greater than the bandgap of TiO₂ (~ 3.1 eV). That means, the photon is first absorbed by TiO₂, and the excited hole is captured by the surface oxygen molecule, which consequently desorbs from the surface. Therefore, this widely accepted scenario [25], [31], [40]–[42] assumes a TiO₂-mediated oxygen desorption process, which subsequently results in an active trap site at the TiO₂ surface, combined with an excited electron in the CB. In a typical perovskite solar cell device, those excited electrons can recombine with holes in the HTM layer reducing the generated photocurrent, in agreement with reported results [43]. This scenario however suggests this process to be more efficient under vacuum, and to be reversible with changing the oxygen partial pressure, i.e. a device poorly performing under deficient oxygen conditions should recover performance when it is placed back in air. Although this reversibility was shown, by the

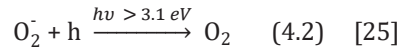
same group, to exist in solid state dye-sensitized solar cells devices employing ms-TiO₂ layers [40], [44], results on perovskite solar cells are not presented. Also, in our work at 300 K, an irreversible damage was observed, which cannot be explained by this scenario alone.

Another possible scenario for the UV-induced damage, suggested by Ito et al [28], starts from the highly mobile iodide ions in the perovskite lattice, which can be accelerated by the potential developed by light illumination, resulting in strong ion migrations as explained in Chapter 1. TiO₂ has a strong ability to extract electrons from iodide ions, a well-known fact from the field of dye-sensitized solar cells [45]. The reduction of iodide ions at the TiO₂ surface can then be described by the following equation:

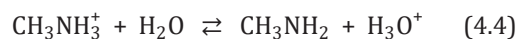


The formation of I₂ at the TiO₂/MAPbI₃ interface can deteriorate the overall perovskite structure. The existence of I₂ as a by-product of UV degradation was reported by Abdelmageed et al [27]. Although this scenario can explain the irreversibility of UV-induced damage observed in our results, it does not set a threshold value for photon energy below which the photo-damage is not observed. Therefore, this scenario alone does not explain the damage observed in our results. In fact, even a combined process of the two above scenarios does not support the results obtained by our work; when oxygen desorption is first activated by UV radiation (with photon energies above the bandgap of TiO₂), electrons, at the active Ti³⁺ sites, will rather favor the direction out of TiO₂.

A feasible mechanism for the UV-damage can be explained through the methylammonium ions CH₃NH₃⁺ as well as the small formation energy of MAPbI₃ from PbI₂ and MAI precursors, which is estimated to be ~ 0.1 eV as discussed in Chapter 1. Here, we also refer to the work of Abdelmageed et al [27], in which Fourier-Transform Infrared Spectroscopy (FTIR) showed that the UV-degradation process is accompanied by the decrease of NH₃ bands, unlike the CH₃ bands. In addition to this spectroscopic observation, the small formation energy of MAPbI₃ suggests that PbI₂ and MAI can co-exist with the perovskite phase. This reversible phase transformation can be highly enhanced with the existence of water molecules [30]. In this case, the following reactions can take place at the TiO₂ interface:



Therefore, UV-radiation merely liberates O₂ molecules that subsequently react with MAI to produce methyl amine CH₃NH₂, water and iodine. The presence of iodine as a result of UV-degradation was experimentally observed by Ref. [27]. Also, escalating evidences have been reporting the existence of methyl amine CH₃NH₂ (boiling point -6.6 °C [46]) in UV-damaged MAPbI₃ [27], and at the grain boundaries of untreated MAPbI₃ as well [47], [48]. Now with the help of water molecules, which can be present in the ambient or as a byproduct from Eq. 4.3, we have the following reaction:



As will be discussed below, we think that the reaction in Eq. 4.4 is a determining reaction for the UV-damage in our samples. Eq. 4.4 represents an acid-base reaction which is in equilibrium. The preferred direction of such a reaction can be estimated from the acid dissociation constant, expressed as pK_a values, of the reactants [49]. The positively charged CH_3NH_3^+ has a lower pK_a of 10.6, compared to H_2O with a pK_a of 15.7. Therefore, CH_3NH_3^+ will work as an acid in this reaction. The conjugate acid in this reaction, H_3O^+ , has pK_a of ~ -2 , which indicates that the reaction will prefer the left direction, as reactions prefer the direction towards weak acids and bases (strong acids and bases have stronger tendency to react). The same argument goes for the conjugate base CH_3NH_2 having pK_a of ~ 35 . In fact, this result can indeed partially explain the “permanence” of CH_3NH_3^+ ions in the MAPbI₃ lattice, despite their reported strong movements inside the PbI_6^- octahedral cages. However, imbalance in Eq. 4.4 can be imposed when the volatile CH_3NH_2 molecules are created by an external mechanism such as Eq. 4.3, and evaporate [28]. This will shift the equilibrium of Eq. 4.4 to the right side, which further enhances the perovskite degradation.

This scenario, although reasonable, does not explain the absence of UV damage at low temperatures as will be shown in Sec. 4.3.2. It also does not inform about the nature of MAI/O₂ interaction with light in Eq. 4.3.

UV Degradation at the Al₂O₃/MAPbI₃ interface

Considering the ambient gas molecules, Al₂O₃ is well-known for the high adsorption of water molecules, which passivate the under-coordinated Al atoms on the Al-terminated surface [50], [51]. In fact, Al₂O₃ is an efficient industrial material for the removal of water from gas streams [52]. Theoretical [50] and experimental [53] investigations showed that this adsorption process might, under certain conditions, favorably result in the dissociation of water molecules resulting in hydroxylated Al₂O₃ surface, i.e. terminated with hydroxyl OH⁻ molecules. Adjacent hydroxyl OH⁻ molecules on the termination surface can further bind through “in-plane” “extensive” hydrogen bonding [51]. Therefore, adsorption of water molecules on Al₂O₃ surface result in strongly bound surface adsorbates.

For the Al₂O₃/MAPbI₃ interface, in addition to the strong binding of surface molecules to the Al₂O₃ surface, the bandgap of Al₂O₃ (~ 7 eV), which is higher than the excitation photon energies used in our experiment, directly excludes the scenario explained by Eq. 4.2 through the bandgap-mediated desorption of surface molecules. Therefore, a different scenario must be responsible for the interfacial UV-damage, as also revealed by the longer PL decay dynamics compared to the TiO₂/MAPbI₃ sample (Figure 4.4a).

In fact, Eq. 4.4 suggests that the adsorbed H₂O molecules on the Al₂O₃ surface can promote a shift of the equilibrium to the right. Therefore, the existence of water molecules can directly result in enhancing the CH_3NH_3^+ to CH_3NH_2 transformation. However, this does not explain how this process can be UV-assisted. A possible explanation might be the direct desorption of H₂O or OH⁻ molecules by UV radiation. Hass et al [50] calculated the maximum energy required for this desorption process to be ~ 2 eV, which is still well below the photon energy of the blue 425 pulses, thus failing to explain our results.

Saif Haque and his group [54]–[56] proposed a different degradation mechanism, where the photoexcited electrons in MAPbI₃ can be captured by oxygen molecules in the ambient atmosphere, resulting in superoxide O₂⁻ molecules. Those O₂⁻ molecules can then directly react with the MA ions in the perovskite lattice. The probability of O₂ molecules in air capturing the excited electron in the CB of MAPbI₃ will be enhanced by the mismatch between CB levels of MAPbI₃ and Al₂O₃ that prevents electrons to be rather injected into Al₂O₃. They showed a nicely designed experiment, where the reaction between CH₃NH₃⁺ and O₂⁻ (in a solution containing both ions) could be clearly inferred. In fact, our experiment was carried out in vacuum, which weakens the importance of oxygen molecules in air for the UV-degradation process. Also, this scenario sets a photon excitation limit that equals the bandgap of MAPbI₃ (~ 1.6 eV), which does not conform with our results as well.

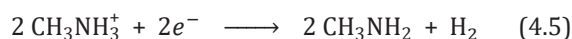
UV Degradation in bulk MAPbI₃

The UV-induced damage in the MAPbI₃_Film sample, manifest in Figure 4.3b, contradicts with some previous reports that UV-degradation is only associated with the TiO₂ interface [25], [27], [28], and with some others stating that oxygen and UV have to simultaneously exist in order for the UV-damage to be initiated [27], [54]–[56]. In fact, our results unambiguously indicate the presence of UV-degradation mechanism that takes place in the MAPbI₃ bulk as well. Therefore, a different mechanism for UV degradation, that happens in the bulk of the perovskite first, and which does not depend on the existence of oxygen in the ambient, must be present as well.

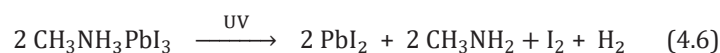
Here, we propose, as the primary degradation step under UV radiation, the direct dissociation of the molecular bonds in the CH₃NH₃⁺ molecule. At room temperature, MAPbI₃ is in its tetragonal phase, and the molecular size of MA cation is small compared to the size of the octahedral cage, making it weakly bound to the inorganic PbI₆⁻ framework. The thermal energy (26 meV) is high enough to overcome the energy barrier required for the MA cation movements in the octahedral cage (the thermal barrier for MA rotation is estimated to be ~ 13 meV [57], and the thermal barrier for all possible movements is estimated to be < 40 meV [58]). In this sense, the CH₃NH₃⁺ cation can be dealt with as a disparate molecular entity that can individually be affected by the incoming UV radiation.

Direct photo-dissociation of molecules is a well-known phenomenon that has been widely used for the selective conversion of organic molecules by the dissociation of one or more molecular bonds [59]–[61]. The bond dissociation energies of molecular bonds involved in the conversion will then set the threshold photon energy limits for this process. Table 4.1 shows the bond dissociation energies for the C-N, C-H and N-H bonds. Interestingly, they all have values above 2.9 eV, the photon energy at 425 nm, which explains the stability of the perovskite structure at this excitation wavelength.

Under excitation with 280 nm pulses, whose photon energy of 4.4 eV is above all bond dissociation energies in Table 4.1, many possible degradation pathways can take place. Here, we mainly consider, for reasons below, the conversion of CH₃NH₃⁺ ions into CH₃NH₂ gas, which can take the following equation:



where the electrons can be transferred from the CB of perovskite to the MA ion. Under vacuum, the volatile CH₃NH₂ molecules will evaporate, which will direct the equilibrium of Eq. 4.4 to the right, thus introducing another possible degradation channel. Dissociation of the other bonds will result in both negatively charged and positively charged by-products, making them less likely to occur. This agrees very well with the above-mentioned experimental observations on the UV-degradation by-products reported by other people; i.e. decrease of the NH₃ bands in the FTIR spectra against constancy of CH₃ bands and the existence of CH₃NH₂ molecules as well [27]. It should be noticed here that Eq. 4.5 only describes the “anticipated” first UV degradation step, and that subsequent reactions, with no UV energy threshold, would also be activated after that. As UV degradation ultimately results in MAPbI₃ transforming to the PbI₂ phase, which has been consistently reported by many people [27], [28], [54], [56], [62], [63], we can write the overall UV degradation equation of MAPbI₃ as follows:



This scenario is worth to be tested at lower temperatures for two reasons. First, at lower temperatures, CH₃NH₂ gas condenses into a liquid phase, which will keep the strong directionality of Eq. 4.4 towards the left side, thus supposedly reducing the UV-degradation rate. Second, the thermally excited movements of CH₃NH₃⁺ ions can be eliminated at temperatures lower than their thermal barrier. Also, the steric confinement of CH₃NH₃⁺ ions caused by the reduced dimensions of the crystalline unit cell at low temperatures, in addition to their reduced thermal motion, will further induce hydrogen bonding between the CH₃NH₃⁺ ions and the PbI₆⁻ lattice [64]–[66]. Therefore, if the CH₃NH₃⁺ is responsible for the first degradation step under UV illumination, then at temperatures lower than the thermal barrier necessary to liberate the CH₃NH₃⁺ ion movements, UV-degradation is expected to be largely reduced or even eliminated. Indeed, this could be successfully demonstrated by temperature-dependent TRPL and TIPL measurements as will be discussed below.

Table 4.1 Bond dissociation energies of the molecular bonds in CH₃NH₃⁺ [49]

Bond	Bond Dissociation Energy (eV)
N-H	4.00
C-H	4.26
C-N	3.16

4.3.2 Low Temperature Measurements

Figure 4.5 shows the temperature-dependent TIPL measurements of all samples, excited by the 280 nm UV pulses, in the temperature range between 200-300 K, where the room-temperature tetragonal perovskite phase is ensured. It has to be mentioned here that for all the following TIPL measurements, and in order to minimize the contribution of UV damage to the temperature dependent results, care was taken to record the PL signal on the CCD immediately upon excitation, and to change the excitation position on the sample for each temperature measurement. Below 200 K, the PL intensity is surprisingly stable over time. At ~ 220 -230 K, a rapid decrease in the PL intensity is observed for all samples, indicating the onset of trap activation at this temperature. This temperature dependent drop is abrupt for MAPbI₃/ms-TiO₂ and MAPbI₃_Film, and it takes a gradual yet fast behavior with MAPbI₃/ms-Al₂O₃, as can be seen in Figure 4.5. To further clarify the abrupt PL drop, temperature dependent TIPL measurements were carried out for MAPbI₃_Film over a wider temperature range, and the results are shown in Figure 4.6a & b. The tetragonal to orthorhombic phase transition can be noticed at ~ 150 K. Below 150 K, the confinement of MA cations in the PbI₆⁻ framework is manifested by the two PL peaks, where the higher energy peak can be assigned to orthorhombic domains with ordered MA cations, whereas the lower energy one is assigned to orthorhombic domains whose MA cations are spatially trapped by cooling in a disordered configuration [67]. Figure 4.6b shows the integrated TIPL intensity versus temperature. The abrupt PL decrease can be clearly noticed at ~ 230 K, from which an activation energy of ~ 20 meV can be estimated. This value agrees very well with the thermal barrier of CH₃NH₃⁺ movements in the perovskite lattice [58].

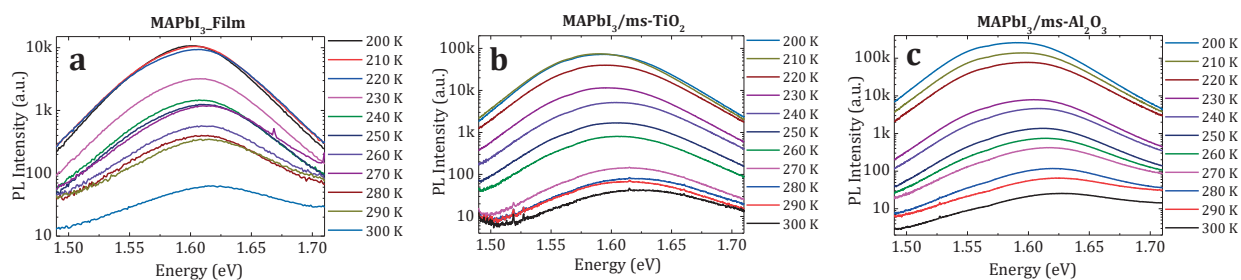


Figure 4.5 TRIL measurements between 200-300 K for (a) MAPbI₃_Film (b) MAPbI₃/ms-TiO₂ and (c) MAPbI₃/ms-Al₂O₃

Figure 4.7 shows the UV-degradation of MAPbI₃_Film with time at different temperatures of 200 K, 230 K, and 260 K. Interestingly, at 200 K, the PL intensity is stable with time, with no UV-induced PL deterioration observed. The strong fluctuations in PL intensity, especially at low temperatures, have been observed before by Tachikawa et al [68] and Yuan et al [69], and can be attributed to physiochemical processes at the perovskite surface [68], [69]. In fact, assigning the origin of these fluctuations to the perovskite surface fits also with the fact as these fluctuations diminish at higher temperatures when the perovskite phase is damaged under UV radiation. At 230 K, at which the MA⁺ movements are thermally liberated, the time degradation of TIPL signal starts to appear as well, indicating the onset of UV-induced

damage, which is further enhanced at 260 K. Therefore, based on our proposed scenario and supported by the temperature-dependent findings, the UV-damage is correlated with the thermal activation of MA⁺ movements in the perovskite lattice.

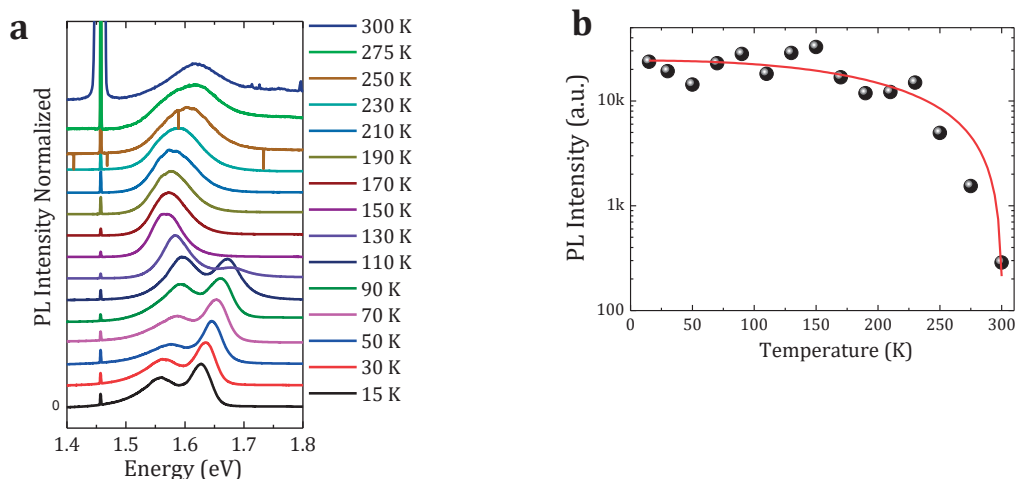


Figure 4.6 (a) TIPL measurements for MAPbI₃_Film over extended temperature range between 15-300 K. (b) Extracted integrated TIPL intensity versus temperature for the same sample

Time-resolved PL measurements were carried out at ~ 200 K, 230 K and 260 K to further investigate the above noticed onset of UV-damage, and the results are shown in Figure 4.8. Interestingly, for MAPbI₃/ms-Al₂O₃ and MAPbI₃_Film, all the fast sub-nanosecond decay channels were absent, and long PL decays are observed, which can be attributed to the SRH recombination of the bulk traps in the material, which was similarly observed when the samples are excited with 425 nm pulses in Figure 4.4b. At 230 K, which is the onset of UV-induced damage as shown by Figure 4.7, fast decay channels were interestingly activated for MAPbI₃/ms-Al₂O₃ and MAPbI₃_Film samples.

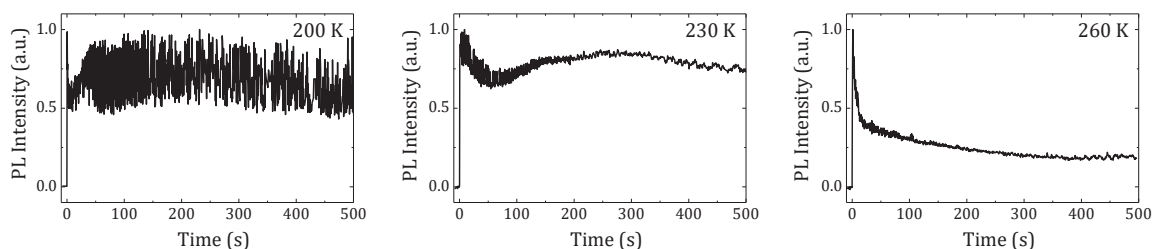


Figure 4.7 PL intensity degradation with time for MAPbI₃_Film induced by the UV excitation of 280 nm pulses at 200 K, 230 K and 260 K.

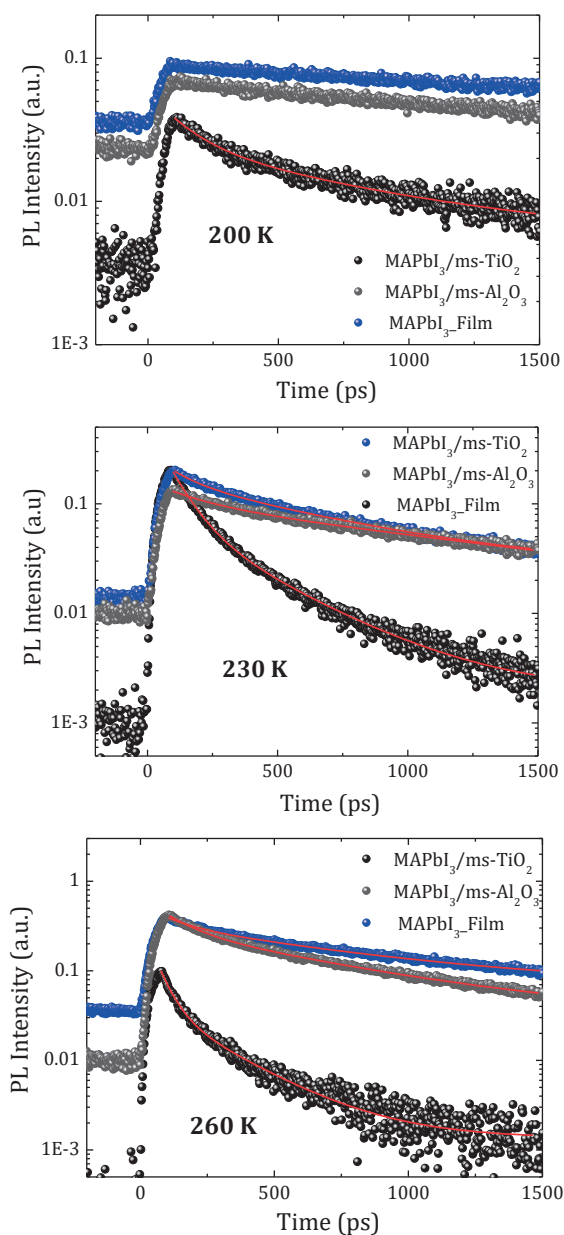


Figure 4.8 TRPL of samples at different temperatures of 200 K, 230 K and 260 K

For MAPbI₃/ms-TiO₂, a relatively long decay at 200 K is accompanied by a fast decay component as well. We want to emphasize here that the UV-induced damage was also absent at this temperature for MAPbI₃/ms-TiO₂. The fast decay component can thus be explained by the UV-induced desorption of oxygen molecules at the TiO₂ surface, which create surface traps for the excited electrons in MAPbI₃.

In Sec. 4.3.3 below, we rationalize all of our findings based on the analysis and conclusions discussed above in order to construct a comprehensive understanding of PL dynamics observed in our samples.

4.3.3 Rationalizing the results

For MAPbI₃/ms-TiO₂, there is no UV-induced damage in the PL signal at 200 K. However a faster PL decay is observed. Oxygen atoms will be desorbed by the above-TiO₂-bandgap UV photons resulting in O₂ molecules and active Ti³⁺ sites. The Ti³⁺ sites will work as surface traps for the excited electrons in the perovskite material. Additionally, oxygen molecules can re-adsorb again on the surface, possibly contributing to the observed PL fluctuations. The vacuum condition, under which our experiment is performed, might be responsible for the intermittent nature of such fluctuations. Therefore, what UV pulses do in the case of MAPbI₃/ms-TiO₂ sample at 200 K is that they activate the TiO₂ surface creating efficient traps for electrons in the perovskite material.

Now, above 200 K, liberated CH₃NH₃⁺ ions will undergo direct dissociation by the UV pulses resulting in CH₃NH₂ molecules as a by-product. The CH₃NH₂ molecules can in turn result in further dissociation of CH₃NH₃⁺ molecules as driven by the reaction described by Eq. 4.4. Iodide ions can also result out of this reaction, for which the iodine-driven degradation pathway mentioned above, and catalyzed by the activated TiO₂ surface, can also share the damage responsibility. Therefore, different kinds of traps can be created during the damage process. Hence, we believe that the PL decay measured at higher temperatures does not contain only two decay channels, and that other channels have to be present as well; the PL decay fitted with two exponential decay constants can indeed accept more exponential decay terms in the fitting function.

In the MAPbI₃/ms-Al₂O₃ sample, desorption of H₂O molecules mediated through Al₂O₃ does not work due the large bandgap. This is nicely reflected by the absence of fast decay channels at 200 K. Above 200 K, the direct dissociation of CH₃NH₃⁺ bonds results in different degradation pathways as discussed above. The existence of water molecules, which is an important ingredient of Eq. 4.4, and possibly other adsorbates, on the Al₂O₃ surface will result in PL dynamics that should be different than both MAPbI₃/ms-TiO₂ and MAPbI₃_Film, with the latter only related to traps created by the direct degradation of CH₃NH₃⁺ ions in the perovskite bulk. As our experiments were carried out in vacuum, interaction of CH₃NH₃⁺ with peroxide O₂⁻ molecules would not contribute to the observed damage, and thus must not be overlooked in other oxygen-rich situations.

In fact, the photo-induced desorption of surface molecules can also take place at the MAPbI₃ surface. MAPbI₃-mediated desorption of such molecules might, therefore, take place if the photon energy is higher than the bandgap of MAPbI₃, ~ 1.6 eV. This effect should, consequently, be observed under both 280 nm and 425 nm pulses. In fact, as discussed in Chapter 1, traps created in the perovskite material commonly have shallow energy levels. Surface defects in MAPbI₃ also own this property [70], and hence should result in PL decay times comparable to that from the bulk. Therefore, it is possible that the long SRH decay times, observed both under 425 nm excitation at 300 K and under 280 nm at 200 K, include both bulk and surface traps, which cannot be resolved by the short ~ 1.5 ns window in the streak image. Those traps can however contribute to the observed strong PL fluctuations, whose intermittency can be further enhanced by the vacuum environment.

4.4 A Word about Electron Injection at the MAPbI₃/TiO₂ interface

In MAPbI₃/ms-TiO₂, it is energetically possible that excited electrons in MAPbI₃ can be injected into the CB of TiO₂, unlike the case of MAPbI₃/ms-Al₂O₃ where the CB of Al₂O₃ lies higher than that of MAPbI₃. However, going back to Figure 4.4b, i.e. TRPL measurements under 425 nm excitation, the PL decay of MAPbI₃/ms-TiO₂ is almost similar to the other samples, and shows no sign of charge injection, which should be manifested by an additional decay component. Therefore, we can conclude that, at least for the time range of 1.5 ns, electron injection into the ms-TiO₂ layer is not the main process behind charge separation in ms-TiO₂ based perovskite solar cells. In order to further confirm this result, TRPL measurements were carried out for the sequentially deposited MAPbI₃/ms-TiO₂ under 425 nm excitation. The result is shown in Figure 4.9 along with the TRPL result of the sequentially deposited MAPbI₃/ms-Al₂O₃ (from Figure 4.2). Clearly, the PL dynamics is again almost independent of the scaffold material used, further confirming the absence of electron transfer across the MAPbI₃/TiO₂ interface.

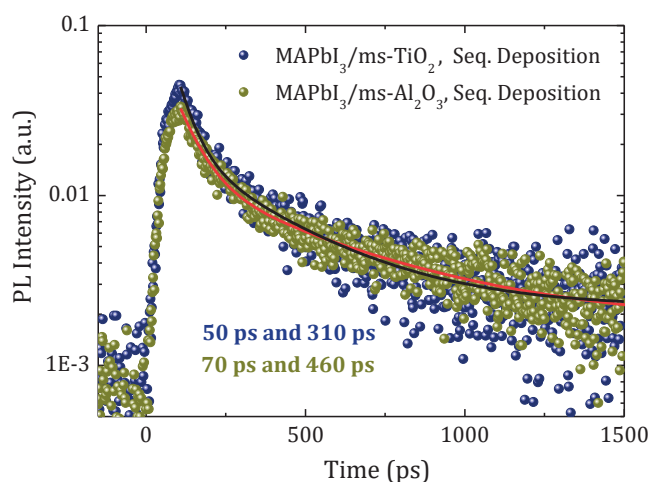


Figure 4.9 Comparison between TRPL decays for MAPbI₃ deposited on TiO₂ and Al₂O₃ scaffold using the sequential deposition method at 300 K. The samples were excited using 425 nm pulses and laser power of 200 μ W.

In fact, despite a prevailing common belief in the available published literature on the existence of electron transfer across the MAPbI₃/TiO₂, a consequence of perovskite solar cells being emerging from the field of dye-sensitized solar cells where electron injection at the dye/TiO₂ interface is the primary charge separation process, the weakness/absence of electron injection was experimentally verified as early as in 2012 by Kim et al [14], and by few other reports after that [33], [34], [71]. The ineffectiveness of charge separation at the MAPbI₃/TiO₂ interface, although energetically feasible, is explained by Xing et al [71] as a result from the high density of surface defects on both the TiO₂ surface (such as Ti³⁺ defect sites) and the MAPbI₃ surface. The nature of intrinsic defects in MAPbI₃ can be understood by Eqs. 1.3, where MA vacancies can easily form, with densities as high as $\sim 10^{20}$ cm⁻³ as discussed in Chapter 1, even for MAPbI₃

prepared under stoichiometric conditions. As defects have the tendency to concentrate on the surface or at grain boundaries, these negatively charged defect sites will therefore result in a p-type MAPbI₃. The high density of defects for both TiO₂ and MAPbI₃ will result in band bending at their surfaces. At the MAPbI₃/TiO₂ interface, which will make a p-n junction, electron migration will take place from TiO₂ to MAPbI₃ until their two Fermi levels are aligned, thus passivating the surface defects at both materials. However, the high density of surface defects at both materials can result in a strong built-in electric field that will make an energy barrier against electron transfer, as schematically drawn in Figure 4.10a. Chen et al [33] reported, based on experimental observations, the existence of PbI₂ at the MAPbI₃/TiO₂ which can make a spatial as well as energy barrier for the electron transfer process, as depicted in Figure 4.10b. The conduction and valence band levels of PbI₂ lying, respectively, above and below those of MAPbI₃, will make type I energy barriers for photoexcited electrons and holes in the MAPbI₃ bulk. A similar conclusion was also reported by Wang et al [34].

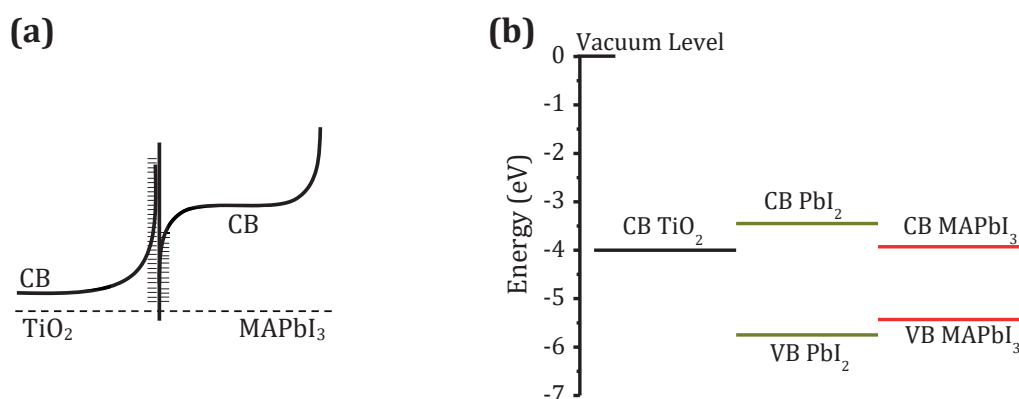


Figure 4.10 (a) Schematic showing the band bending effects at the MAPbI₃/TiO₂ interface resulting in an energy barrier, adapted from Ref. [71]. (b) Energy level diagram for a TiO₂/PbI₂/MAPbI₃ interface. The PbI₂ mid-layer will obstruct electron transfer from MAPbI₃ to TiO₂. Adapted from Ref. [33]

In summary, this chapter confirms that UV degradation is not only associated with the TiO₂ surface or with the presence of oxygen, as has been shown in previously published reports. Additionally, an intrinsic UV degradation mechanism also exists, which switches off below 200 K. Considering this result and the available literature, the bond dissociation (mainly the N-H bond) in liberated CH₃NH₃⁺ ions is suggested to be the primary step in the UV degradation process. This, in fact, explains the instability of both ms-TiO₂ and ms-Al₂O₃ based perovskite solar cell devices under UV radiation. The take-home message from this chapter is that replacement of MA with a more stable cation, e.g. Formamidinium FA having one order of magnitude higher energy barrier for thermal movements in the octahedral cage [57], can be a feasible strategy to realize UV-stable devices. Also, care must be taken when TRPL measurements are carried out on perovskite/ms-TiO₂ interfaces, as the PL decay can result from either UV created traps or from UV-activated traps on the TiO₂ surface, rather than from electron injection across the interface, which is shown to be though insignificant.

References

- [1] A. J. Nozik, "Quantum dot solar cells," *Phys. E*, vol. 14, pp. 115–120, 2002.
- [2] I. Mora-Seró, S. Giménez, F. Fabregat-Santiago, R. Gómez, Q. Shen, T. Toyoda, and J. Bisquert, "Recombination in quantum dot sensitized solar cells," *Acc. Chem. Res.*, vol. 42, no. 11, pp. 1848–1857, 2009.
- [3] P. V. Kamat, "Quantum Dot Solar Cells. *The Next Big Thing* in Photovoltaics," *J. Phys. Chem. Lett.*, vol. 4, no. 6, pp. 908–918, 2013.
- [4] G. H. Carey, A. L. Abdelhady, Z. Ning, S. M. Thon, O. M. Bakr, and E. H. Sargent, "Colloidal Quantum Dot Solar Cells," *Chem. Rev.*, vol. 115, no. 23, pp. 12732–12763, 2015.
- [5] A. Kojima, K. Teshima, T. Miyasaka, and Y. Shirai, "Novel photoelectrochemical cell with mesoscopic electrodes sensitized by lead-halide compounds (2)," in *Meeting Abstracts*, no. 7, pp. 397, 2006.
- [6] A. Kojima, K. Teshima, Y. Shirai, and T. Miyasaka, "Novel photoelectrochemical cell with mesoscopic electrodes sensitized by lead-halide compounds (5)," in *Meeting Abstracts*, no. 8, pp. 352, 2007.
- [7] A. Kojima, K. Teshima, Y. Shirai, and T. Miyasaka, "Novel photoelectrochemical cell with mesoscopic electrodes sensitized by lead-halide compounds (11)," in *Meeting Abstracts*, no. 1, pp. 27, 2008.
- [8] T. Miyasaka, A. Kojima, and K. Teshima, "Lead halide perovskites as quantum dot sensitizers for mesoscopic TiO₂ photovoltaic cells," in *Meeting Abstracts*, no. 9, pp. 742, 2009.
- [9] A. Kojima, K. Teshima, Y. Shirai, and T. Miyasaka, "Organometal Halide Perovskites as Visible-Light Sensitizers for Photovoltaic Cells," *J. Am. Chem. Soc.*, vol. 131, no. 17, pp. 6050–6051, 2009.
- [10] J.-H. Im, C.-R. Lee, J.-W. Lee, S.-W. Park, and N.-G. Park, "6.5% efficient perovskite quantum-dot-sensitized solar cell," *Nanoscale*, vol. 3, pp. 4088–4093, 2011.
- [11] G. Benkő *et al.*, G. Benkő, P. Myllyperkiö, J. Kallioinen, P. Myllyperkiö, F. Trif, J. E. I. Korppi-Tommola, A. P. Yartsev, V. Sundström, and V. Sundström, "Interligand Electron Transfer Determines Triplet Excited State Electron Injection in RuN3-Sensitized TiO₂ Films," *J. Phys. Chem. B*, vol. 108, no. 9, pp. 2862–2867, 2004.
- [12] M. M. Lee, J. Teuscher, T. Miyasaka, T. N. Murakami, and H. J. Snaith, "Efficient Hybrid Solar Cells Based on Meso-Superstructured Organometal Halide Perovskites," *Science*, vol. 338, no. 6107, pp. 643–647, 2012.
- [13] J. M. Ball, M. M. Lee, A. Hey, and H. J. Snaith, "Low-temperature processed meso-superstructured to thin-film perovskite solar cells," *Energy Environ. Sci.*, vol. 6, pp. 1739–1743, 2013.
- [14] H.-S. Kim, C.-R. Lee, J.-H. Im, K.-B. Lee, T. Moehl, A. Marchioro, S.-J. Moon, R. Humphry-Baker, J.-H. Yum, J. E. Moser, M. Graetzel, and N.-G. Park, "Lead Iodide Perovskite Sensitized All-Solid-State Submicron Thin Film Mesoscopic Solar Cell with Efficiency Exceeding 9%," *Sci. Rep.*, vol. 2, pp. 583–585, 2012.
- [15] J. Burschka, N. Pellet, S.-J. Moon, R. Humphry-Baker, P. Gao, M. K. Nazeeruddin, and M. Graetzel, "Sequential deposition as a route to high-performance perovskite-sensitized solar cells," *Nature*, vol. 499, no. 7458, pp. 316–319, 2013.
- [16] N. J. Jeon, J. H. Noh, Y. C. Kim, W. S. Yang, S. Ryu, and S. Il Seok, "Solvent engineering for high-performance inorganic-organic hybrid perovskite solar cells," *Nat. Mater.*, vol. 13, pp. 897–903, 2014.
- [17] N. Arora, M. I. Dar, M. Hezam, W. Tress, G. Jacopin, T. Moehl, P. Gao, A. S. Aldwayyan, B. Deveaud, M. Grätzel, and M. K. Nazeeruddin, "Photovoltaic and Amplified Spontaneous Emission Studies of High-Quality Formamidinium Lead Bromide Perovskite Films," *Adv. Funct. Mater.*, vol. 26, no. 17, pp. 2846–2854, 2016.
- [18] N. Arora, M. I. Dar, M. Abdi-Jalebi, F. Giordano, N. Pellet, G. Jacopin, R. H. Friend, S. M. Zakeeruddin and M. Grätzel, "Intrinsic and Extrinsic Stability of Formamidinium Lead Bromide Perovskite Solar Cells Yielding High Photovoltage," *Nano Lett.*, vol. 16, no. 11, pp. 7155–7162, 2016.

- [19] H. J. Snaith, A. Abate, J. M. Ball, G. E. Eperon, T. Leijtens, N. K. Noel, S. D. Stranks, J. T.-W. Wang, K. Wojciechowski, and W. Zhang, "Anomalous hysteresis in perovskite solar cells," *J. Phys. Chem. Lett.*, vol. 5, no. 9, pp. 1511–1515, 2014.
- [20] A. M. A. Leguy, Y. Hu, M. Campoy-Quiles, M. I. Alonso, O. J. Weber, P. Azarhoosh, M. van Schilfgaarde, M. T. Weller, T. Bein, J. Nelson, P. Docampo, and P. R. F. Barnes, "Reversible Hydration of CH₃NH₃PbI₃ in Films, Single Crystals, and Solar Cells," *Chem. Mater.*, vol. 27, no. 9, pp. 3397–3407, 2015.
- [21] Y. Han, S. Meyer, Y. Dkhissi, K. Weber, J. M. Pringle, U. Bach, L. Spiccia, and Y.-B. Cheng, "Degradation observations of encapsulated planar CH₃NH₃PbI₃ perovskite solar cells at high temperatures and humidity," *J. Mater. Chem. A*, vol. 3, pp. 8139–8147, 2015.
- [22] G. Niu, W. Li, F. Meng, L. Wang, H. Dong, and Y. Qiu, "Study on the stability of CH₃NH₃PbI₃ films and the effect of post-modification by aluminum oxide in all-solid-state hybrid solar cells," *J. Mater. Chem. A*, vol. 2, pp. 705–710, 2014.
- [23] J. Zhao, B. Cai, Z. Luo, Y. Dong, Y. Zhang, H. Xu, B. Hong, Y. Yang, L. Li, W. Zhang, and C. Gao, "Investigation of the Hydrolysis of Perovskite Organometallic Halide CH₃NH₃PbI₃ in Humidity Environment," *Sci. Rep.*, vol. 6, pp. 21976, 2016.
- [24] J. Yang, B. D. Siempelkamp, D. Liu, and T. L. Kelly, "Investigation of CH₃NH₃PbI₃ Degradation Rates and Mechanisms in Controlled Humidity Environments Using *in Situ* Techniques," *ACS Nano*, vol. 9, no. 2, pp. 1955–1963, 2015.
- [25] T. Leijtens, G. E. Eperon, S. Pathak, A. Abate, M. M. Lee, and H. J. Snaith, "Overcoming ultraviolet light instability of sensitized TiO₂ with meso-superstructured organometal tri-halide perovskite solar cells," *Nat. Commun.*, vol. 4, pp. 583–585, 2013.
- [26] A. J. Pearson, G. E. Eperon, P. E. Hopkinson, S. N. Habisreutinger, J. T.-W. Wang, H. J. Snaith, and N. C. Greenham, "Oxygen Degradation in Mesoporous Al₂O₃/CH₃NH₃PbI_{3-x}Cl_x Perovskite Solar Cells: Kinetics and Mechanisms," *Adv. Energy Mater.*, vol. 6, no. 13, pp. 1600014, 2016.
- [27] G. Abdelmageed, L. Jewell, K. Hellier, L. Seymour, B. Luo, F. Bridges, J. Z. Zhang, and S. Carter, "Mechanisms for light induced degradation in MAPbI₃ perovskite thin films and solar cells," *Appl. Phys. Lett.*, vol. 109, no. 23, pp. 233905, 2016.
- [28] S. Ito, S. Tanaka, K. Manabe, and H. Nishino, "Effects of Surface Blocking Layer of Sb₂S₃ on Nanocrystalline TiO₂ for CH₃NH₃PbI₃ Perovskite Solar Cells," *J. Phys. Chem. C*, vol. 118, no. 30, pp. 16995-17000, 2014.
- [29] G. Murugadoss, S. Tanaka, G. Mizuta, S. Kanaya, H. Nishino, T. Umeyama, H. Imahori, and S. Ito, "Light stability tests of methylammonium and formamidinium Pb-halide perovskites for solar cell applications," *Jpn. J. Appl. Phys.*, vol. 54, no. 8S1, pp. 08KF08, 2015.
- [30] Z. Wang, Z. Shi, T. Li, Y. Chen, and W. Huang, "Stability of Perovskite Solar Cells: A Prospective on the Substitution of the A Cation and X Anion," *Angew. Chem. Int. Ed.*, vol. 56, no. 5, pp. 1190-1212, 2017.
- [31] T. A. Berhe, W.-N. Su, C.-H. Chen, C.-J. Pan, J.-H. Cheng, H.-M. Chen, M.-C. Tsai, L.-Y. Chen, A. A. Dubale, and B.-J. Hwang, "Organometal halide perovskite solar cells: degradation and stability," *Energy Environ. Sci.*, vol. 9, pp. 323-356, 2016.
- [32] E. Guillén, F. J. Ramos, J. A. Anta, and S. Ahmad, "Elucidating transport-recombination mechanisms in perovskite solar cells by small-perturbation techniques," *J. Phys. Chem. C*, vol. 118, no. 40, pp. 22913–22922, 2014.
- [33] Q. Chen, H. Zhou, T.-B. Song, S. Luo, Z. Hong, H.-S. Duan, L. Dou, Y. Liu, and Y. Yang, "Controllable self-induced passivation of hybrid lead iodide perovskites toward high performance solar cells," *Nano Lett.*, vol. 14, no. 7, pp. 4158–4163, 2014.
- [34] L. Wang, C. McCleese, A. Kovalsky, Y. Zhao, and C. Burda, "Femtosecond Time-Resolved Transient Absorption

- Spectroscopy of $\text{CH}_3\text{NH}_3\text{PbI}_3$ Perovskite Films: Evidence for Passivation Effect of PbI_2 ," *J. Am. Chem. Soc.*, vol. 136, no. 35, pp. 12205-12208, 2014.
- [35] P. Qin, A. L. Domanski, A. K. Chandiran, R. Berger, H.-J. Butt, M. I. Dar, T. Moehl, N. Tetreault, P. Gao, S. Ahmad, M. K. Nazeeruddin, and M. Grätzel, "Yttrium-substituted nanocrystalline TiO_2 photoanodes for perovskite based heterojunction solar cells," *Nanoscale*, vol. 6, pp. 1508-1514, 2014.
- [36] P. Qin, S. Tanaka, S. Ito, N. Tetreault, K. Manabe, H. Nishino, M. K. Nazeeruddin, and M. Grätzel, "Inorganic hole conductor-based lead halide perovskite solar cells with 12.4% conversion efficiency," *Nat. Commun.*, vol. 5, pp. 3834, 2014.
- [37] A. A. Istratov and O. F. Vyvenko, "Exponential analysis in physical phenomena," *Rev. Sci. Instrum.*, vol. 70, no. 2, pp. 1233-1257, 1999.
- [38] G. Lu, A. Linsebigler, and J. T. Yates, "The adsorption and photodesorption of oxygen on the $\text{TiO}_2(110)$ surface," *J. Chem. Phys.*, vol. 102, no. 11, pp. 4657-4662, 1995.
- [39] M. A. Henderson, W. S. Epling, C. L. Perkins, C. H. F. Peden, and U. Diebold, "Interaction of Molecular Oxygen with the Vacuum-Annealed $\text{TiO}_2(110)$ Surface: Molecular and Dissociative Channels," *J. Phys. Chem. B*, vol. 103, no. 25, pp. 5328-5337, 1999.
- [40] S. K. Pathak, A. Abate, P. Ruckdeschel, B. Roose, K. C. Gödel, Y. Vaynzof, A. Santhala, S.-I. Watanabe, D. J. Hollman, N. Noel, A. Sepe, U. Wiesner, R. Friend, H. J. Snaith, and U. Steiner, "Performance and Stability Enhancement of Dye-Sensitized and Perovskite Solar Cells by Al Doping of TiO_2 ," *Adv. Funct. Mater.*, vol. 24, no. 38, pp. 6046-6055, 2014.
- [41] N. Klein-Kedem, D. Cahen, and G. Hodes, "Effects of Light and Electron Beam Irradiation on Halide Perovskites and Their Solar Cells," *Acc. Chem. Res.*, vol. 49, no. 2, pp. 347-354, 2016.
- [42] B. Roose, K. C. Gödel, S. Pathak, A. Sadhanala, J. P. C. Baena, B. D. Wilts, H. J. Snaith, U. Wiesner, M. Grätzel, U. Steiner, and A. Abate, "Enhanced efficiency and stability of perovskite solar cells through Nd-doping of mesostructured TiO_2 ," *Adv. Energy Mater.*, vol. 6, no. 2, pp. 1501868, 2016.
- [43] T. Leijtens, G. E. Eperon, S. Pathak, A. Abate, M. M. Lee, and H. J. Snaith, "Overcoming ultraviolet light instability of sensitized TiO_2 with meso-superstructured organometal tri-halide perovskite solar cells," *Nat. Commun.*, vol. 4, pp. 583-585, 2013.
- [44] S. K. Pathak, A. Abate, T. Leijtens, D. J. Hollman, J. Teuscher, L. Pazos, P. Docampo, U. Steiner, and H. J. Snaith, "Towards long-term photostability of solid-state dye sensitized solar cells," *Adv. Energy Mater.*, vol. 4, no. 8, pp. 1301667, 2014.
- [45] H. M. Ghaithan, S. M. H. Qaid, M. Hezam, J. P. Labis, M. Alduraibi, I. M. Bedja, and A. S. Aldwayyan, "Laser induced photocurrent and photovoltage transient measurements of dye-sensitized solar cells based on TiO_2 nanosheets and TiO_2 nanoparticles," *Electrochim. Acta*, vol. 212, pp. 992-997, 2016.
- [46] H. D. Gibbs, "THE BOILING-POINTS OF AMMONIA, METHYL AMINE, METHYL CHLORIDE AND SULPHUR DIOXIDE," *J. Am. Chem. Soc.*, vol. 27, no. 7, pp. 851-865, 1905.
- [47] M. C. Jung, Y. M. Lee, H. K. Lee, J. Park, S. R. Raga, L. K. Ono, S. Wang, M. R. Leyden, B. D. Yu, S. Hong, and Y. Qi, "The presence of CH_3NH_2 neutral species in organometal halide perovskite films," *Appl. Phys. Lett.*, vol. 108, no. 7, pp. 073901, 2016.
- [48] A. Calloni, A. Abate, G. Bussetti, G. Berti, R. Yivlialin, F. Ciccacci, and L. Duò, "Stability of Organic Cations in Solution-Processed $\text{CH}_3\text{NH}_3\text{PbI}_3$ Perovskites: The Formation of Modified Surface Layers," *J. Phys. Chem. C*, vol. 119, no. 37, pp. 21329-21335, 2015.
- [49] J. E. Huheey, E. A. Keiter, and R. L. Keiter, *Inorganic Chemistry: Principles of Structure and Reactivity, 4th Edition*. HarperCollins College Publishers, 1993.
- [50] K. C. Hass, W. F. Schneider, A. Curioni, and W. Andreoni, "The Chemistry of Water on Alumina Surfaces:

- Reaction Dynamics from First Principles," *Science*, vol. 282, no. 5387, pp. 265–268, 1998.
- [51] P. J. Eng, T. P. Trainor, G. E. Brown Jr., G. A. Waychunas, M. Newville, S. R. Sutton, and M. L. Rivers, "Structure of the Hydrated-Al₂O₃ (0001) Surface," *Science*, vol. 288, no. 5468, pp. 1029–1033, 2000.
- [52] L. K. Hudson, C. Misra, A. J. Perrotta, K. Wefers, and F. S. Williams, "Aluminum Oxide," in *Ullmanns Encyclopedia of Industrial Chemistry*, vol. 2, pp. 607–645. Wiley-VCH, 2002.
- [53] J. W. Elam, C. E. Nelson, M. A. Cameron, M. A. Tolbert, and S. M. George, "Adsorption of H₂O on a single-crystal α -Al₂O₃(0001) surface," *J. Phys. Chem. B*, vol. 102, no. 36, pp. 7008–7015, 1998.
- [54] N. Aristidou, I. Sanchez-Molina, T. Chotchuangchutchaval, M. Brown, L. Martinez, T. Rath, and S. A. Haque, "The Role of Oxygen in the Degradation of Methylammonium Lead Trihalide Perovskite Photoactive Layers," *Angew. Chem. Int. Ed.*, vol. 54, no. 28, pp. 8208–8212, 2015.
- [55] F. T. F. O'Mahony, Y. H. Lee, C. Jellett, S. Dmitrov, D. T. J. Bryant, J. R. Durrant, B. C. O'Regan, M. Graetzel, M. K. Nazeeruddin, and S. A. Haque, "Improved environmental stability of organic lead trihalide perovskite-based photoactive-layers in the presence of mesoporous TiO₂," *J. Mater. Chem. A*, vol. 3, pp. 7219–7223, 2015.
- [56] D. Bryant, N. Aristidou, S. Pont, I. Sanchez-Molina, T. Chotchunangatchaval, S. Wheeler, J. R. Durrant, and S. A. Haque, "Light and oxygen induced degradation limits the operational stability of methylammonium lead triiodide perovskite solar cells," *Energy Environ. Sci.*, vol. 9, pp. 1655–1660, 2016.
- [57] J. M. Frost, K. T. Butler, F. Brivio, C. H. Hendon, M. Van Schilfgaarde, and A. Walsh, "Atomistic origins of high-performance in hybrid halide perovskite solar cells," *Nano Lett.*, vol. 14, no. 5, pp. 2584–2590, 2014.
- [58] J. M. Frost and A. Walsh, "What Is Moving in Hybrid Halide Perovskite Solar Cells?," *Accounts of Chemical Research*, vol. 49, no. 3, pp. 528–535, 2016.
- [59] M. A. Gondal, A. Hameed, Z. H. Yamani, and A. Arfaj, "Photocatalytic transformation of methane into methanol under UV laser irradiation over WO₃, TiO₂ and NiO catalysts," *Chem. Phys. Lett.*, vol. 392, no. 4–6, pp. 372–377, 2004.
- [60] A. H. Yahaya, M. A. Gondal, and A. Hameed, "Selective laser enhanced photocatalytic conversion of CO₂ into methanol," *Chem. Phys. Lett.*, vol. 400, no. 1–3, pp. 206–212, 2004.
- [61] M. A. Gondal, Z. H. Yamani, A. Dastgeer, M. A. Ali, and A. Arfaj, "Photo-Conversion of Methane into Higher Hydrocarbons Using 355 nm Laser Radiation," *Spectrosc. Lett.*, vol. 36, no. 4, pp. 313–326, 2003.
- [62] R. K. Misra, S. Aharon, B. Li, D. Mogilyansky, I. Visoly-Fisher, L. Etgar, and E. A. Katz, "Temperature- and component-dependent degradation of perovskite photovoltaic materials under concentrated sunlight," *J. Phys. Chem. Lett.*, vol. 6, no. 3, pp. 326–330, 2015.
- [63] W. Li, W. Zhang, S. Van Reenen, R. J. Sutton, J. Fan, A. A. Haghighirad, M. B. Johnston, L. Wang, and H. J. Snaith, "Enhanced UV-light stability of planar heterojunction perovskite solar cells with caesium bromide interface modification," *Energy Environ. Sci.*, vol. 9, pp. 490–498, 2016.
- [64] J.-H. Lee, N. C. Bristowe, P. D. Bristowe, and A. K. Cheetham, "Role of hydrogen-bonding and its interplay with octahedral tilting in CH₃NH₃PbI₃," *Chem. Commun.*, vol. 51, pp. 6434–6437, 2015.
- [65] J. H. Lee, J.-H. Lee, E.-H. Kong, and H. M. Jang, "The nature of hydrogen-bonding interaction in the prototypic hybrid halide perovskite, tetragonal CH₃NH₃PbI₃," *Sci. Rep.*, vol. 6, pp. 21687, 2016.
- [66] C. Motta, F. El-Mellouhi, and S. Sanvito, "Exploring the cation dynamics in lead-bromide hybrid perovskites," *Phys. Rev. B*, vol. 93, no. 23, pp. 235412, 2016.
- [67] M. I. Dar, G. Jacopin, S. Meloni, A. Mattoni, N. Arora, A. Boziki, S. M. Zakeeruddin, U. Rothlisberger, and M. Grätzel, "Origin of unusual bandgap shift and dual emission in organic-inorganic lead halide perovskites," *Sci. Adv.*, vol. 2, no. 10, pp. e1601156, 2016.

- [68] T. Tachikawa, I. Karimata, and Y. Kobori, "Surface Charge Trapping in Organolead Halide Perovskites Explored by Single-Particle Photoluminescence Imaging," *J. Phys. Chem. Lett.*, vol. 6, no. 16, pp. 3195–3201, 2015.
- [69] H. Yuan, E. Debroye, G. Caliendo, K. P. F. Janssen, J. van Loon, C. E. A. Kirschhock, J. A. Martens, J. Hofkens, and M. B. J. Roelofs, "Photoluminescence Blinking of Single-Crystal Methylammonium Lead Iodide Perovskite Nanorods Induced by Surface Traps," *ACS Omega*, vol. 1, no. 1, pp. 148–159, 2016.
- [70] A. Buin, P. Pietsch, J. Xu, O. Voznyy, A. H. Ip, R. Comin, and E. H. Sargent, "Materials processing routes to trap-free halide perovskites," *Nano Lett.*, vol. 14, no. 11, pp. 6281–6286, 2014.
- [71] G. Xing, B. Wu, S. Chen, J. Chua, N. Yantara, S. Mhaisalkar, N. Mathews, and T. C. Sum, "Interfacial Electron Transfer Barrier at Compact TiO₂/CH₃NH₃PbI₃ Heterojunction," *Small*, vol. 11, no. 29, pp. 3606–3613, 2015.

Chapter 5

Asymmetric Cathodoluminescence Emission in $\text{CH}_3\text{NH}_3\text{PbI}_{3-x}\text{Br}_x$ Perovskite Single Crystals

This chapter presents a temperature-dependent cathodoluminescence (CL) study on $\text{MAPbI}_{3-x}\text{Br}_x$ ($x < 0.02$) single microcubes. CL maps at room temperature revealed a contrasted behavior between the centers and peripheries of the cubes, where peripheries exhibit dominant CL emission compared to much dimmer emission at the centers. At 4 K, the CL emission from the center almost vanishes, suggesting that the dominant surface CL emission is carrier diffusion dependent. Scanning transmission electron microscopy coupled with energy dispersive X-ray spectroscopy reveals that the cubes' centers have a noticeable deficiency in MA cations, which possibly results in a higher density of non-radiative defect traps hindering the CL emission around the center of the cube. Based on this assumption, and on a detailed investigation of other possible origins of the surface enhanced emission, the CL surface emission is explained by a diffusion limited surface recombination, which is dominant, thanks to their less trap densities and reduced electron interaction volumes, at the side walls of the cubes.

The main body of this work resulted in the following publication:

Dar, M. I., Jacopin, G., Hezam, M., Arora, N., Zakeeruddin S. M., Deveaud B., Nazeeruddin, M. K., Gratzel, M. (2016). Asymmetric Cathodoluminescence Emission in $\text{CH}_3\text{NH}_3\text{PbI}_{3-x}\text{Br}_x$ Perovskite Single Crystals. *ACS Photonics*, 3, 947-952.

5.1 Introduction

Perovskite single nano- and microcrystals have recently shown an increasing importance especially in photonic applications [1]–[12]. For example, the pump threshold for amplified spontaneous emission (ASE) in perovskite nanocrystals can be orders of magnitude less than that in perovskite films [3]. The simple chemistry involved in the fabrication of perovskite crystals in addition to their easily accessible size and composition dependent bandgap tuning have recently resulted in the fabrication of perovskite based electrically driven light emitting devices, where perovskite nano- and micro-crystals are efficiently implemented in a variety of configurations [8]–[10].

In order to improve the possible applications of such nano/micro crystals, the optical properties have to be thoroughly evaluated. Besides the average optical quality measurements, carried out by standard PL/absorption techniques, local properties in these crystals are also important. In a single micro/nano crystal, complications associated with grain boundaries in perovskite thin films do not exist; however, the surface properties can, for example, be dominant. Also, the average optical properties measured using traditional PL/absorption techniques can hide a number of details such as inhomogeneities in the optical qualities of single constituent micro/nano crystals [13]. These details can be essential for a better understanding, and therefore better improvement chances, of the crystal growth conditions.

Recently, there have been few studies on the local optical properties of perovskite micro/nanocrystals [1], [3], [5], [6], [14]. Confocal laser scanning microscopy (in short confocal microscopy) has been mainly used for this purpose. In a confocal optical microscope, a focused laser beam excites a single position on the sample, and a subsequent spatial filtering of the emitted light blocks emission from all other points of the sample, at which diffused carriers can possibly recombine. Scanning of the excitation point can then produce a PL map of the microcrystal. The diffusion process of excited carriers at the point of excitation will, expectedly, result in reducing the received emission signal. Compared to polycrystalline thin films, perovskite single microcrystals have higher carrier mobilities [15], [16], thus greatly enhancing this diffusion effect. In confocal microscopy measurements with time-resolved capabilities, this effect manifests itself through an ultrafast PL decay component [14]. Therefore, the PL map produced by confocal microscopy contains information on both recombination and diffusion properties of carriers in the microcrystal, which needs to be carefully accounted for during analysis.

Unlike confocal microscopy, where both excitation and emission are spatially constrained, Cathodoluminescence (CL), on the other hand, has no spatial filtering in the optical collection line. Therefore, photons emitted far from the excitation point can still be collected, limited only by the field size of the SEM and the carrier recombination dynamics (i.e. material's quality). Therefore, CL provides an alternative method to account for this diffusion effect, which can be useful in the analysis of some specific cases as will be seen below.

As discussed in Chapter 1, halide exchange reactions in perovskites, besides resulting in tailored bandgaps, provide a superior approach to control the growth mechanism of perovskite microcrystals [17]–

[19]. Considering $\text{MAPbI}_{3-x}\text{Br}_x$ for example, even a small Br/I ratio ($x \sim 0$), which preserves the bandgap of MAPbI_3 , was shown by Dar et al [19] to be influential for the growth of fascinating $\text{MAPbI}_{3-x}\text{Br}_x$ single crystalline microcubes, as well as for obtaining better performing solar cell devices. Studying the optical quality of single microcrystals is thus necessary to evaluate the growth mechanism and obtain deeper insights for further improvements. This chapter presents a temperature-dependent CL study on those $\text{MAPbI}_{3-x}\text{Br}_x$ microcubes. CL mapping was carefully carried out for different microcubes, and a highly asymmetric CL emission was observed, where the peripheries of the cubes exhibit a predominant CL emission compared to much dimmer centers. The CL emission from microcubes' centers was remarkably low at room temperature, and it almost vanished at 4 K. To unravel the origin of this striking asymmetric CL emission, the effect of temperature and acceleration voltage on the CL emission is investigated. Other possible origins of this behavior are also discussed, such as the edge effect, WGM modes and self-absorption. Additionally, the CL results are correlated to Energy Dispersive X-ray Spectroscopy maps carried out by using Scanning Transmission Electron Microscopy (STEM-EDS maps). Considering these studies, the CL asymmetric behavior could be explained by a diffusion process that takes place from the microcube's center, where a noticeable MA-cation deficiency exists as revealed by STEM-EDS maps, to its outer surface. Thanks to the small interaction volumes in our measurements, estimated by Monte Carlo simulations, the cube surface facets parallel to the incident electron beam will be much less damaged by the e-beam, providing, besides their less MA-deficiency related traps, a longer lived location for carrier recombination.

5.2 Description of Samples and Experimental Conditions

The sample preparation, along with high resolution SEM and STEM-EDS measurements, were carried out by Dr. Ibrahim Dar, within a collaboration with the group of Prof. Nazeeruddin, EPFL. In short, a PbBr_2 film is first prepared by spin-coating a PbBr_2 solution (1.2 M in DMSO) on a 250 nm mesoporous Al_2O_3 film, followed by drying at 80 °C for ~ 15 minutes. The prepared PbBr_2 film is then soaked in MAI solution (8 mg/mL in 2-propanol) for 20 minutes, followed by drying at 80 °C for 15 minutes as well. During the soaking step, both processes of Br-/I- exchange and the perovskite phase formation take place at the same time, ultimately resulting, in ~ 20 minutes, in the growth of $\text{MAPbI}_{3-x}\text{Br}_x$ microcubes of $\sim 1\text{-}2 \mu\text{m}$ sizes. Figure 5.1 shows a top-view high resolution FE-SEM image of the grown $\text{MAPbI}_{3-x}\text{Br}_x$ cubes supported on the $\text{ms-Al}_2\text{O}_3$ substrate. The cubes are then removed from the Al_2O_3 substrate (by simple scratching), and the obtained powder is dispersed in toluene, before being dispersed again on a Si substrate. The cubes on the Si substrate are left to dry long enough before they are inserted in the SEM-CL vacuum chamber for CL measurements. Further details on the sample preparation can be found elsewhere [19], [20].

CL measurements were carried out under acceleration voltages of 3.3 kV and 6 kV, and a probe current of ~ 2 nA. The fast damage induced by the electron beam was carefully considered during the measurements. Perovskites in general have indeed been reported to be easily destroyed by the electron beam [21]–[26]. Specifically, in addition to the fast quenching of the CL signal, the electron beam causes the

CL emission peak to harshly blue-shift with time (in seconds) [22], [24], [26]. This effect can be reduced/eliminated by reducing the acceleration voltage, probe current and stage temperature (cooling) [22]. In our measurements, even with the higher 6 kV acceleration voltage, cooling the substrate to ~ 4 K allowed a strikingly constant CL peak position and a longer CL emission from a single microcube up to more than 2 minutes (Figure 5.2a), which was enough to take 64×64 pixel CL maps with dwell times ranging between ~ 10 -50 ms. As will be discussed below, the asymmetric CL behavior is observed with both the low-temperature orthorhombic and the room-temperature tetragonal perovskite phases. Therefore, substrate cooling, which was essential to stabilize the CL peak position, does not affect the main conclusions of this work.

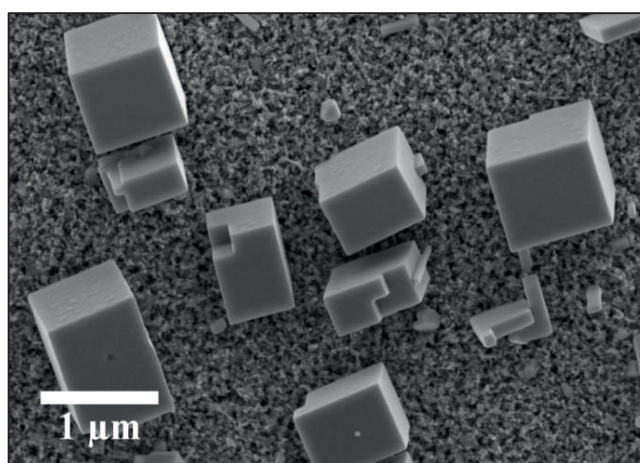


Figure 5.1 Top-view FE-SEM image of MAPbI_{3-x}Br_x microcubes grown on Al₂O₃ scaffold

Figure 5.2a shows the CL emission degradation from a single microcube in the first two minutes at 4 K with an acceleration voltage of 6 kV. The blue-shifting effect was completely absent, manifested by the constant peak position with time. The CL quenching as well as the slight increase in the FWHM of the CL emission peak (Figure 5.2b) can be attributed to the creation of electron-beam induced defects with their subsequent induced damage to the perovskite structure [22].

Another important point revealed by Figure 5.2a is that the e-beam induced damage does not result in transformation of perovskite into PbI₂ phase, whose radiative emission is located at ~ 2.3 eV [27]. Unlike the photo-induced damage discussed in Chapter 4, e-beam damage is fully destructive. Therefore, panchromatic CL maps will exclusively reflect the CL emission of the microcube in its perovskite phase. At room temperature, CL mapping could be achieved only with acceleration voltage of 3.3 kV.

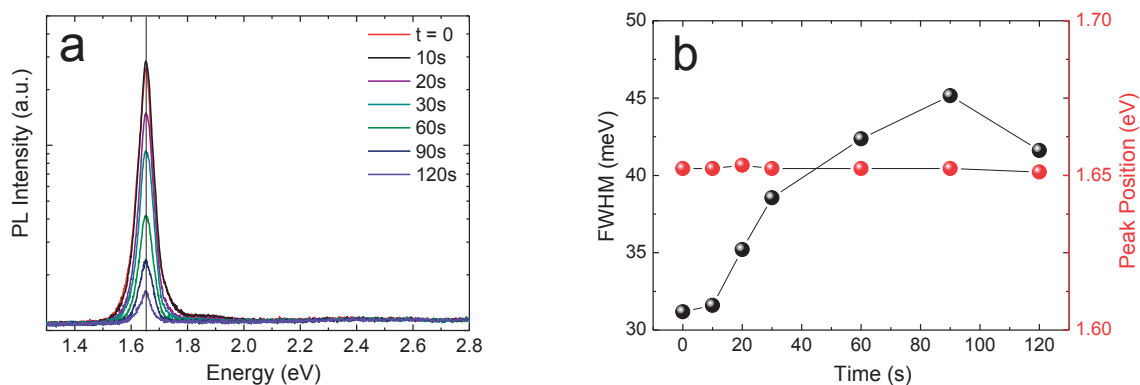


Figure 5.2 (a) Quenching of CL emission with time for a single $\text{MAPbI}_{3-x}\text{Br}_x$ microcrystal for the first two minutes. The measurements are taken under acceleration voltage of 6 kV, probe current of 2 nA and a stage temperature of 4 K (b) Time evolution of calculated FWHM and peak position of the CL emission peak with time for the measurements in (a)

5.3 Results and Discussion

Figure 5.3 shows typical top-view SEM and panchromatic CL maps for two microcubes at 4 K (Figure 5.3a & b) and at 300 K (Figure 5.3d & e), under acceleration voltage of 3.3 kV. A contrasted CL emission can be clearly noticed between the centers and edges of both cubes. The CL emission from the cubes' edges is dominant over that from the center, with a surface emission "width" of ~ 100 nm. The CL emission inhomogeneity can be clearly observed at both temperatures of 4 K and 300 K, indicating that this effect is not correlated with the temperature dependent crystallographic perovskite phase. However, the CL emission of the cube center is noticeably dimmer at 4 K (Figure 5.3b) than it is at 300 K (Figure 5.3e). Figure 5.3c and 5.3f respectively show CL intensity line scans across the cubes at 4 K and 300 K (lines shown on corresponding SEM images). While the cube at 4 K has an almost vanishing CL emission at the center, the relative CL emission from the center of the cube at 300 K was at least one order of magnitude higher. Of course, the higher CL emission in the center at 300 K cannot be attributed to a specific recombination site in the cube. Therefore, the possibility that it originates from the surface recombination of diffused carriers created near the center, their mobility being assisted by the higher temperature, cannot be ruled out. In fact, the vanishing CL emission at 4 K strongly supports this proposition. This diffusion assisted surface recombination will be further elaborated below.

In a perovskite film, de Quilettes et al [28] showed that grain boundaries are optically much dimmer than the bulk of the grains, indicating the creation of non-radiative centers at the grain boundaries. For a single crystal, however, surface effects play differently and both radiative and non-radiative recombination can take place through different mechanisms. For example, strong surface non-radiative recombination is a well-reported issue for many semiconductor nanocrystals, such as Si [29], [30] and GaAs [31], [32]. On the other hand, radiative surface recombination has been reported for other semiconductor nanocrystals, e.g.

ZnO nanocrystals [33], [34]. Also, the geometrical shape of the microcrystal can enhance surface-located recombination, via Whispering Gallery Modes (WGM) for example, as reported for many materials including perovskites [1], [6]. Additionally, interaction of the electron beam with the edge of the microcrystal has to be considered as well, as edge-related inhomogeneities can also take place, as discussed in Chapter 2. All these effects have to be considered when assigning the origin of the observed CL inhomogeneity. In the following, we discuss the different possible origins of the observed CL edge emission.

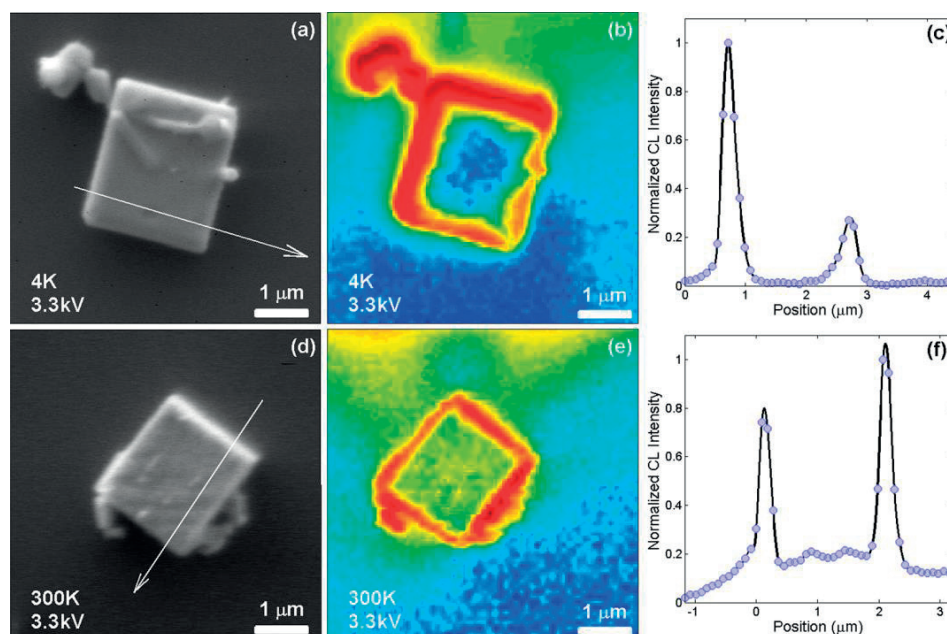


Figure 5.3 (a) FE-SEM image and (b) panchromatic CL image for a typical $\text{MAPbI}_{3-x}\text{Br}_x$ microcube at 4 K and acceleration voltage of 3.3 kV. (c) Line scan of CL intensity along the arrow indicated in (a). (d) FE-SEM image and (e) panchromatic CL image for another $\text{MAPbI}_{3-x}\text{Br}_x$ microcube at 300 K and acceleration voltage of 3.3 kV. (c) Line scan of CL intensity along the arrow indicated in (d). For a better clarity of the effect, the CL maps were integrated between 755 and 765 nm for (b) and between 742 and 793 nm for (d).

As discussed in Chapter 2, the “edge effect” is an enhanced emission of secondary electrons at the edges and morphological peaks in the sample. As more secondary electrons are emitted at the edge, the generated electron-hole pairs at the edge will therefore be reduced, in contradiction to our results. To further investigate this point, a CL map was carried out on a microcube at an acceleration voltage of 6 kV, at which the “edge effect” must be enhanced, presumably resulting in less CL emission from the edge. Figure 5.4b shows the CL map obtained at 4 K. Strikingly, the CL emission from the surface is further enhanced, highly reducing the central dimmer area in the CL map. This directly excludes the edge effect from having an important role in the explanation of our findings. It has to be mentioned here that the e-beam induced damage was extremely high under 6 kV rendering it much more difficult to carry out CL maps. For this

purpose, several CL maps were carried out for several microcubes under 6 kV, and the consistency of the CL behavior was reliably ensured.

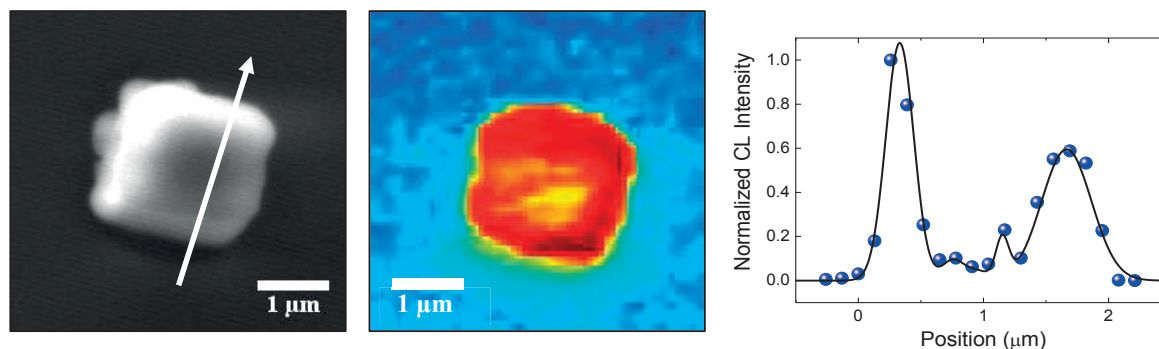


Figure 5.4 (a) FE-SEM image and (b) panchromatic CL map for a typical $\text{MAPbI}_{3-x}\text{Br}_x$ microcube at 4 K under an acceleration voltage of 6 kV. (c) CL intensity line scan as indicated in the line depicted in (a).

In fact, as can be seen in Figure 5.4b & c, the “emitting surface shell” is now wider (~ 300 nm) under 6 kV, and the center is more emitting than under 3.3 kV (Figure 5.3b & c). To explain these issues, Monte Carlo simulation was carried out using CASINO v2.42 software [35]. A number of 2×10^4 electrons were used for simulating the electron trajectories and CL emission from a $2 \mu\text{m}$ thick perovskite sample on a Si substrate. The electron beam diameter was taken to be 10 nm. The Monte Carlo simulation results are shown in Figure 5.5. Clearly, only the top surface is probed in our measurements. Under 3.3 kV, an interaction volume of ~ 100 nm below the surface is obtained. The resulting CL emission originates almost from the same depth of the interaction volume, peaking at ~ 30 nm below the surface.

As expected, a larger interaction volume of ~ 300 nm diameter is obtained at 6 kV, and the CL emission originates from the same depth peaking at ~ 75 nm below the surface. In fact, this can explain the smaller dimmer volume under 6 kV compared to 3.3 kV as follows. Assuming a carrier diffusion assisted recombination at the surface, as anticipated from the results in Figure 5.3 and supported by the high mobility of carriers in perovskites, the larger generation volume at 6 kV will allow more electrons in the center to diffuse towards the surface and recombine. Therefore, the width of the “emitting surface shell” will also reflect the size of the interaction volume, resulting in a wider “emitting surface shell” under higher acceleration voltages. This also resulted in the relatively brighter center at 6 kV, as can be seen in Figure 5.4.

It has to be mentioned here that these Monte Carlo simulations do not take diffusion effects into consideration, and that the high mobility of carriers is expected to significantly reduce the CL emission from the top layer than expected by the Monte Carlo simulations. However, the simulations serve to estimate the theoretically maximum CL emission from the top layer, which will be useful to set an upper bound for self-absorption as will be discussed below.

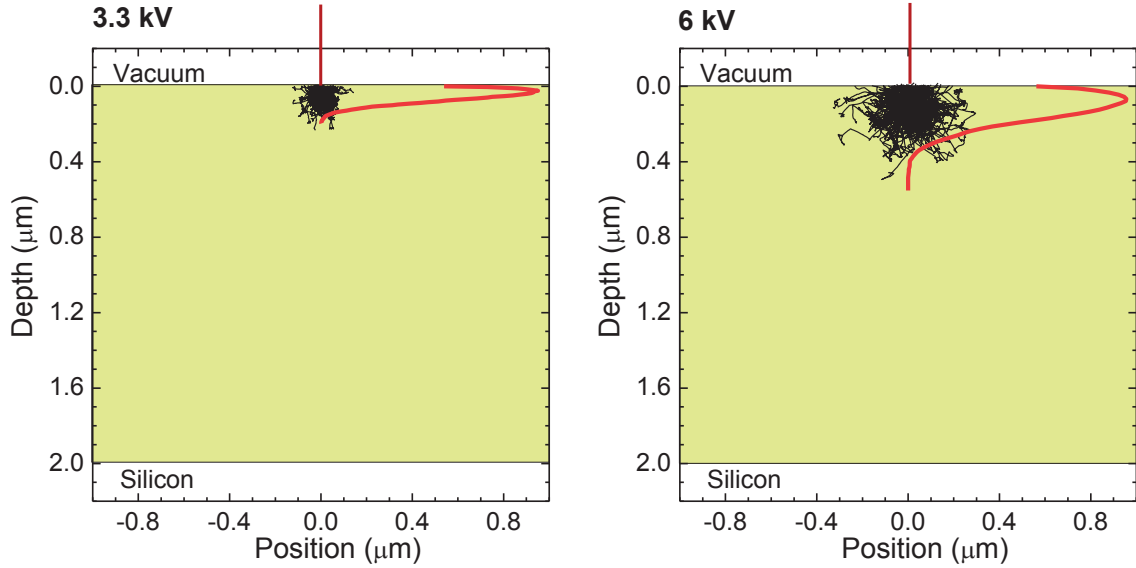


Figure 5.5 Monte Carlo simulations for electron trajectories (black) and resulting CL depths (red) resulting from e-beam excitation (brown vertical line) at the center of a 2 μm perovskite cube under acceleration voltages of 3.3 kV and 6 kV.

Self-absorption is expected to be enhanced for CL emission from the center compared to that from the edge, which can possibly explain the reduced CL emission from the microcubes' centers. However, the small interaction volumes of $\sim 100\text{-}300$ nm in our measurements also exclude the possibility of self-absorption from being responsible for the reduced CL emission from the center, as will be shown in the following. Self-absorption can be estimated using the following formula [34]:

$$f_A = (1 + \alpha d)^{-1} \quad (5.1)$$

where α is the absorption coefficient, d is the depth, and f_A is the attenuation factor for self-absorption. Assuming an absorption coefficient of $\sim 5 \times 10^4 \text{ cm}^{-1}$ above the bandgap [36], and considering that, at the CL emission peak, the absorption coefficient has decreased by at least one order of magnitude, it is reasonable to use a value of $5 \times 10^3 \text{ cm}^{-1}$ for the correction of self-absorption effects.

Figure 5.6 plots the CL emission corrected for self-absorption along the vertical direction for both acceleration voltages of 3.3 kV and 6 kV. We obtain an attenuation factor of ~ 0.95 along the vertical direction, for a depth of 100 nm, indicating that, under 3.3 kV, only a maximum of 5% CL emission is self-absorbed. For a depth of 30 nm, where the CL emission has its peak value at 3.3 kV, the attenuation is less than 2%. Under 6 kV, whose interaction volume extends to ~ 300 nm below the surface, self-absorption can account for 13% attenuation for CL emission originating at 300 nm, and less than 4% for 75 nm depth where the CL emission has its maximum. At directions other than the vertical direction, the CL emission will be less efficiently collected as the self-absorption attenuation will be more pronounced. Therefore, the direction allowing the most efficient contribution to the measured CL signal is the vertical direction, where

at most 5-13% is self-absorbed. This, indeed, cannot explain the “at least one order of magnitude” increase of CL signal at the edges. It has to be stated again here that diffusion effects, i.e. what happens before carrier recombination and CL emission, are completely ignored in this argument, further ruling out the possibility of self-absorption being responsible for the observed CL behavior.

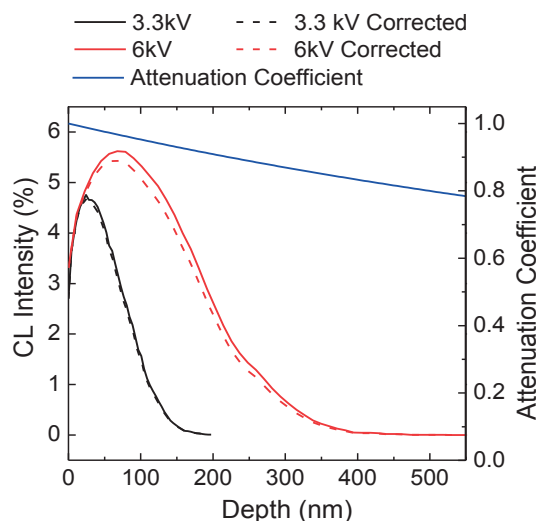


Figure 5.6 Monte Carlo simulated CL emission intensity under 3.3 kV and 6 kV acceleration voltages corrected for self-absorption using Eq. 5.1. The calculated self-absorption coefficient is plotted with blue color, and it ranges between ~ 0.87 -1 for a CL emission depth of 0-300 nm.

Surface emission can also be enhanced through WGM modes. WGM modes is a phenomenon in which a resonator with a regular shape and smooth edges acts as a cavity for the emitted light. Cavity modes, which simply satisfy the standing wave condition in the resonator, can then be amplified. WGM modes were observed for MAPbB_3 perovskite microcubes by Liao et al [6]. To test the possibility of having WGM modes, CL mapping was carried out on another microcube evidencing an irregular shape, as shown in Figure 5.7. Clearly, the same CL behavior is still observed, which directly excludes the possibility of WGM modes being responsible for the observed CL emission. Furthermore, no WGM spatial or wavelength modulation was observed in the obtained CL maps/spectra as noticed above.

Our results are also different from what has been reported by Grancini et al [37], where a contrasted PL emission behavior between the bulk and surface of a perovskite crystal was observed, and attributed to the adsorption of water molecules at the surface of the crystal. The perovskite crystals studied by Grancini et al were intentionally treated under moisture conditions, and the surface emission enhanced by adsorption of water molecules was also recognized by a shift of ~ 50 meV in the surface emission spectrum. In our study, the crystals were studied in vacuum without post-treatment by moisture. Also, there was essentially no significant shift in the CL emission between the center and the edge of the microcrystal; the

shift was always < 5 meV. Figure 5.8 shows typical CL spectra at the center and the edge of a microcube carried out at a temperature of 4 K and acceleration voltage of 6 kV.

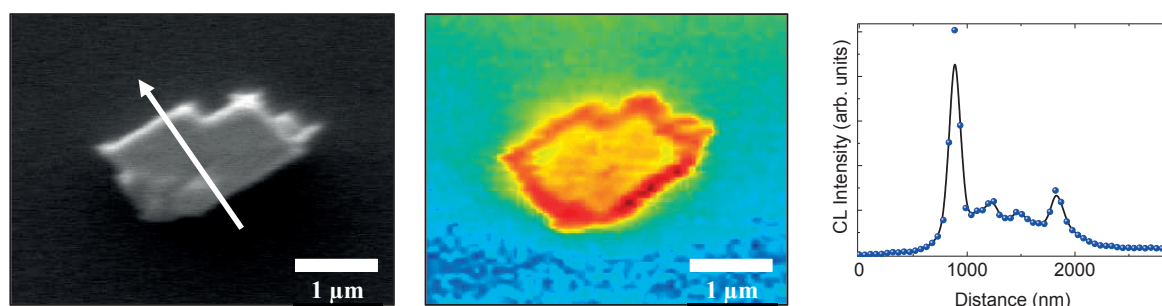


Figure 5.7 (a) FE-SEM image and (b) panchromatic CL map for a $\text{MAPbI}_{3-x}\text{Br}_x$ microcube with an irregularity in its cubical shape at 300 K, 3.3 kV. (c) CL intensity line scan as indicated in the line depicted in (a).

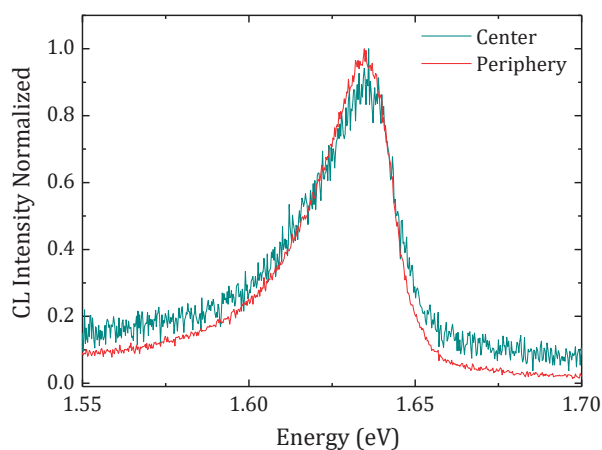


Figure 5.8 CL spectra at the center and at the periphery (edge) of a $\text{MAPbI}_{3-x}\text{Br}_x$ microcube measured at 4 K with an acceleration voltage of 6 kV.

To summarize, the observed contrasted CL emission between the center and surface of the $\text{MAPbI}_{3-x}\text{Br}_x$ microcubes most probably originates from a carrier diffusion limited recombination at the surface, and cannot be attributed to several other possible surface/edge related processes. This in fact raises the important question about the reason behind the strongly reduced, even almost vanishing at 4 K and 3.3 kV, carrier recombination in the center. To unravel this puzzle, energy dispersive X-ray elemental analysis was carried out on the microcubes. Figure 5.9 shows typical STEM-EDS maps for a microcube of $\sim 1 \mu\text{m}$ size. Interestingly, although lead (Pb) and iodine (I) are homogeneously distributed through the microcube, MA (resembled by the N map) has a noticeable deficiency in the center. Br was homogeneously present with < 2 at. % as well. These maps clearly associate the observed CL behavior with inhomogeneous distribution of MA cations in the cube, indicating a defective cube's center, in which carrier recombination is dominated by

non-radiative traps. Therefore, when the center is excited by the e-beam, carriers diffusing to the less defective surface can radiatively recombine. The mobility of carriers will be reduced at 4 K, which results in less number of carriers reaching the surfaces. At higher acceleration voltages, electrons are generated in a larger interaction volume thus increasing the possibility of diffusion and subsequent radiative recombination mainly at the side walls of the cube.

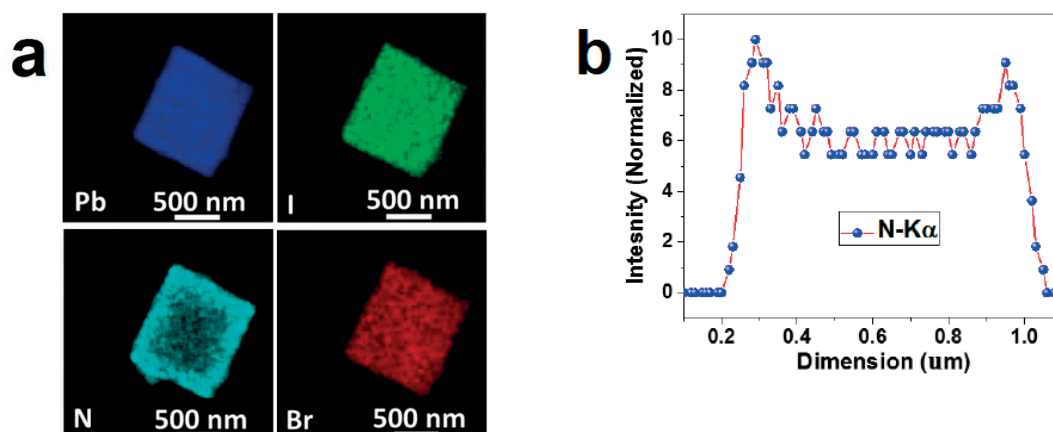


Figure 5.9 (a) STEM-EDS maps for Pb, I, N and Br for a $\text{MAPbI}_{3-x}\text{Br}_x$ microcube (b) EDS Line scan of N $\text{K}\alpha$ X-ray signal across the microcube.

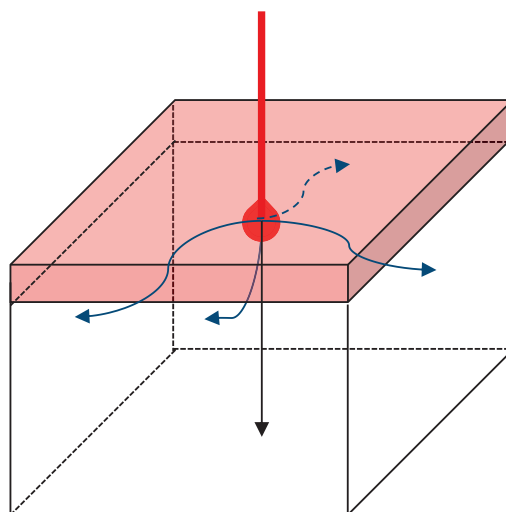


Figure 5.10 Schematic showing the proposed radiative recombination mechanism to explain the observed enhanced CL emission at the surface. In the center, defect traps will result in non-radiative recombination in the vicinity of the excitation point. However, carriers can radiatively recombine at the surfaces, which have fewer traps. The top surface will be damaged by the e-beam. Among the other 5 surfaces, carriers have a better chance to diffuse to the side walls (blue curved arrows) than to the farther bottom surface (black straight arrow). Thanks to the small electron generation volumes, the e-beam damage will affect only the top layer (shown in pink) thus leaving intact the largest portion of the side walls.

Now, according to the above analysis, the top surface of the cube (at which the e-beam first hits) should also contribute to the radiative recombination process, thus increasing the CL emission from the center. However, the e-beam induced damage, which can precede the e-beam induced excitation, apparently does not allow this contribution. On the other hand, the bottom surface, as shown by the Monte Carlo simulation above, is too far away to be reached by the e-beam. Nevertheless, excited carriers, limited by their temperature-dependent mobility, might have a chance, although small, to recombine at the bottom surface. However, in addition to this small chance of recombination at the bottom surface, self-absorption will also reduce any collected CL emission from the bottom surface crossing the large vertical distance of $\sim 1\text{-}2\ \mu\text{m}$. Hence, the four side walls will mainly contribute to the CL signal. In fact, the small generation volumes of $\sim 100\text{-}300\ \text{nm}$ will keep the largest portion of the side walls intact at least for the first CL scanning cycle. At an excitation point on the cube's edge, carriers need to diffuse much less in order to reach the intact area of the nearest side wall and recombine, thus producing a higher CL emission. Figure 5.10 shows a schematic showing the proposed diffusion limited recombination at the side walls.

In summary, enhanced CL emission is observed at the edges of $\text{MAPbI}_{3-x}\text{Br}_x$ microcubes, and is attributed to a high deficiency of MA cations in the cubes' centers, revealed by STEM-EDS elemental maps. The mechanism of surface recombination is investigated, and is shown to be mainly governed by the carrier diffusion to the side walls of the cube. This study explains the strong e-beam induced damage, which has to be carefully taken into consideration when analyzing the situation under study. Taking that into consideration, new insights could be exposed on the carrier dynamics in microcrystals of organo metal halide perovskites.

References

- [1] Q. Zhang, S. T. Ha, X. Liu, T. C. Sum, and Q. Xiong, "Room-temperature near-infrared high-Q perovskite whispering-gallery planar nanolasers," *Nano Lett.*, vol. 14, no. 10, pp. 5995–6001, 2014.
- [2] B. R. Sutherland, S. Hoogland, M. M. Adachi, C. T. O. Wong, and E. H. Sargent, "Conformal organohalide perovskites enable lasing on spherical resonators," *ACS Nano*, vol. 8, no. 10, pp. 10947–10952, 2014.
- [3] H. Zhu, Y. Fu, F. Meng, X. Wu, Z. Gong, Q. Ding, M. V. Gustafsson, M. T. Trinh, S. Jin, and X.-Y. Zhu, "Lead halide perovskite nanowire lasers with low lasing thresholds and high quality factors," *Nat. Mater.*, vol. 14, no. 6, pp. 636–642, 2015.
- [4] J. Xing, X. F. Liu, Q. Zhang, S. T. Ha, Y. W. Yuan, C. Shen, T. C. Sum, and Q. Xiong, "Vapor Phase Synthesis of Organometal Halide Perovskite Nanowires for Tunable Room-Temperature Nanolasers," *Nano Lett.*, vol. 15, no. 7, pp. 4571–4577, 2015.
- [5] Y. Fu, H. Zhu, A. W. Schrader, D. Liang, Q. Ding, P. Joshi, L. Hwang, X.-Y. Zhu, and S. Jin, "Nanowire Lasers of Formamidinium Lead Halide Perovskites and Their Stabilized Alloys with Improved Stability," *Nano Lett.*, vol. 16, no. 2, pp. 1000–1008, 2016.
- [6] Q. Liao, K. Hu, H. Zhang, X. Wang, J. Yao, and H. Fu, "Perovskite microdisk microlasers self-assembled from solution," *Advanced Materials*, vol. 27, no. 22, pp. 3405–3410, 2015.
- [7] L. Protesescu, S. Yakunin, M. I. Bodnarchuk, F. Bertolotti, N. Masciocchi, A. Guagliardi, and M. V. Kovalenko, "Monodisperse Formamidinium Lead Bromide Nanocrystals with Bright and Stable Green Photoluminescence," *J. Am. Chem. Soc.*, vol. 138, no. 43, pp. 14202–14205, 2016.
- [8] M. F. Aygueler, M. D. Weber, B. M. D. Puscher, D. D. Medina, P. Docampo, and R. D. Costa, "Light-Emitting Electrochemical Cells Based on Hybrid Lead Halide Perovskite Nanoparticles," *J. Phys. Chem. C*, vol. 119, no. 21, pp. 12047–12054, 2015.
- [9] A. Perumal, S. Shendre, M. Li, Y. K. E. Tay, V. K. Sharma, S. Chen, Z. Wei, Q. Liu, Y. Gao, P. J. S. Buenconsejo, S. T. Tan, C. L. Gan, Q. Xiong, T. C. Sum, and H. V. Demir, "High brightness formamidinium lead bromide perovskite nanocrystal light emitting devices," *Sci. Rep.*, vol. 6, pp. 36733, 2016.
- [10] L. Meng, E.-P. Yao, Z. Hong, H. Chen, P. Sun, Z. Yang, G. Li, and Y. Yang, "Pure Formamidinium-Based Perovskite Light-Emitting Diodes with High Efficiency and Low Driving Voltage," *Adv. Mater.*, vol. 29, no. 4, pp. 1603826, 2016.
- [11] F. Zhu, L. Men, Y. Guo, Q. Zhu, U. Bhattacharjee, P. M. Goodwin, J. W. Petrich, E. A. Smith, and J. Vela, "Shape evolution and single particle luminescence of organometal halide perovskite nanocrystals," *ACS Nano*, vol. 9, no. 3, pp. 2948–2959, 2015.
- [12] L. Protesescu, S. Yakunin, M. I. Bodnarchuk, F. Krieg, R. Caputo, C. H. Hendon, R. X. Yang, A. Walsh, and M. V. Kovalenko, "Nanocrystals of Cesium Lead Halide Perovskites (CsPbX_3 , X = Cl, Br, and I): Novel Optoelectronic Materials Showing Bright Emission with Wide Color Gamut," *Nano Lett.*, vol. 15, no. 6, pp. 3692–3696, 2015.
- [13] P. Corfdir, M. Abid, A. Mouti, P. A. Stadelmann, E. Papa, J.-P. Ansermet, J.-D. Ganière, and B. Deveaud-Plédran, "Biexciton emission and crystalline quality of ZnO nano-objects," *Nanotechnology*, vol. 22, no. 28, pp. 285710, 2011.
- [14] C. Zhao, W. Tian, J. Leng, R. Cui, W. Liu, and S. Jin, "Diffusion-correlated local photoluminescence kinetics in $\text{CH}_3\text{NH}_3\text{PbI}_3$ perovskite single-crystalline particles," *Science Bulletin*, vol. 61, no. 9, pp. 665–669, 2016.
- [15] D. Shi, V. Adinolfi, R. Comin, M. Yuan, E. Alarousu, A. Buin, Y. Chen, S. Hoogland, A. Rothenberger, K. Katsiev, Y. Losovyj, X. Zhang, P. A. Dowben, O. F. Mohammed, E. H. Sargent, and O. M. Bakr, "Low trap-state density and long carrier diffusion in organolead trihalide perovskite single crystals," *Science*, vol. 347, no. 6221, pp. 519–22, 2015.

- [16] T. M. Brenner, D. A. Egger, A. M. Rappe, L. Kronik, G. Hodes, and D. Cahen, "Are Mobilities in Hybrid Organic-Inorganic Halide Perovskites Actually 'High'?", *Journal of Physical Chemistry Letters*, vol. 6, no. 23, pp. 4754–4757, 2015.
- [17] A. B. Wong, M. Lai, S. W. Eaton, Y. Yu, E. Lin, L. Dou, A. Fu, and P. Yang, "Growth and Anion Exchange Conversion of $\text{CH}_3\text{NH}_3\text{PbX}_3$ Nanorod Arrays for Light-Emitting Diodes.," *Nano Lett.*, vol. 15, pp. 5519–5524, 2015.
- [18] D. Zhang, Y. Yang, Y. Bekenstein, Y. Yu, N. A. Gibson, A. B. Wong, S. W. Eaton, N. Kornienko, Q. Kong, M. Lai, A. P. Alivisatos, S. R. Leone, and P. Yang, "Synthesis of Composition Tunable and Highly Luminescent Cesium Lead Halide Nanowires through Anion-Exchange Reactions," *J. Am. Chem. Soc.*, vol. 138, no. 23, pp. 7236–7239, 2016.
- [19] M. Ibrahim Dar, M. Abdi-Jalebi, N. Arora, T. Moehl, M. Grätzel, and M. K. Nazeeruddin, "Understanding the Impact of Bromide on the Photovoltaic Performance of $\text{CH}_3\text{NH}_3\text{PbI}_3$ Solar Cells," *Adv. Mater.*, vol. 27, no. 44, pp. 7221–7228, 2015.
- [20] M. I. Dar, G. Jacopin, M. Hezam, N. Arora, S. M. Zakeeruddin, B. Deveaud, M. K. Nazeeruddin, and M. Grätzel, "Asymmetric Cathodoluminescence Emission in $\text{CH}_3\text{NH}_3\text{PbI}_{3-x}\text{Br}_x$ Perovskite Single Crystals," *ACS Photonics*, vol. 3, no. 6, pp. 947–952, 2016.
- [21] E. Edri, S. Kirmayer, S. Mukhopadhyay, K. Gartsman, G. Hodes, and D. Cahen, "Elucidating the charge carrier separation and working mechanism of $\text{CH}_3\text{NH}_3\text{PbI}_{3-x}\text{Cl}_x$ perovskite solar cells," *Nat. Commun.*, vol. 5, pp. 3461, 2014.
- [22] C. Xiao, Z. Li, H. Guthrey, J. Moseley, Y. Yang, S. Wozny, H. Moutinho, B. To, J. J. Berry, B. Gorman, Y. Yan, K. Zhu, and M. Al-Jassim, "Mechanisms of Electron-Beam-Induced Damage in Perovskite Thin Films Revealed by Cathodoluminescence Spectroscopy," *J. Phys. Chem. C*, vol. 119, no. 48, pp. 26904–26911, 2015.
- [23] C. G. Bischak, E. M. Sanehira, J. T. Precht, J. M. Luther, and N. S. Ginsberg, "Heterogeneous Charge Carrier Dynamics in Organic-Inorganic Hybrid Materials: Nanoscale Lateral and Depth-Dependent Variation of Recombination Rates in Methylammonium Lead Halide Perovskite Thin Films," *Nano Lett.*, vol. 15, no. 7, pp. 4799–4807, 2015.
- [24] O. Hentz, Z. Zhao, and S. Gradečak, "Impacts of Ion Segregation on Local Optical Properties in Mixed Halide Perovskite Films," *Nano Lett.*, vol. 16, no. 2, pp. 1485–1490, 2016.
- [25] N. Klein-Kedem, D. Cahen, and G. Hodes, "Effects of Light and Electron Beam Irradiation on Halide Perovskites and Their Solar Cells," *Acc. Chem. Res.*, vol. 49, no. 2, pp. 347–354, 2016.
- [26] H. Yuan, E. Debroye, K. Janssen, H. Naiki, C. Steuwe, G. Lu, M. Moris, E. Orgiu, H. Uji-i, F. De Schryver, P. Samori, J. Hofkens, and M. Roeffaers, "Degradation of Methylammonium Lead Iodide Perovskite Structures through Light and Electron Beam Driven Ion Migration," *J. Phys. Chem. Lett.*, vol. 7, no. 3, pp. 561–566, 2016.
- [27] X. Liu, S. T. Ha, Q. Zhang, M. de la Mata, C. Magen, J. Arbiol, T. C. Sum, and Q. Xiong, "Whispering gallery mode lasing from hexagonal shaped layered lead iodide crystals," *ACS Nano*, vol. 9, no. 1, pp. 687–695, 2015.
- [28] D. W. de Quilettes, S. M. Vorpahl, S. D. Stranks, H. Nagaoka, G. E. Eperon, M. E. Ziffer, H. J. Snaith, and D. S. Ginger, "Impact of microstructure on local carrier lifetime in perovskite solar cells," *Science*, vol. 348, no. 6235, pp. 683–686, 2015.
- [29] J. E. Allen, E. R. Hemesath, D. E. Perea, J. L. Lensch-Falk, Z. Y. Li, F. Yin, M. H. Gass, P. Wang, A. L. Bleloch, R. E. Palmer, and L. J. Lauhon, "High-resolution detection of Au catalyst atoms in Si nanowires," *Nat. Nanotechnol.*, vol. 3, pp. 168–173, 2008.
- [30] Y. Dan, K. Seo, K. Takei, J. H. Meza, A. Javey, and K. B. Crozier, "Dramatic Reduction of Surface Recombination by in Situ Surface Passivation of Silicon Nanowires," *Nano Lett.*, vol. 11, no. 6, pp. 2527–2532, 2011.
- [31] C.-C. Chang, C.-Y. Chi, M. Yao, N. Huang, C.-C. Chen, J. Theiss, A. W. Bushmaker, S. LaLumondiere, T.-W. Yeh, M. L. Povinelli, C. Zhou, P. D. Dapkus, and S. B. Cronin, "Electrical and Optical Characterization of Surface Passivation in GaAs Nanowires," *Nano Lett.*, vol. 12, no. 9, pp. 4484–4489, 2012.

- [32] H. J. Joyce, C. J. Docherty, Q. Gao, H. H. Tan, C. Jagadish, J. Lloyd-Hughes, L. M. Herz, and M. B. Johnston, "Electronic properties of GaAs, InAs and InP nanowires studied by terahertz spectroscopy," *Nanotechnology*, vol. 24, no. 21, pp. 214006, 2013.
- [33] I. Shalish, H. Temkin, and V. Narayanamurti, "Size-dependent surface luminescence in ZnO nanowires," *Phys. Rev. B*, vol. 69, no. 24, pp. 245401, 2004.
- [34] N. Pan, X. Wang, M. Li, F. Li, and J. G. Hou, "Strong Surface Effect on Cathodoluminescence of an Individual Tapered ZnO Nanorod," *J. Phys. Chem. C*, vol. 111, no. 46, pp. 17265–17267, 2007.
- [35] D. Drouin, A. R. Couture, D. Joly, X. Tastet, V. Aimez, and R. Gauvin, "CASINO V2.42 — A Fast and Easy-to-use Modeling Tool for Scanning Electron Microscopy and Microanalysis Users", *Scanning*, vol. 29, no. 3, pp. 92-101, 2007.
- [36] J.-H. Im, C.-R. Lee, J.-W. Lee, S.-W. Park, and N.-G. Park, "6.5% efficient perovskite quantum-dot-sensitized solar cell," *Nanoscale*, vol. 3, no. 10, pp. 4088-4093, 2011
- [37] G. Grancini, V. D'Innocenzo, E. R. Dohner, N. Martino, A. R. Srimath Kandada, E. Mosconi, F. De Angelis, H. I. Karunadasa, E. T. Hoke, and A. Petrozza, " $\text{CH}_3\text{NH}_3\text{PbI}_3$ perovskite single crystals: surface photophysics and their interaction with the environment," *Chem. Sci.*, vol. 6, no. 12, pp. 7305–7310, 2015.

Chapter 6

Conclusions

This thesis is mainly concerned about the optical characterization and carrier dynamics in organo lead halide perovskites. Different luminescence-based characterization techniques were used to study perovskite materials for different purposes. Specifically, the serious stability issues in these materials and the high sensitivity of their optical, and therefore photovoltaic, properties to preparation conditions have been tackled in three different chapters of this thesis. These chapters are preceded by an introductory chapter about the basic structural and optical properties of organo lead halide perovskites that includes a recent literature review about the possible origins of stability and disorder problems in these materials. The main outcomes of this work and some future perspectives are discussed in the following two sections.

6.1 Summary of Results

In the first study, a correlation between time-resolved photoluminescence (TRPL) of high quality FAPbBr₃ films and the open-circuit voltage (V_{oc}) of the corresponding perovskite solar cell devices was established. We showed that the solvent used during the perovskite film deposition has a critical role in the resulting quality of the film and device performance. Specifically, FAPbBr₃ based devices fabricated using a 1:1 molar ratio of DMF:DMSO solvents in the perovskite film synthesis showed a record V_{oc} of 1.42 V. This value is close to the calculated theoretical value (~ 1.70 V), estimated using the PL decay constant, and was higher than the reported built-in potential set by the device contacts, which uncovers new insights into the charge separation mechanism in perovskite solar cells.

Amplified spontaneous emission (ASE) measurements were carried out on the same films, and the results of ASE dependence on the solvent were highly congruent with the device results. The effect of excitation wavelength on the ASE performance was investigated, and the thermal effects associated with higher energy as well as highly absorbed pulses had almost no effect on the quantum efficiency. The gain behavior was also investigated for the films, and the relatively strong exciton binding energy in the FAPbBr₃ films resulted in a strong Sommerfeld enhancement effect at the band edge. This property allowed us to propose a convenient method to estimate the bandgap renormalization (BGR) directly from the ASE

peak position. BGR was observed in our samples as a red-shift in the ASE emission peak with increasing pump power, and a BGR constant of $\sim 5\text{-}7 \times 10^{-9}$ eV.cm was obtained.

The second study is devoted to UV-induced damage in MAPbI₃ mesoporous and solid films. Temperature dependent studies were carried out for different metal oxide interface material (namely, TiO₂ and Al₂O₃) and for a bulk MAPbI₃ film. The UV-damage showed a strong temperature dependence completely switching off below 200 K. We conclude that many UV-induced degradation processes are possible, some of which are reported in the literature; however, the direct dissociation of molecular bonds in the MA cation is proposed to be the primary degradation step. The study concludes with a short section on the charge separation efficiency of electrons at the MAPbI₃/TiO₂ interface, which is measured in our work to be negligible.

The third study presents a cathodoluminescence study on MAPbI_{3-x}Br_x ($x < 0.02$) microcubes. The CL emission from the cube was dominant at the edges, while the CL emission from the center was largely reduced at room temperature, and almost vanishing at 4 K. STEM-EDX analysis revealed a noticeable deficiency of MA cations in the cube's centers, which calls for revising the optical quality resulting from perovskite micro/nanostructures prepared by using halide exchange synthesis procedures. The analysis was further continued with Monte Carlo simulations, showing that, for a microcube with high concentration of trap sites in the center and significant carrier mobility, the observed enhanced CL emission from the surface can be explained by the recombination of diffused carriers at the side walls of the microcube.

6.2 Future Perspectives

In a short time span of less than 5 years, which is the time duration of this thesis as well, it has been really thrilling to witness the commencement of the field of perovskite solar cells, along with the dramatic improvement in their efficiency from $\sim 9\%$ to 22.1%. The other thrilling fact is that this enormous improvement has been achieved for solution-processed materials that can be easily synthesized in the lab.

Of course, this triggered a lot of research to explain these extraordinarily successful materials, and, on the other unfortunate hand, to explain the main obstacle in this kind of solar cells: instability. An organic cation is an ingredient in the crystalline structure, and it can naturally come to mind that it is behind the stability problems. In fact, this was clearly demonstrated in our study on the UV-damage, where low temperature freezing of the MA cation could save the perovskite structure from UV-damage. At higher temperatures, in addition to the disorder gained by the organic cation movements in the octahedral cage of the perovskite structure, the organic nature of the MA cation appears, solely, by the possibility of direct bond dissociation under UV radiation. However, this is not the end of the story. The disorder created by the organic cation is also shown to be important for slow carrier recombination, a vital success factor for perovskite solar cell devices. Research efforts on the replacement of the MA cation by the heavier more stable one, Formamidinium FA, resulted, on one side, in a dramatic increase in the time stability of the material, as shown in our work as well. However, for iodide-based perovskites, with their bandgaps of ~ 1.6

eV optimal for photovoltaics, power conversion efficiencies of FA-based perovskites are still facing some problems, and finally only a mixed FA-MA cation could demonstrate reputable efficiencies. Although some of these problems are related to the stability of the crystalline phase of FA-based perovskite, the slower charge dynamics allowed by the MA cation cannot be overlooked.

These stability issues, besides affecting the device performance, necessitate a high carefulness when characterization measurements are carried out on the perovskite samples. For example, the PL decay under UV excitation of 280 nm pulses at the $\text{TiO}_2/\text{MAPbI}_3$ interface, which exist even at low temperatures as discussed in Chapter 4, was at the beginning thought to be a sign of electron injection at the $\text{TiO}_2/\text{MAPbI}_3$ interface. Only after few months, when we decided to change the excitation wavelength to 425 nm, simply to exclude the effect of TiO_2 absorption and have cleaner results, the strong PL decay as well as the PL quenching were both observed to switch off. Careful analysis of the measurements could ultimately result in uncovering important conclusions about the UV-induced degradation mechanisms. As another example, despite the high e-beam induced damage in the CL mapping study, substrate cooling and Monte Carlo simulations could help to decouple the effect of the e-beam induced damage in the analysis and explain the carrier recombination mechanism in the microcubes.

The current achieved efficiencies of perovskite solar cells are already well within the accepted values in the market, and in fact exceeding some traditionally available solar cell technologies of far higher cost and less scalability. Therefore, stability is the main issue to be tackled in the future. In fact, the current stream is moving toward mixing strategies for improved stability, and several successful approaches have provided nice improvements. From the point of view of material characterization, this will, from one side, stabilize the samples under study and simplify the necessary analysis and precautions. From another side, however, complicated mixed interface materials are involved in these new strategies, which will require additional analytical efforts.

Although the record power conversion efficiencies are almost stabilized since last year, the field of organo lead halide perovskite solar cells, and currently organo lead halide based photonics, will expectedly continue at a very fast pace for the next couple of years. The continuous stability improvement over the last two years has given the necessary fuel for this field to keep lightening. Additionally, the various combinations of material design and device structures investigated in the literature is another factor, forecasting a longer dispersed research future. Although some successful designs look on track to be commercially feasible, the winning material/device design(s) is yet early to be expected; from this point of view, the field of perovskite solar cells is still in its infancy!

Curriculum Vita

Personal Information

Name	Mahmoud Saeed Hezam
Nationality	Yemeni
Date of birth	1981
Place of birth	Taéz, Yemen
Marital Status	Married, with two kids
Email address	mhezam@gmail.com mahmoud.hezam@epfl.ch

Education

2012-2017	PhD in Physics from Ecole Polytechnique Fédérale de Lausanne (EPFL), Switzerland
2004-2007	MSc in Physics from King Fahd University of Petroleum and Minerals (KFUPM), Dhahran, Saudi Arabia
1999-2004	BSc in Physics from King Fahd University of Petroleum and Minerals (KFUPM), Dhahran, Saudi Arabia

Work Experience

2008-present	Researcher, King Abdullah Institute for Nanotechnology, King Saud University, Riyadh, Saudi Arabia
2004-2008	Research Assistant, Department of Physics, King Fahd University of Petroleum and Minerals (KFUPM), Dhahran, Saudi Arabia

List of Publications

1. A. Mekki, N. Tabet, M. Hezam, "Synthesis and characterization of nitrogen-doped ZnO thin films" *International Journal of Nano and Biomaterials* (2009) - Vol. 2, pp. 216 - 225.
2. M. Hezam, N. Tabet, A. Mekki, "Synthesis and Characterization of DC Magnetron Sputtered ZnO Thin Films Under High Working Pressures", *Thin Solid Films* 518 (2010), pp. e161-e164.
3. N. Hamdan, N. Tabet, M. Hezam, Z. Hussain, "The use of X ray absorption near-edge structure and X ray magnetic circular dichroism in diluted magnetic semiconductors", *Integration of Nuclear Spectrometry Methods as a New Approach to Material Research* (2011), pp. 111.
4. A. Ansari, J. Labis, A. Aldwayyan, M. Hezam, "Facile synthesis of water-soluble luminescent mesoporous Tb(OH)₃@SiO₂ core-shell nanospheres", *Nanoscale Research Letters* 2013, 8:163
5. H. M. Ghaithan, H. M., S. M. Qaid, M. Hezam, M. B. Siddique, I. M. Bedja, A. S. Aldwayyan, "Invoking the frequency dependence in square modulated light intensity techniques for the measurement of electron time constants in dye-sensitized solar cells", *SPIE Proceedings, Nanoengineering: Fabrication, Properties, Optics, and Devices XII*, 9556 (2015), pp. 955604-955604.
6. J. P. Labis, M. Hezam, A. Al-Anazi, H. Al-Brithen, A. A. Ansari, A. M. El-Toni, R. Enriquez, G. Jacopin, M. Al-Hoshan, "Pulsed laser deposition growth of 3D ZnO nanowall network in nest-like structures by two-step approach", *Solar Energy Materials and Solar Cells* 143 (2015), pp. 539-545
7. N. Arora, M. I. Dar, M. Hezam, W. Tress, G. Jacopin, T. Moehl, P. Gao, A. S. Aldwayyan, B. Deveaud, M. Gratzel & M. K. Nazeeruddin, "Photovoltaic and Amplified Spontaneous Emission Studies of High-Quality Formamidinium Lead Bromide Perovskite Films", *Advanced Functional Materials* (2016), 26(17), 2846-2854.
8. M.I. Dar, G. Jacopin, M. Hezam, N. Arora, S. M. Zakeeruddin, B. Deveaud, M. K. Nazeeruddin, M. Gratzel, "Asymmetric cathodoluminescence emission in CH₃NH₃PbI_{3-x}Br_x Perovskite Single Crystals", *ACS Photonics* (2016), 3, 947-952.
9. H. M. Ghaithan, S. M. Qaid, M. Hezam, J. P. Labis, M. Alduraibi, I. M. Bedja, A. S. Aldwayyan, "Laser induced photocurrent and photovoltage transient measurements of dye-sensitized solar cells based on TiO₂ nanosheets and TiO₂ nanoparticles", *Electrochimica Acta* (2016), 212, 992-997.
10. M. Hezam, A. Alqasem, S. Qaid, G. Jacopin, M. N. Khan, N. Arora, M. I. Dar, B. Deveaud, M. K. Nazeeruddin, A. Aldwayyan, "Investigation of Threshold Carrier Density of Amplified Spontaneous Emission from Optically Pumped Formamidinium Lead Bromide Perovskite Film", (submitted to *Advanced Optical Materials*).
11. S. Qaid, M. A. Majeed Khan, M. Hussain, M. Hezam, H. M. Ghaithan, H. Albrithen, A. Aldwayyan, "Structural and Optical Investigation of Brookite TiO₂ Thin Films Grown by Atomic Layer Deposition on Si(111) Substrates", (submitted to *Thin Solid Films*).
12. M. Hezam, G. Jacopin, P. Qin, A. Aldwayyan, M. K. Nazeeruddin, B. Deveaud, "Elucidating UV-degradation Mechanisms in Methylammonium Lead Halide Perovskite", (to be submitted).

Selected Conference Communications

1. M. Hezam, N. Tabet and A. Mekki, "Synthesis and Characterization of DC Magnetron Sputtered ZnO Thin Films Under High Working Pressures", Presented at the International Conference on Materials for Advanced Technologies (ICMAT 2009), 28 June -3 July 2009, Singapore
2. M. Hezam, M. Alhoshan, M. Alsalhi, S. Alrokayyan, M. Kawwam, "Lithography-independent Fabrication of Long Nanogap Electrodes", Presented at the International Conference on Materials for Advanced Technologies (ICMAT 2011), 26 June -1 July 2011, Singapore.
3. M. Hezam, A. Eltoni, J. Labis, B. Alruhaimi, M. Alduraibi, A. Aldwayyan, "Growth of Raspberry-like and Sphere-like TiO₂ Nanostructures by Controlled Agglomeration of TiO₂ Nanocrystals", presented at the ImagineNano 2013 Conference (Trends in NanoApplications: Energy), April 23-26th, 2013, Bilbao, Spain.
4. M. Hezam, G. Jacopin, M. Shahmohammadi, Q. Peng, S. Qaid, I. Bedja, J-D Ganiere, A. Aldwayyan, M. K. Nazeerudin, M. Gratzel, B. Deveaud, "Investigation of Charge Separation and Charge Injection Dynamics in Perovskite Solar Cells", presented as (oral) at the Hybrid and Organic Photovoltaics 2014 Conference (HOPV14), May 11-14th, 2014, Lausanne, Switzerland.

